University of California
Los Angeles

Measurement of non-photonic electron azimuthal anisotropy v_2 from Au+Au collisions at $\sqrt{s_{NN}} = 200\ GeV$

A dissertation submitted in partial satisfaction
of the requirements for the degree
Doctor of Philosophy in Physics

by

Weijiang Dong

2006

The dissertation of Weijiang Dong is approved.

Ren Sun

Ernest Abers

Charles A. Whitten Jr.

Huan Z. Huang, Committee Chair

University of California, Los Angeles

2006

To my parents and Zhendi

Table of Contents

1 Introduction 1

1.1 Quarks, Gluons and Quark-Gluon Plasma 2

1.2 Momentum Space Azimuthal Anisotropy v_2 7

1.3 Observations 13

1.3.1 Jet Quenching 13

1.3.2 Partonic Collectivity 15

1.4 Heavy Quark v_2 18

2 Experiment 21

2.1 The Accelerator: Relativistic Heavy Ion Collider 21

2.2 The Detector: Solenoid Tracker At RHIC 25

2.2.1 Time Projection Chamber: TPC 26

2.2.2 Barrel Electro-Magnetic Calorimeter: BEMC 30

2.2.3 Barrel Shower Maximum Detector: BSMD 38

3 Data Analysis 43

3.1 Event Specific Analysis 43

3.2 Track Specific Analysis 58

3.2.1 Charged Tracks Reconstruction by TPC 58

3.2.2 Electro-Magnetic Particles Reconstruction by BEMC and BSMD 60

3.2.3 Hadron Rejection and Electron Selection 77

3.2.4 Photonic Electron Background Removal 86
3.2.5 Photonic Electron Background Removal Efficiency 100

4 Results and Discussion 112

4.1 Results 112
4.2 Discussion 113
4.3 Non-photonic electron spectra measurement 117

A Kinematics 121

A.1 Transverse momentum 121
A.2 Rapidity and Pseudo-rapidity 121

B The STAR Collaboration 123

References 128

List of Figures

1.1 The prediction of a phase transition for quark system at critical temperature by lattice QCD 4

1.2 Quark system phase diagram 6

1.3 A typical non-central collision of two heavy nuclei 8

1.4 The overlap of a non-central collision of two heavy nuclei 8

1.5 The evolution of the coordinate space azimuthal anisotropy into a momentum space azimuthal anisotropy 9

1.6 The measured identified particle's v_2 and hydrodynamic calculations 11

1.7 Hadron R_{cp} measured by STAR 14

1.8 Strange hadron v_2 in Au+Au 200 GeV minimum biased events measured by STAR 16

1.9 Strange hadron v_2 measured by STAR scaled by number of constituent quarks 17

1.10 Non-photonic electron v_2 and D meson v_2 correlation 20

2.1 The RHIC Complex 24

2.2 The STAR detector system 25

2.3 The STAR TPC schematic view 27

2.4 First relativistic Au+Au collision recorded by the STAR TPC . . 28

2.5 The longitudinal and lateral energy loss profiles in Electro-Magnetic Calorimeters 33

2.6 The BEMC side view from $-Z$ direction 34

2.7 The BEMC module side view 35

2.8 The BEMC module cross sectional view 36

2.9 The BEMC wavelength-shifting fiber 37

2.10 Schematic illustration of the double layer STAR BSMD 39

2.11 Cross sectional view of the STAR BSMD 40

3.1 Detailed event statistics for Au+Au 200 *GeV* electron v_2 analysis 44

3.2 The STAR reference multiplicity distribution for Au+Au 200 *GeV* minimum biased events 46

3.3 Centrality bin distribution for Au+Au 200 *GeV* minimum biased events 47

3.4 Track's ϕ distributions in Au+Au 200 *GeV* minimum biased events 50

3.5 Track's weighted ϕ distributions in Au+Au 200 *GeV* minimum biased events 52

3.6 Event plane azimuthal angle distribution for Au+Au 200 *GeV* minimum biased events 53

3.7 Sub-event plane azimuthal angle correlation for Au+Au 200 *GeV* minimum biased events 55

3.8 Raw event plane resolution correction factor for Au+Au 200 *GeV* minimum biased events 56

3.9 Weighted event plane resolution correction factor for Au+Au 200 *GeV* integrated centrality intervals 57

3.10 dE/dx v.s. P measured by the STAR TPC 59

3.11 The behavior of a module in a typical d+Au 200 *GeV* event . . . 62

3.12 The STAR library BEMC point reconstruction chain 63

3.13 A situation when ϕ cluster crosses two sub-divisions 65

3.14 The flow chart of the UCLA BEMC reconstruction software: *StEmcPointMaker* 67

3.15 BSMD η and ϕ module clustering threshold distribution 68

3.16 The mean and sigma of the 150 detecting channels in each BSMD ϕ module 68

3.17 The BSMD ϕ clustering threshold of each module 69

3.18 The comparison of using two different energy sharing choices . . . 73

3.19 Number of working η/ϕ strips below a tower cluster 74

3.20 $\eta - \phi$ distribution of the reconstructed BEMC points 75

3.21 The invariant mass spectra of two BEMC reconstructed particles using different merging parameters 76

3.22 P/E for electron candidates and P/E for all tracks with BEMC association 79

3.23 Number of BSMD hits for electrons and hadrons 80

3.24 Two dimensional projection distance distribution for all tracks with BEMC point association 81

3.25 One dimensional projection distance distributions in z/η and ϕ directions for all tracks with BEMC point association 82

3.26 dE/dx distributions of all the tracks after BEMC cuts 83

3.27 The purity of the inclusive electron sample after the BEMC cuts as a function of p_T 85

3.28 The primary vertex DCA cut's effect on photon conversion electron background removal 87

3.29 The same sign pair and opposite sign pair invariant mass distributions 89

3.30 Tracking resolution effect on the invariant mass calculation 90

3.31 2-D invariant mass distributions of photon conversions and π^0 Dalitz decays 93

3.32 2-D invariant mass distributions of same sign and opposite sign pairs 94

3.33 The photonic background subtraction process in non-photonic electron v_2 analysis 96

3.34 The photonic background subtraction process in non-photonic electron v_2 analysis for $2 < p_T(GeV) < 2.5$ and $2.5 < p_T(GeV) < 3$ . . 98

3.35 Photon conversion electron background removal efficiency calculation 102

3.36 π^0 Dalitz decay electron background removal efficiency calculation 103

3.37 The relative fraction of two types of photonic electron background 106

3.38 The weighted average of the π^0 Dalitz decay electron background removal efficiency and the photon conversion electron background removal efficiency 107

3.39 The comparison of an identified photonic electron's partner electron's p_T distributions from real data analysis and simulation data analysis 109

3.40 The comparison of photon conversion asymmetries from real data analysis and simulation data analysis 110

3.41 The calculation of photonic pair asymmetry distributions in the real data analysis 111

4.1 Non-photonic electron v_2 preliminary result 112

4.2 Photonic, non-photonic and inclusive electron ratios 114

4.3 The expected non-photonic electron v_2 error bars for 9 million minimum biased events if the STAR SVT is removed 116

4.4 The non-photonic electron spectra for d+Au, p+p, and Au+Au 200 *GeV* experiments 118

4.5 The non-photonic electron nuclear modification factor R_{AA} for d+Au and Au+Au 200 *GeV* experiments 120

LIST OF TABLES

1.1 Properties of quarks 2

2.1 The RHIC design parameters and specifications. 23

2.2 The STAR subsystems 26

2.3 The STAR BSMD design parameters and specifications 41

3.1 Event selection and cuts 44

3.2 The STAR centrality definition for year 2004 Au+Au 200 *GeV* experiment 48

3.3 Basic track quality cuts 49

3.4 Electron identification cuts 84

3.5 Cuts for invariant mass method for photonic background removal. 93

4.1 The radiation length of material in STAR detector 115

ACKNOWLEDGMENTS

I thank my advisor, Huan Z. Huang, for being the best advisor that I ever know. As a Ph.D student, I greatly benefited from Huan's deep and broad understanding of physics, rich experience in data analysis, and patience in instructing students. I thank Charles A. Whitten Jr. for his suggestions on many aspects of my research, especially on the project of developing the UCLA BEMC reconstruction software. I thank Oleg Tsai for teaching me about detector hardware. I thank George Igo for helping me to improve this dissertation. Thanks also go to other members of the IEP group at UCLA: Vahe Ghazikhanian, Steve Trentalange, Dylan Thein, Steve Guertin, Jingguo Ma, Johan Gonzalez, Priscilla Kurnadi, David Staszak, and former graduate students Hui Long, Hai Jiang, Paul Sorensen, Jeff Wood, Eugene Yamamoto, and former post-doc An Tai, and visiting scholars Xiangzhou Cai, Xiaoyan Lin, Jinhui Chen, Guoliang Ma, Shenqing Feng. I am grateful for having been a member of this great group for five years. I also thank Josephine M. Morrell for her help on the administrative work. I also thank James Dunlop, Zhangbu Xu, Alexander Suaide, Thomas Ullrich, Nu Xu, Yifei Zhang, Frank Laue, and other members of the STAR heavy flavor physics working group for their helps with my research. I thank the RHIC Operations Group and RCF at BNL, and the NERSC Center at LBNL for their support. This work was supported in part by the HENP Divisions of the Office of Science of the U.S. DOE; the U.S. NSF; the BMBF of Germany; IN2P3, RA, RPL, and EMN of France; EPSRC of the United Kingdom; FAPESP of Brazil; the Russian Ministry of Science and Technology; the Ministry of Education and the NNSFC of China; IRP and GA of the Czech Republic, FOM of the Netherlands, DAE, DST, and CSIR of the Government of India; Swiss NSF; the Polish State Committee for Scientific Research; STAA of Slovakia, and the Korea Sci. & Eng. Foundation.

VITA

May 3rd, 1979	Born, Qianjiang, Hubei, China.
July, 2000	B.S. in Physics, University of Science and Technology of China, Hefei, Anhui, China
July, 2001	M.S. in Physics, University of California, Los Angeles, USA
2001–2003	Teaching Assistant, Physics and Astronomy Department, University of California, Los Angeles, USA
2003–present	Graduate Research Assistant, Physics and Astronomy Department, University of California, Los Angeles, USA

PUBLICATIONS

J. Adams *et al.*

Incident Energy Dependence of p_t Correlations at RHIC *Phys. Rev. C* **72**:044902, 2005.

J. Adams *et al.*

Multi-strange baryon elliptic flow in Au+Au collisions at $\sqrt{s_{NN}} = 200$ GeV *Phys. Rev. Lett.* **95**:122301, 2005.

J. Adams *et al.*

Multiplicity and Pseudorapadity Distributions of Photons in Au+Au Collisions at $\sqrt{s_{NN}} = 62.4$ GeV *Phys. Rev. Lett.* **95**:062301, 2005.

J. Adams *et al.*

Pion Interferometry in Au+Au Collisions at $\sqrt{s_{NN}} = 200$ GeV. *Phys. Rev.* **C71**:044906, 2005.

J. Adams *et al.*

Pseudorapidity Asymmetry and Centrality Dependence of Charged Hadron Spectra in d+Au Collisions at $\sqrt{s_{NN}} = 200$ GeV. *Phys. Rev.* **C70**:064907, 2004.

J. Adams *et al.*

Open Charm Yields in d+Au Collisions at $\sqrt{s_{NN}} = 200$ GeV. *Phys. Rev. Lett.* **94**:062301, 2005.

J. Adams *et al.*

Measurements of Transverse Energy Distributions in Au+Au Collisions at $\sqrt{s_{NN}} = 200$ GeV. *Phys. Rev.* **C70**:054907, 2004.

J. Adams *et al.*

Transverse Momentum Dependent Modification of Dynamic Texture in Central Au+Au Collisions at $\sqrt{s_{NN}} = 200$ GeV. *Phys. Rev.* **C71**:031901, 2005.

J. Adams *et al.*

Phi Meson Production in Au+Au and p+p Collisions at $\sqrt{s_{NN}} = 200$ GeV. *Phys. Lett.* **B612**:181-189, 2005.

J. Adams *et al.*

Centrality and Psuedorapidity Dependence of Charged Hardron Production at Intermediate pT in Au+Au Collisions at $\sqrt{s_{_{NN}}}$ = 200 GeV. *Phys. Rev.* **C70**:044901, 2004.

J. Adams *et al.*

Three Pion HBT Correlations in RHIC Collisions from the STAR Experiment *Phys. Rev. Lett.* **91**:262301, 2003.

J. Adams *et al.*

Experimental and Theoretical Challenges in the Search for the Quark Gluon Plasma: The STAR Collaboration's Critical Assessment of the Evidence from RHIC Collisions. *Nucl. Phys.* **A757**:102-183, 2005.

J. Adams *et al.*

K(892) Resonance Production in Au+Au and p+p Collisions at $\sqrt{s_{_{NN}}}$ = 200 GeV at STAR. *Phys. Rev.* **C71**:064902, 2005.

J. Adams *et al.*

Production of e+e- Pairs Accompanied by Nuclear Dissociation in Ultra-Peripheral Heavy Ion Collisions. *Phys. Rev.* **C70**:031902, 2004.

J. Adams *et al.*

Photon and Neutral Pion Production in Au+Au Collisions at $\sqrt{s_{_{NN}}}$ = 130 GeV. *Phys. Rev.* **C70**:044902, 2004.

J. Adams *et al.*

Azimuthally Sensitive HBT in Au+Au Collisions at $\sqrt{s_{NN}} = 200$ GeV. *Phys. Rev. Lett.* **93**:012301, 2004.

J. Adams *et al.*

Cross sections and Transverse Single Spin Asymmetries in Forward Neutral Pion Production from Proton Collisions at $\sqrt{s_{NN}} = 200$ GeV. *Phys. Rev. Lett.* **92**:171801, 2004.

J. Adams *et al.*

Azimuthal Anisotropy at RHIC:The First and Fourth Harmonics. *Phys. Rev. Lett.* **92**:062301, 2004.

J. Adams *et al.*

Identified Particle Distrubutions in p+p and Au+Au Collisions at $\sqrt{s_{NN}} = 200$ GeV. *Phys. Rev. Lett.* **92**:112301, 2004.

J. Adams *et al.*

Pion, Kaon, Proton and Anti-Proton Transvserse Momentum Distributions from p+p and d+Au Collisions at $\sqrt{s_{NN}} = 200$ GeV. *Phys. Lett.* **B6**:8-16, 2005.

J. Adams *et al.*

Event by Event Mean pT Fluctations in Au-Au Collisions at $\sqrt{s_{NN}} = 130$ GeV. *Phys. Rev.* **C71**:064906, 2005.

J. Adams *et al.*

Pion Kaon Correlations in Au-Au Collisions at $\sqrt{s_{NN}} = 130$ GeV. *Phys. Rev. Lett.* **91**:262302, 2003.

J. Adams *et al.*

Multistrange Baryon Production in Au+Au Collisions at $\sqrt{s_{NN}} = 130$ GeV. *Phys. Rev. Lett.* **92**:182301, 2004.

J. Adams *et al.*

Rho0 Production and Possible Modification in Au+Au and p+p Collisions at $\sqrt{s_{NN}} = 200$ GeV. *Phys. Rev. Lett.* **92**:092301, 2004.

J. Adams *et al.*

Multiplicity Fluctations in Au+Au Collisions at $\sqrt{s_{NN}} = 130$ GeV. *Phys. Rev.* **C68**:044905, 2003.

J. Adams *et al.*

Rapidity and Centrality Dependence of Proton and Anit-Proton Production from Au+Au Collisions at $\sqrt{s_{NN}} = 200$ GeV. *Phys. Rev.* **C70**:041901, 2004.

ABSTRACT OF THE DISSERTATION

Measurement of non-photonic electron azimuthal anisotropy v_2 from Au+Au collisions at $\sqrt{s_{NN}} = 200\ GeV$

by

Weijiang Dong
Doctor of Philosophy in Physics
University of California, Los Angeles, 2006
Professor Huan Z. Huang, Chair

The elliptic flow parameter v_2 of heavy quarks addresses several important physics issues. It can allow us to gain more insight to the hadronization mechanism of bulk partonic matter. It can test the thermalization of the medium created by relativistic heavy ion collisions. It can enhance our understanding of the energy loss mechanisms in the medium created by relativistic heavy ion collisions.

Direct v_2 measurement of the heavy quark hadrons through hadronic decay channels requires large statistics and/or precise decay vertex determination which are currently not available at STAR. The measurement of electrons from heavy quark semi-leptonic decays allows us to gain insight into the v_2 of the heavy quarks. However, in heavy ion collisions, the produced particles are overwhelmingly hadrons. Also, even in a pure inclusive electron sample, the background photonic electrons prevail over signal non-photonic electrons in the STAR detector configuration where we have a sizable amount of detector materials. These facts pose big challenges for measuring the non-photonic electron v_2. This dissertation will present a method to deal with these challenges. Firstly, a high purity inclusive electron sample is achieved by particle identification using a combination of different detectors. Then the photonic electrons are statistically measured and removed from the inclusive electron sample. Finally, the non-photonic electron v_2 can be calculated from its event-plane-angle-adjusted ϕ distribution. This dissertation will present the preliminary result of a measurement for the non-photonic electron v_2 covering a p_T range from 1.5 to 3 GeV/c by the STAR collaboration. Future directions for non-photonic electron v_2 measurements will also be discussed.

CHAPTER 1

Introduction

Quantum Chromo-Dynamics (QCD), the fundamental theory of the strong interaction, predicts an exotic state of matter being produced in high energy density and high temperature environment. This exotic state of matter is called the Quark Gluon Plasma (QGP), which could have been existed one microsecond after the Big Bang.

QGP is another phase of nuclear matter. Unlike the cold nuclear matter, in which quarks are confined within nucleons, in the QGP boundaries between nucleons disappear and quarks are deconfined. In relativistic heavy ion collisions, a huge amount of energy is deposited into a small volume to create an energy density that is high enough to reach the critical value where the QGP can be possibly created in a laboratory environment.

From the experimental program covering a time span of about five years at the Relativistic Heavy Ion Collider (RHIC), physicists have observed partonic collectivity and jet quenching through the measurements of light hadrons. These findings indicate the creation of strong interacting deconfined quark matter in the laboratory. The measurement of elliptic flow parameter v_2 of heavy quarks will complement these measurements and enhance our understanding of the matter that is created by relativistic heavy ion collisions.

Relevant topics to this dissertation will be briefly introduced in this chapter.

1.1 Quarks, Gluons and Quark-Gluon Plasma

Quarks are the fundamental building blocks of hadrons like protons and neutrons. Table 1.1 lists the properties of the quarks [Won94]. Quarks have a flavor degree of freedom. There are 6 flavors of quarks, namely up (u), down (d), charm (c), strange (s), bottom (b) and top (t). Each quark has a corresponding anti-quark, e.g. $\bar{u}$ is the anti-quark of u quark. Quantum Chromo-Dynamics (QCD) is the fundamental theory that describes the strong interaction between quarks. In QCD, every quark carries a "color". There are three different colors that a quark can carry: red, green and blue. The strong interaction between two quarks depends on the colors that they carry. Two quarks interact with one another by exchange of a gluon. Gluons are bosons and they also carry colors. Just like quarks, gluons interact with other color charged quarks or gluons with the exchange of other gluons. Unlike quarks, gluons do not carry flavors.

Table 1.1: Properties of quarks

Flavor	Charge	I_z	C	S	T	B
u	$\frac{2}{3}$	$\frac{1}{2}$	0	0	0	0
d	$-\frac{1}{3}$	$-\frac{1}{2}$	0	0	0	0
c	$\frac{2}{3}$	0	1	0	0	0
s	$-\frac{1}{3}$	0	0	-1	0	0
t	$\frac{2}{3}$	0	0	0	1	0
b	$-\frac{1}{3}$	0	0	0	0	-1

Gluons "glue" quarks together to form hadrons. There are two kinds of hadrons: mesons and baryons. Gluons "glue" two quarks (quark-antiquark) together to form mesons. Pions are examples of mesons where a π^+ is composed of one u quark and one $\bar{d}$ quark. Gluons "glue" three quarks together to form baryons. Protons and neutrons are examples of baryons where a proton is composed of two u quarks and one d quark and a neutron is composed of two d quarks and one u quark. Hadrons are all color neutral particles. "$q\bar{q}$" is color neutral because it is a color-anticolor pair. "qqq" can be color neutral because it can be the combination of red, green and blue.

Experimentally, no isolated single quark has ever been observed. This suggests that the interaction between quarks and gluons must be very strong when their distance is large. However, Deep Inelastic Scattering (DIS) experiments found that with large momentum transfer, the quarks inside of a hadron behave as if they are free particles. We believe that QCD correctly describes the strong interaction among quarks and gluons because QCD has the property that the interaction is weak at a short distance and strong at a large distance. QCD predicts asymptotic freedom of quarks [GW73, Pol73]. When the distance of interaction is small and the momentum transfer is large, a perturbative treatment can be used. QCD with perturbative treatment is called pQCD. When the distance of interaction is big and the momentum transfer is small, QCD can be calculated on a lattice of space and time, thus lattice QCD. Lattice QCD calculation shows that when the distance of interaction is on the same order of the size dimension of a hadron, the interaction strength is linear with the interaction distance. This characteristic of the interaction confines quarks in the hadrons [Wil74].

Lattice QCD calculations also predict that at sufficiently high temperature, quarks can be deconfined. Figure 1.1 shows that the energy density divided by T^4 as a function of temperature for quark system [Kar02]. When the temperature is approaching critical temperature T_c, the energy density divided by T^4 quickly rises and saturates, which indicates a phase transition. The value of T_c depends on the chemical potential being used in the calculations. For zero chemical potential,

T_c is about 160 MeV. The level of saturation reflects the number of degrees of freedom. The new phase of matter is the Quark Gluon Plasma (QGP). The QGP is a locally thermally equilibrated state of matter in which quarks and gluons are deconfined [Ada05a].

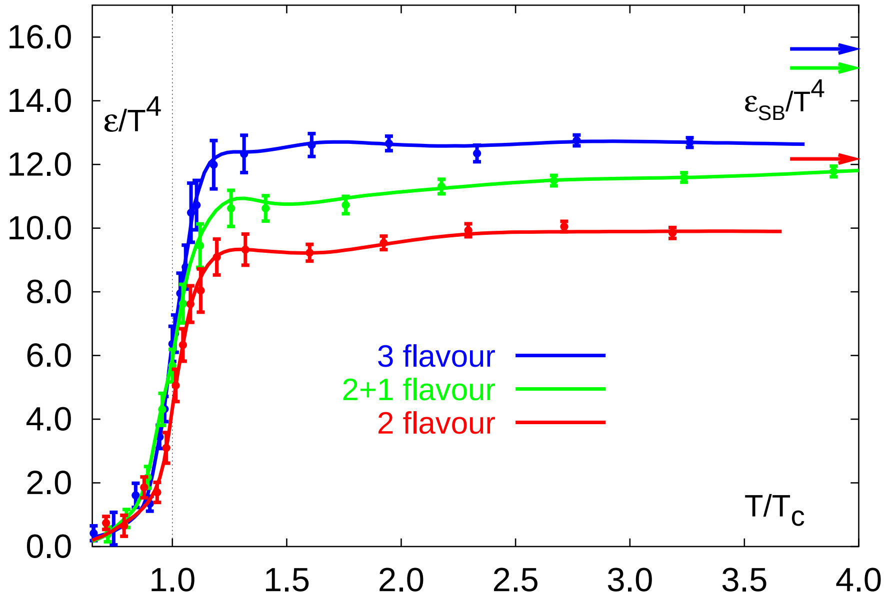

Figure 1.1: The T^4 scaled energy density as a function of temperature for quark system from lattice QCD calculations. When the temperature T reaches the critical temperature T_c, the scaled energy density rapidly rises, which indicates a quick change of the number of degrees of freedom. The change in the number of degrees of freedom means that a phase transition happens. The arrows represent the Stefan-Boltzmann values for asymptotically high temperature. The Stefan-Boltzmann limits are for system of free quarks. The lattice QCD values do not quickly reach at these limits presumably due to the strong interaction of quarks at the temperature range.

Soon after the lattice QCD theory predicted the QGP, physicists realized that QGP can be created in the laboratory by colliding heavy nuclei at relativistic velocities ($v \rightarrow c, \gamma \gg 1$). The large energies deposited into a small volume will be sufficient to reach the energy density needed to create the QGP [Bau75]. In 1974, T.D. Lee brought up a discussion about the need for a physics program to study the QGP [Lee75]. Since then, physicists began to build facilities with higher and higher energies to search for the QGP. These facilities include the Bevalac at Lawrence Berkeley National Laboratory in the early 1980s [NG84], the Alternating Gradient Synchrotron (AGS) at Brookhaven National Laboratory in the late 1980s and the Super Proton Synchrotron (SPS) at CERN also in the late 1980s [HM96]. The Relativistic Heavy Ion Collider (RHIC) was commissioned at Brookhaven National Laboratory in 2000. At the time (February 23, 2006) when this dissertation was written, the Large Hadron Collider (LHC) was being built at CERN and it was due to be switched on in 2007 [Giu03]. Figure 1.2 shows the phase diagram of quark system together with indications of temperature and energy density region reached at these facilities.

QGP is believed to exist approximately one microsecond after the Big Bang and may exist in the cores of many neutron stars, where the pressure makes the baryon density exceed the critical density of the phase transition [Gle01].

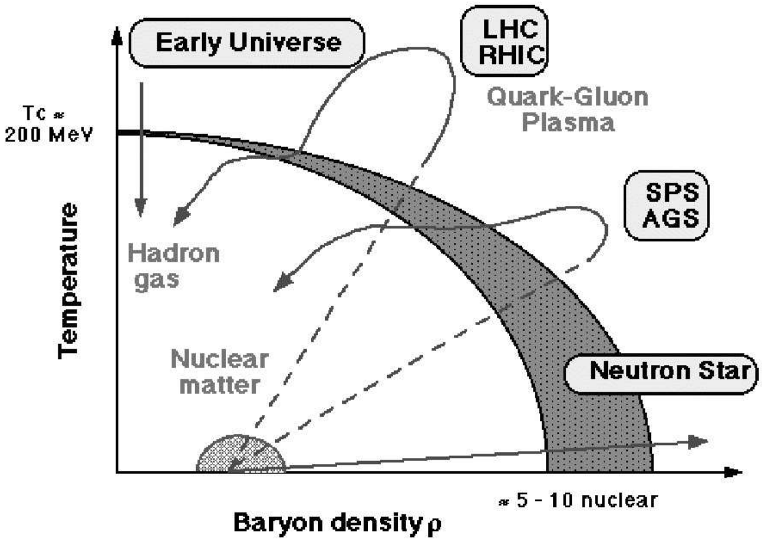

Figure 1.2: Quark system phase diagram with the $T - \rho$ location of each QGP searching experiment, neutron star, cold nuclear matter and the early universe.

1.2 Momentum Space Azimuthal Anisotropy v_2

In a typical non-central relativistic heavy ion collision, because the two heavy nuclei are Lorentz-contracted along the beam axis, they look like two circular discs. Their overlapping zone has the shape of an almond. Thus, initially, there is an azimuthal anisotropic source in coordinate space. A reference plane called reaction plane is defined by the beam axis and the vector connecting the centers of the two colliding nuclei. The length of the vector is called the impact parameter. Since the vector connecting the two colliding nuclei is perpendicular to the beam axis, so the reaction plane can be characterized by the vector's azimuthal angle, which is called reaction plane azimuthal angle. Figure 1.3 shows a typical non-central collision of two heavy nuclei, where Z axis is the beam direction and the X-Z plane is the reaction plane. Figure 1.4 shows the overlap of two non-central colliding nuclei in reaction plane [Sor03]. As the system develops, the particles coming parallel to the reaction plane experience less interactions than the particles coming perpendicular to the reaction plane so their momentum distributions are different. Thus, at the final state, there is an azimuthal anisotropy in momentum space. Figure 1.5 illustrates the evolution of coordinate space azimuthal anisotropy to momentum space azimuthal anisotropy soon after a non-central collision of two heavy nuclei [KSH00].

Mathematically, the particle distribution in momentum space can be expanded into a Fourier series [PV98]:

$$E\frac{d^3N}{dp^3} = \frac{1}{2\pi}\frac{d^2N}{p_T dp_T dy}\left[1 + 2\sum_{n=1}^{\infty} v_n \cos\left[n(\phi - \Psi_{RP})\right]\right] \tag{1.1}$$

where

$$v_n =< \cos[n(\phi - \Psi_{RP})] > \tag{1.2}$$

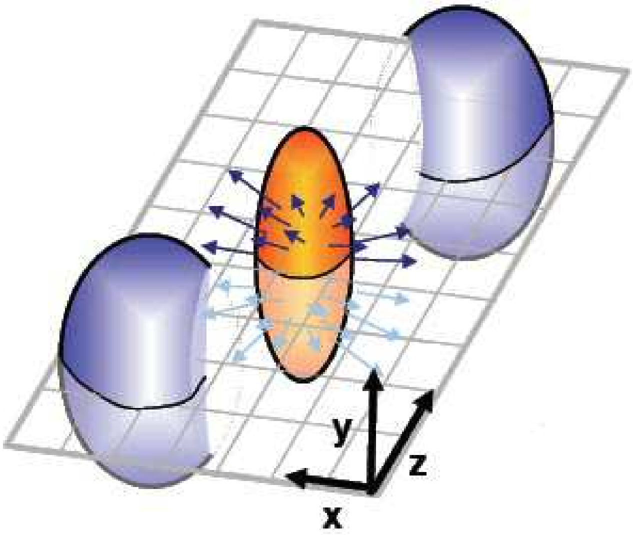

Figure 1.3: A typical non-central collision of two heavy nuclei. Z axis is the beam direction and the X-Z plane is the reaction plane.

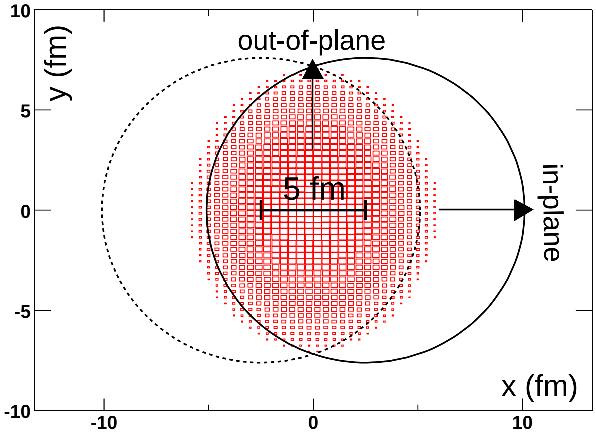

Figure 1.4: The overlap of a non-central collision of two heavy nuclei for $5fm$ impact parameter. Impact parameter is defined as the distance between the centers of the two colliding nuclei. The beam directions are in and out of the page. The two circles represent the two colliding nuclei. The reaction plane is the X-Y plane.

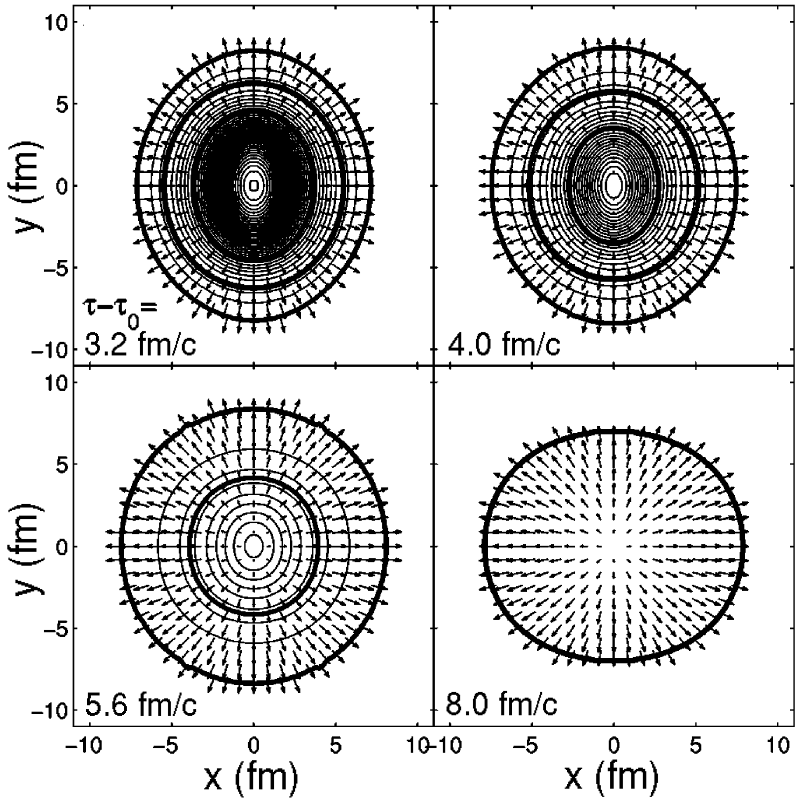

Figure 1.5: The evolution of the coordinate space azimuthal anisotropy into a momentum space azimuthal anisotropy. The calculation is based on the hydrodynamic model.

v_n is the anisotropy parameter of the nth harmonic. p_T, y, and ϕ are respectively transverse momentum, rapidity, and azimuthal angle of the particle. Ψ_{RP} is the reaction plane azimuthal angle. The second harmonic coefficient v_2 is also called *elliptic flow*. It measures the elliptic component of the anisotropy. If v_2 is positive, one will expect more particles coming out parallel to the reaction plane because small angle difference between ϕ and Ψ_{RP} will make $cos[2(\phi-\Psi_{RP})]$ close to 1, and one will expect less particles coming out perpendicular to the reaction plane because when $\phi - \Psi_{RP}$ is close to $\pi/2$, $cos[2(\phi - \Psi_{RP})]$ will be close to -1.

Due to the almond shape of the source, v_2 is the largest and most studied of the anisotropy parameters in relativistic heavy ion physics. Besides v_2, v_1 and v_4 have been measured by STAR as well [Ada04a]. The higher terms of the expansion are found to be small and more difficult to measure experimentally.

To develop a momentum space azimuthal anisotropy from a coordinate space azimuthal anisotropy, multiple interactions are necessary. If each nucleon-nucleon collision is totally independent, the final particle's momentum distribution resulted from the heavy ion collisions will be a simple superposition of many isotopic momentum distributions resulted from many non-correlated nucleon-nucleon collisions. The result of the superposition is an isotropic momentum distribution.

Because multiple interactions, which help to achieve the thermalization of the system, mainly happen during the early stage of the system, and also the azimuthal anisotropy in coordinate space is largest thus the pressure gradient is largest at the beginning of the evolution, the v_2 can reveal the information about the thermalization of the system at the early stage [Sor97].

The recent measurement of the v_2 of identified particles shows a mass ordering phenomenon at low p_T range [Ada04b]. At a given p_T in this range, the v_2 decreases with increasing particle mass. The hydrodynamic model, which assumes ideal fluid flow, describes the mass ordering of v_2 at low p_T very well [HKH01]. The left plot of Figure 1.6 shows the measured v_2 of $\pi^{\pm}$, K_s^0, $\bar{P}$ and $\Lambda + \bar{\Lambda}$ together with hydrodynamic calculations. The success of hydrodynamic model in this p_T range indicates that a strong interacting thermalized quark matter has been created.

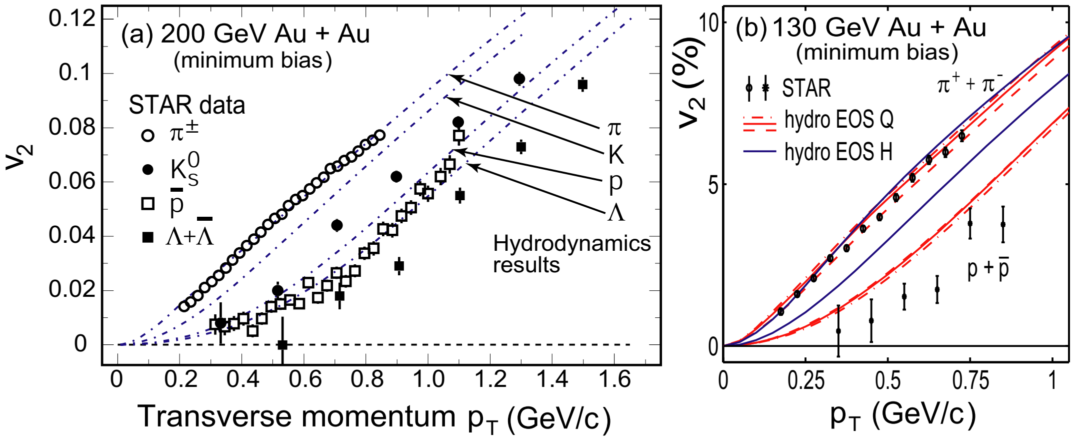

Figure 1.6: The left plot shows the measured v_2 of $\pi^{\pm}$, K_s^0, $\bar{P}$ and $\Lambda + \bar{\Lambda}$ together with hydrodynamic calculations [Ada05a]. At a given p_T in this range, the v_2 decreases with increasing particle mass. This mass ordering is well described by hydrodynamic model. The right plot shows the hydrodynamic calculations by assuming different EoS. The hydrodynamic Eos Q describes the data much better than the hydrodynamic Eos H.

The result from v_2 measurement can constrain the effective Equation of State (EoS) of the nuclear matter created by RHIC [TLS01]. Recent hydrodynamic model study indicates that the nuclear matter created at RHIC has an EoS with a strong first order phase transition between hadron gas and an ideal parton gas [Huo05]. The right plot of Figure 1.6 shows that the EoS Q (QGP EoS) describes the experimental data much better than the EoS H (hadron gas EoS).

This seems to indicate that the phase transition has happened at RHIC collisions.

At mediate p_T, the hydrodynamic model, whose assumption is no longer valid, gives v_2 much larger than experiment results. In this p_T range, the quark recombination model successfully describes the experimental data. At high p_T, the v_2 of identified particles begins to saturate, which implies jet quenching. Section 1.3 will discuss about quark recombination model and jet quenching.

1.3 Observations

The commissioning of RHIC in year 2000 had created an opportunity to study the nuclear matter under high temperature and high energy density conditions [JW05]. The observations of jet quenching and partonic collectivity from the first few years of RHIC operation indicate that a dense and equilibrated system may have been created in the most violent head-on collisions of two heavy nuclei. The initial energy density of these collisions is estimated to be about two orders of magnitude larger than that of cold nuclear matter. That density is well above the critical density for the phase transition that is predicted by the lattice QCD.

1.3.1 Jet Quenching

High transverse momentum particles are believed to originate from initial hard scattering process in the early stage of heavy ion collisions [Adl02], thus these particles are good probes to study the matter created by heavy ion collisions. High transverse momentum partons travel through the matter and lose energy by gluon radiation. Experimentally, two ratios are interesting to look at. One is called nuclear modification factor R_{CP}, which is defined by the ratio of the particle yield scaled by N_{binary} [Won94] from central and peripheral collisions:

$$R_{CP}(p_T) = \frac{[(dN/dp_T)/N_{binary}]^{Central}}{[(dN/dp_T)/N_{binary}]^{Peripheral}} \tag{1.3}$$

The other is called nuclear modification factor R_{AA}, which is defined as the ratio of the particle yield scaled by N_{binary} from two heavy nuclei collision to proton-proton collision:

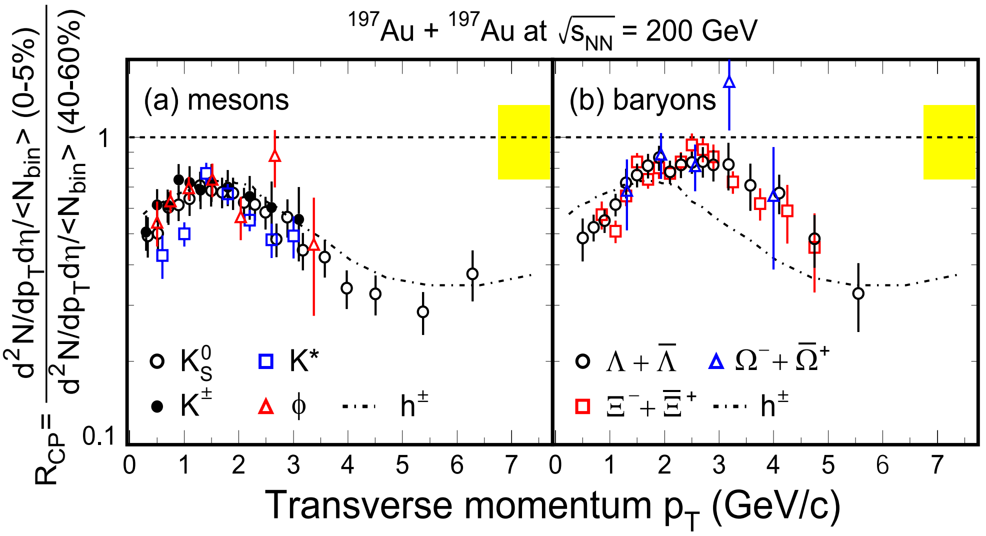

Figure 1.7: Hadron R_{cp} measured by STAR. The left plot is for mesons and right plot is for baryons. The N_{binary} scaled mesons and baryons yields in central collisions are largely suppressed at high p_T. The shaded band around 1 is the systematic error in the N_{binary} calculation, which is based on the Monte Carlo Glauber model.

$$R_{AA}(p_T) = \frac{d^2N/dp_T d\eta}{T_{AA} d^2\sigma^{pp}/dp_T d\eta} \tag{1.4}$$

Where $T_{AA} =< N_{binary} > /\sigma^{NN}_{inel}$ and σ^{NN}_{inel} is the inelastic cross section of nucleon+nucleon collisions.

Both ratios take a reference system which is small and not supposed to reach QGP critical values: one is created by peripheral collisions and the other is created by proton-proton collisions. Figure 1.7 shows the R_{cp} for strangeness hadrons measured by STAR [Sch04]. Both mesons and baryons have large suppression at high p_T. This suppression indicates that a strong interacting dense matter has been created by RHIC.

1.3.2 Partonic Collectivity

Another interesting observation is partonic collectivity. Figure 1.8 shows the v_2 of strange hadrons together with hydro-dynamic model predictions [Ada05b]. For p_T less than 2 GeV, hydro-dynamic model calculations describe the experiment results quite well. However, at high p_T, the model prediction begins to deviate from the data. The meson v_2 and the baryon v_2 both begin to saturate at different levels. Interestingly, if scaled by the number of constituent quarks, as shown in Figure 1.9, the meson v_2 and the baryon v_2 follow the same trend [Ada05b]! This meson and baryon grouping is also observed in the R_{CP} measurement which is shown in Figure 1.7. The quark coalescence model, which assumes the coalescence of constituent quarks as the major hadronization mechanism, naturally explains this grouping observation. A solid conclusion of this is that a deconfined quark system has been created by RHIC.

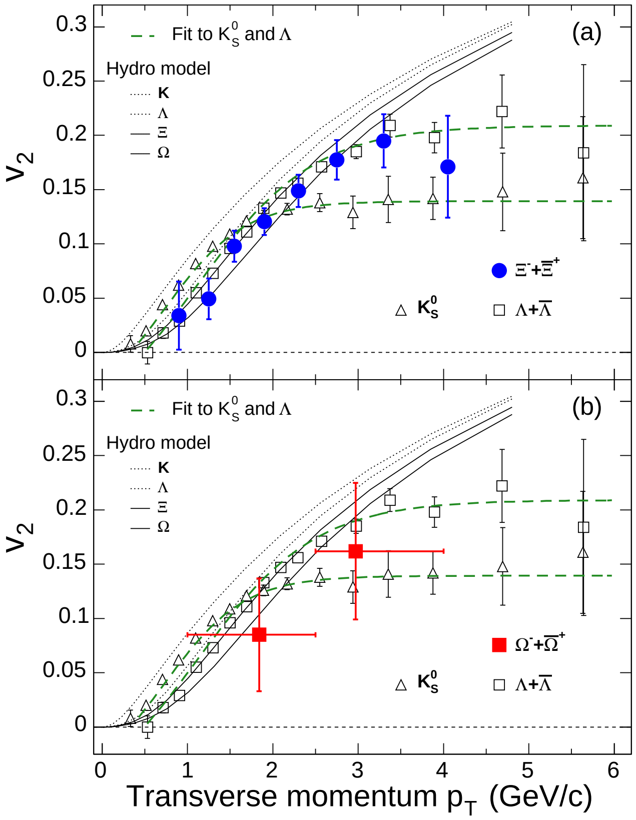

Figure 1.8: Strange hadron v_2 in Au+Au 200 GeV minimum biased events measured by STAR. The predictions from hydrodynamical model calculations are indicated by lines.

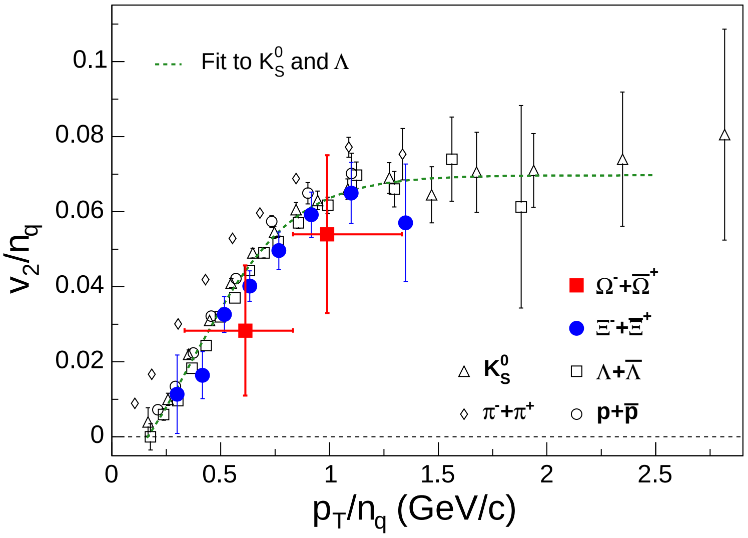

Figure 1.9: Strange hadron v_2 measured by STAR scaled by number of constituent quarks. All particles follow the same trend except for pions.

1.4 Heavy Quark v_2

As discussed in section 1.3, jet quenching and partonic collectivity through the measurement of light hadrons are the most important findings from the first several years of RHIC operation. The measurement of the elliptic flow parameter v_2 of the heavy quarks will complement these measurements and enhance our understanding of the relativistic heavy ion collisions.

The heavy quark v_2 addresses several important physics issues. One issue is the hadronization of bulk partonic matter. A Constituent Quark Number (CQN) scaling in v_2 has been observed in hadrons of light quarks, which has been interpreted as features of hadronization of bulk partonic matter through quark coalescence or recombination. If the heavy quark v_2 follows the same CQN scaling as light quarks, it implies that these heavy quarks may have become a part of the bulk partonic matter through dynamic evolution in the medium and its hadronization mechanism is similar to that of light quarks. A second issue is the thermalization of the hot matter created by the relativistic heavy ion collisions [DES04]. If even the heavy quark flows, then the system should have sufficient interactions among constituents to reach the thermalization. A third issue is the energy loss of heavy quarks in the hot and dense medium created by RHIC [DK01]. At transverse momentum above the recombination region, the energy loss mechanism of light quarks is considered to be responsible for the observed azimuthal angular anisotropy. The measurement of v_2 for heavy quark hadrons will complement this measurement and give new insight into the mechanism by which partons lose energy in the medium.

Direct v_2 measurement of the heavy quark hadrons through hadronic decay channels requires large statistics and/or precise decay vertex determination which are currently not available at STAR. However, the study of the decay products of the heavy quark hadrons may reveal information about these heavy quark hadrons. The heavy quark hadrons have non-negligible semi-leptonic decay branch ratios. For example, D^+, which is composed of c quark and $\bar{d}$ quark, decays into a positive electron (positron) and something else with a branch ratio around 17.2% [Eid04]. Simulation shows that, at high p_T, the v_2 of the daughter electrons from D meson decays are strongly correlated with the v_2 of the D mesons [DES04]. The top plot in Figure 1.10 shows such correlation. Thus, the measurement of electrons from heavy quark semi-leptonic decays allows us to gain insight into the v_2 of the heavy quarks.

Electrons coming from heavy quark decays are called non-photonic electrons. Contrary to non-photonic electrons are the photonic electrons that come from photon conversions and scaler meson Dalitz decays. Section 3.2.4 will discuss how to deal with photonic electrons.

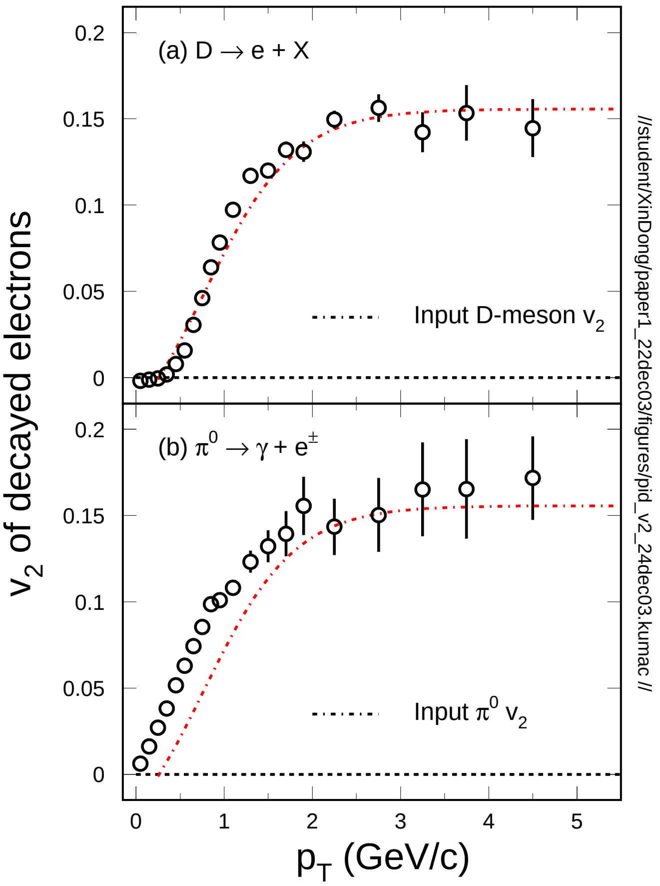

Figure 1.10: The top plot shows the non-photonic electron v_2 and D meson v_2 correlation. The bottom plot shows the correlation between the π^0 Dalitz decay electron v_2 and π^0 v_2.

CHAPTER 2

Experiment

This chapter will discuss the experiment setup. The first section will briefly discuss about the RHIC accelerator. The second section will discuss about the STAR detector system. It will discuss about the major detectors been used in this dissertation research in detail.

2.1 The Accelerator: Relativistic Heavy Ion Collider

“The Relativistic Heavy Ion Collider (RHIC) at Brookhaven National Laboratory (BNL) is a world-class scientific research facility that began operation in 2000, following 10 years of development and construction. Thousands of physicists from around the world use RHIC to study what the universe may have looked like in the first few moments after its creation.” [Sch06]

Figure 2.1 shows the whole RHIC complex [Sch06]. To study Au+Au collision, billions of gold atoms are generated in the Pulsed Sputter Ion Source in the Tandem Van de Graaff. One neutral gold atom is attached with one electron so it becomes -1 charged. The static electrical field accelerates the negative gold ions toward a gold foil, where about 33 (include the attached one) electrons of each negative gold ion are stripped off, so the negative gold ions become positive gold ions. At the other side of the gold foild, the static electrical field in opposite direction further accelerates these positive gold ions and feeds them to the Booster through the Tandem-to-Booster beam line. At this point, they're traveling only at about 5% the speed of light or 1 MeV per nucleon. A spectrometer selects only +32 charged gold ions and feed them to the Booster. The Booster synchrotron is a small circular accelerator that accelerates particles using electromagnetic waves at radio frequency. It accelerates these gold ions to about 37% the speed of light or 95 MeV per nucleon. At the end of the Booster, there is another gold foil where about all the remaining but two electrons are stripped off. Another spectrometer selects +77 charged gold ions and feeds them into the Alternating Gradient Synchrotron (AGS) to be accelerated further up to around 99.7% the speed of light or 10.8 GeV per nucleon. At the end of AGS, there is one more foil to strip the last two electrons off each gold ion and makes it +79 charged. After this, these +79 charged gold ions will be taken down toward the AGS-To-RHIC (ATR) transfer line. At the end of this line, there is a switching magnet sending the ion bunches down to one of the two beam lines: one is clockwise and the other is counter-clockwise. Bunches are directed either left to travel clockwise or right to travel counter-clockwise. RHIC can accelerate these ions up to 100 GeV per nucleon and collide them in any of the six intersection points on RHIC ring.

Table 2.1 lists a summary of the RHIC design parameters and specifications [Che03].

Table 2.1: The RHIC design parameters and specifications.

Physical Parameters	Value	
No. of Intersection Regions	6	
No. of Bunches/Ring	60	
Bunch Spacing (nanosecond)	213	
Collision Angle	0	
Free Space at Crossing Point (m)	16	
Performance Specifications	Au	p
No. of Particles/Bunch	1×10^9	1×10^{11}
Top Energy (GeV/Nucleon)	100	250
Energy Spread (10^{-3})	0.7	0.7
Average Luminosity ($\text{cm}^{-2}\text{sec}^{-1}$)	$\sim 2 \times 10^{26}$	$\sim 1 \times 10^{31}$
Luminosity Life Time (hr)	3	10
Average Beam Current (mA)	55	70

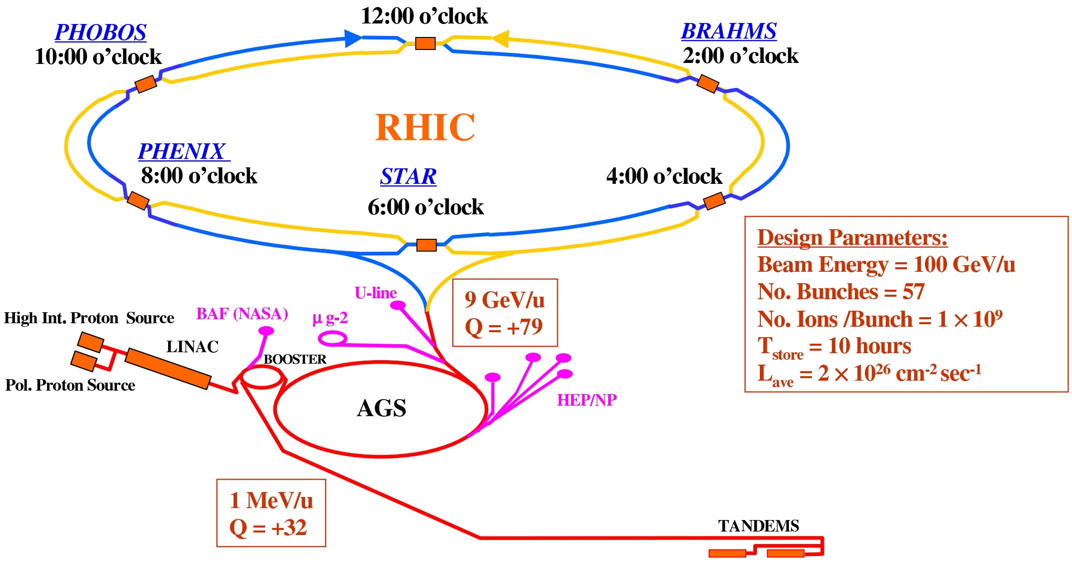

Figure 2.1: Diagram of the RHIC complex at Brookhaven National Laboratory in Long Island, New York.

2.2 The Detector: Solenoid Tracker At RHIC

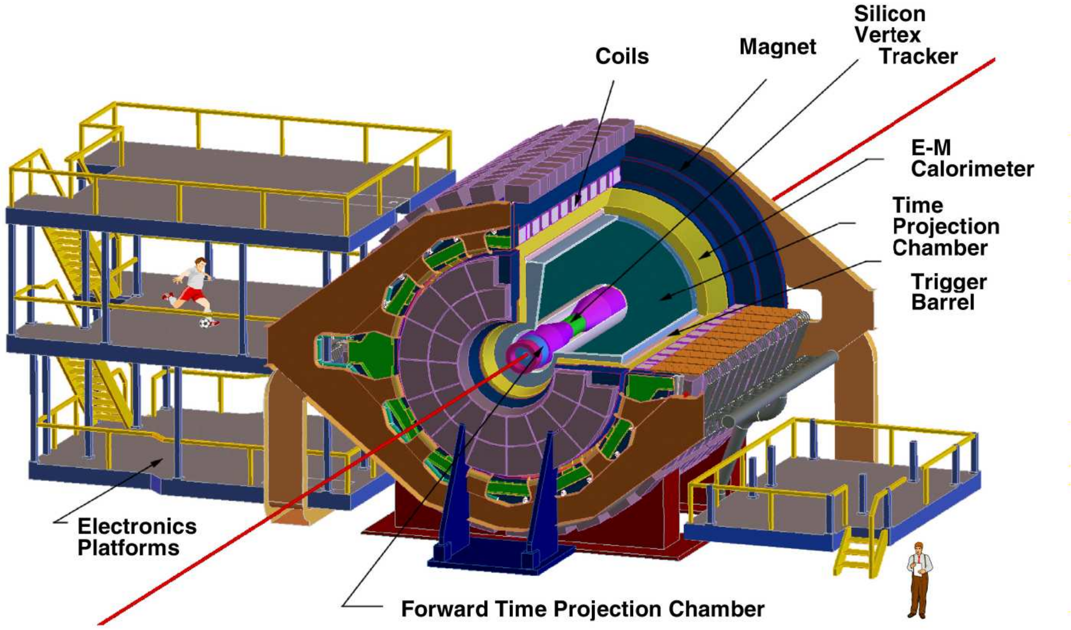

Figure 2.2: The STAR detector system.

The Solenoid Track At RHIC (STAR) is a detector system that consists of several subsystems. It is located at the 6 o'clock position on the RHIC ring. Figure 2.2 shows a perspective view of STAR [Ack03]. It has 2π coverage in azimuthal angle. There are several subsystems in the STAR detector system. Table 2.2 lists their functions.

In this dissertation, information from these three major detectors are used: Time Projection Chamber (TPC), Barrel Electro-Magnetic Calorimeter (BEMC), and Barrel Shower Maximum Detector (BSMD). The TPC is used to identify and measure electron's momentum. The BEMC and the BSMD are used to help identifying electrons.

Table 2.2: The STAR subsystems

Major Detector Subsystem	Major Usage
Zero-Degree Calorimeter (ZDC)	Triggering minimum bias events
Central Trigger Barrel (CTB)	Triggering high multiplicity events
Time Projection Chamber (TPC)	Tracking mid-rapidity charged particles
Forward Time Projection Chamber (FTPC)	Tracking large-rapidity charged particles
Time Of Flight (TOF)	Particle identification
Barrel Electro-Magnetic Calorimeter (BEMC)	Measuring mid-rapidity electrons, positrons and photons, also triggering high p_T events
Endcap Electro-Magnetic Calorimeter (EEMC)	Measuring large-rapidity electrons, positrons and photons

2.2.1 Time Projection Chamber: TPC

The STAR TPC is a tracking detector capable of measuring and identifying charged particles [And03]. It can cover 2π in azimuthal angle and from -1.8 to 1.8 in pseudo-rapidity. The STAR TPC has two cylindrical drift chambers separated by a membrane at high voltage. The chambers are filled with a mixture of 90% argon and 10% methane. There is an inner field cage in each chamber. Each inner field cage has hundreds of consecutive rings with constant voltage difference between two neighboring rings. This configuration offers a uniform electrical field along the Z axis (beam direction) inside the chambers. The ionization electrons drift towards the end-caps of the TPC under the influence of the electrical field. There are 24 anode pad sectors to detect these drifting electrons at the end-cap of each chamber. Outside of the drift chamber, there is a solenoidal magnet providing strong magnetic field up to half a tesla also along the Z axis. Figure 2.3

shows a schematic view of STAR TPC.

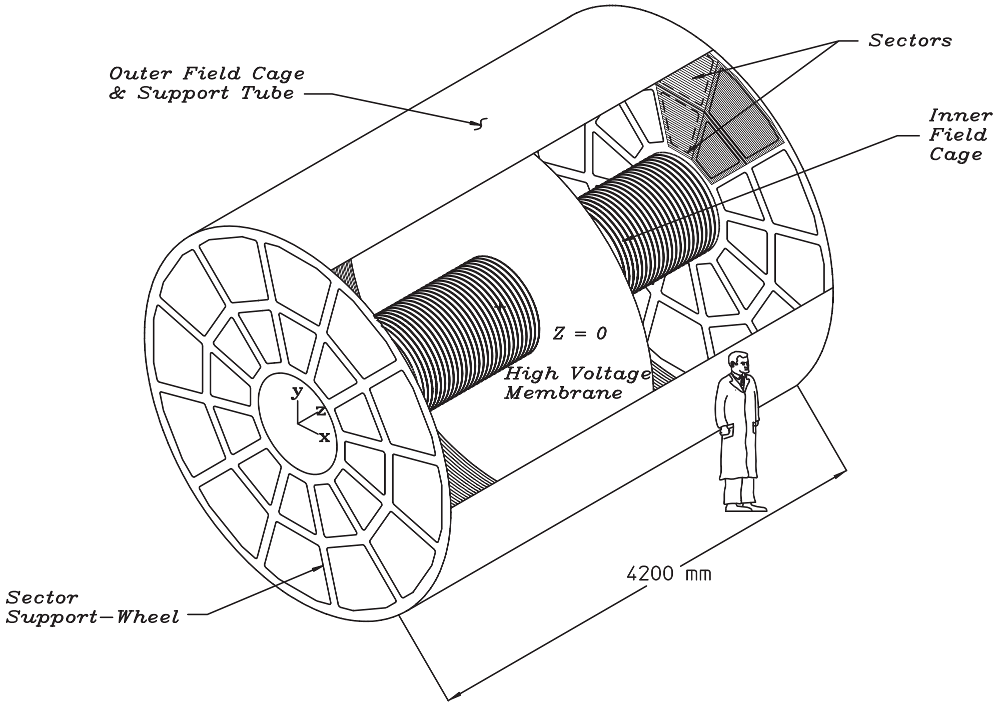

Figure 2.3: The STAR TPC schematic view.

The STAR TPC can track up to 4×10^3 charged particles from a single Au+Au collision. Figure 2.4 shows the first Au+Au collision event recorded by the STAR TPC. The detailed discussion on how the charged particles are reconstructed by the TPC will be in section 3.2.1.

In this dissertation research, the TPC is used as the major detector for inclusive electron identification and measurement. It is also used for photonic background electron removal. In the heavy ion collision environment, the hadron multiplicity is hundreds of times larger than that for the electron, and small misidentification of hadron/electron is disastrous for electron measurements. Thus, the

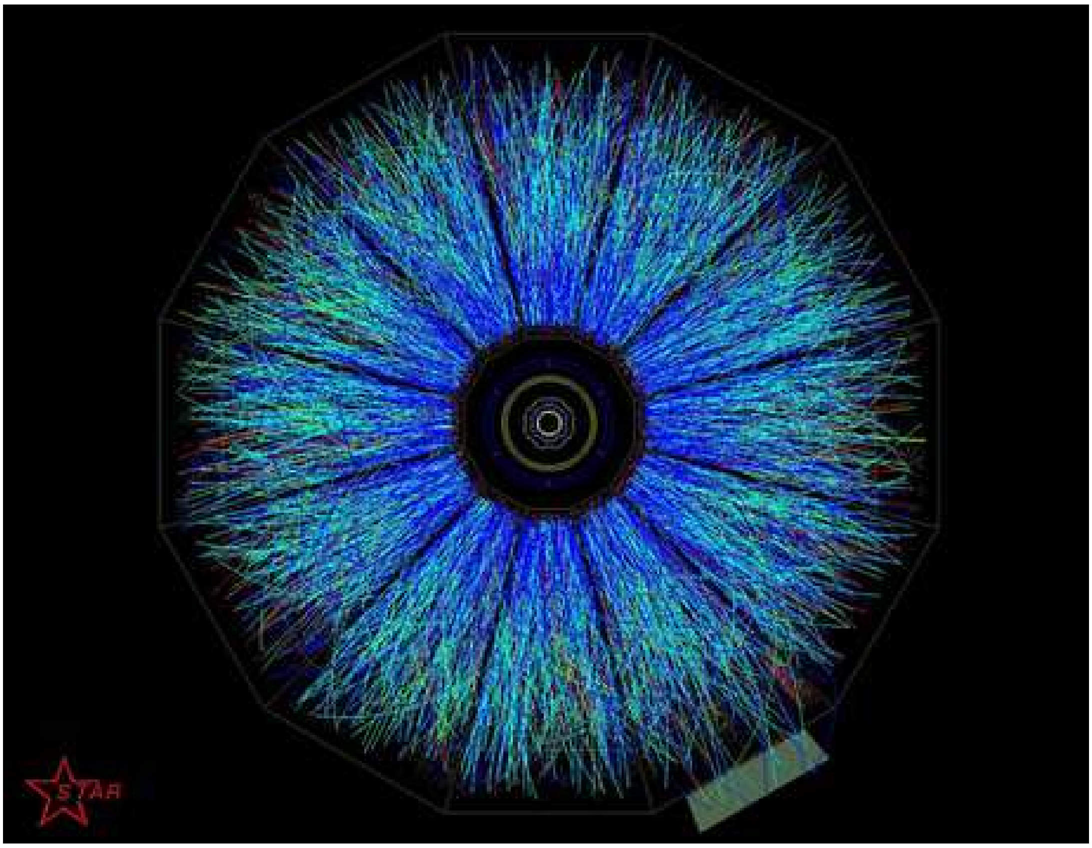

Figure 2.4: First relativistic Au+Au collision recorded by the STAR TPC.

TPC's limited particle identification ability is not enough to completely separate hadrons from electrons in the environment of heavy ion collisions and auxiliary detectors are needed for electron identification. This further particle identification power comes from the Time of Flight (TOF) for the low momentum region, and the Barrel Electro-Magnetic Calorimeter (BEMC) with the Barrel Shower Maximum Detector (BSMD) for the high momentum region. This dissertation focuses on the measurement of high p_T electrons using the BEMC and the BSMD.

2.2.2 Barrel Electro-Magnetic Calorimeter: BEMC

The STAR BEMC and its partner detector the BSMD are critical detectors for electron identification in this dissertation research. They are used in conjunction with the TPC and they provide additional hadron rejection power.

2.2.2.1 Electro-Magnetic Calorimeter Technology

A calorimeter is a device to measure energy. Particles deposit almost all of their energies through the creation and absorption processes when they incident on a block of material in a calorimeter [Fer87]. A fraction of the deposited energy can be measured through the signal from a variety of sources: ionization, scintillation, Cherenkov light, etc.. The total deposited energy as a function of the measured energy can be determined.

There are two major types of calorimeters: homogeneous calorimeters, e.g. CsI(Tl), BGO, Pb-glass, and sampling calorimeters, e.g. Pb-scintillatoror Pb-Ar(liq). In a homogeneous calorimeter, the energy degradation and energy measurement is done by the same material. Homogeneous calorimeters can have good energy resolution but are costly. In a sampling calorimeter, the energy degradation and energy measurement are separated in alternating layers of different material. Sampling calorimeters have inferior energy resolution because they only measure a smaller fraction of the total particle energy. However, they cost less and they are flexible in design and fabrication.

The Electro-Magnetic Calorimeter (EMC) is a device to measure the energy of electrons, positrons and photons. These particles create electro-magnetic showers in the calorimeter. The EMC possesses many useful features that other detectors do not have. Here are a few major features of the EMC:

- Its relative energy resolution improves with increasing energy: $\sigma_E/E \propto 1/n \propto 1/\sqrt{E}$, where n is the number of secondary shower particles and is proportional to the incident energy E. On the contrary, the momentum resolution of tracking detectors in a magnetic field deteriorates with increasing momentum.

- It can measure neutral photons that tracking detectors cannot measure.

- Its necessary longitudinal depth to contain the shower increases logarithmically with particle energy. So a wide energy measurement range can be achieved with a relatively compact size calorimeter. The size of a tracking detector in a magnetic field increases linearly with particle momentum.

- The longitudinal and lateral development of showers in the EMC are different for electrons/photons, and hadrons. Thus the EMC can be used for electron/photon [1] identification.

- It is a intrinsically fast detector so it can be used as a trigger detector.

When a high energy electron, positron or photon is incident on an absorber, it produces a cascade of secondary electrons, positrons and photons via bremsstrahlung and pair production. As the depth increases, the number of secondary particles increases, but their mean energy decreases. When the energies fall below the critical energy ε, the multiplication process stops and energy is dissipated via the processes of ionization and excitation.

ε is defined as the energy when the ionization loss and radiation are equal. It can be calculated approximately as $560/Z(MeV)$, where Z is the number of protons in the nucleus. The radiation length X_0, is the distance in which, on

---

[1] Electrons and photons cannot be separated by the EMC alone. A tracking detector like the TPC can be used to tell them apart.

average, an electron loses $(1 - 1/e)$ of its energy. It is also the length in which a photon has a pair conversion probability of 7/9. X_0 can be approximated as $180A/Z^2(g \cdot cm^2)$, where A is the atomic number. Two scaled variables are useful in the following dicussion:

$$t = \frac{x}{X_0} \tag{2.1}$$

$$y = \frac{E}{\varepsilon} \tag{2.2}$$

Then the average particle energy e(t) and the number of particles n(t) are given by:

$$e(t) = \frac{E}{2^t} \tag{2.3}$$

$$n(t) = 2^t \tag{2.4}$$

At shower maximum:

$$t_{max} = \ln y \tag{2.5}$$

$$n(t_{max}) = y \tag{2.6}$$

As the shower develops it broadens laterally due to multiple scattering of electrons and low energy photons. This can be characterized by the Moliere radius, R_m. R_m is approximately $7A/Z(g \cdot cm^{-2})$. The final shower looks like a narrow core surrounded by a soft halo of scattering particles. An infinite cylinder of radius R_m contains 90% of the shower energy. Figure 2.5 shows the longitudinal and lateral energy loss profiles in electro-magnetic calorimeters.

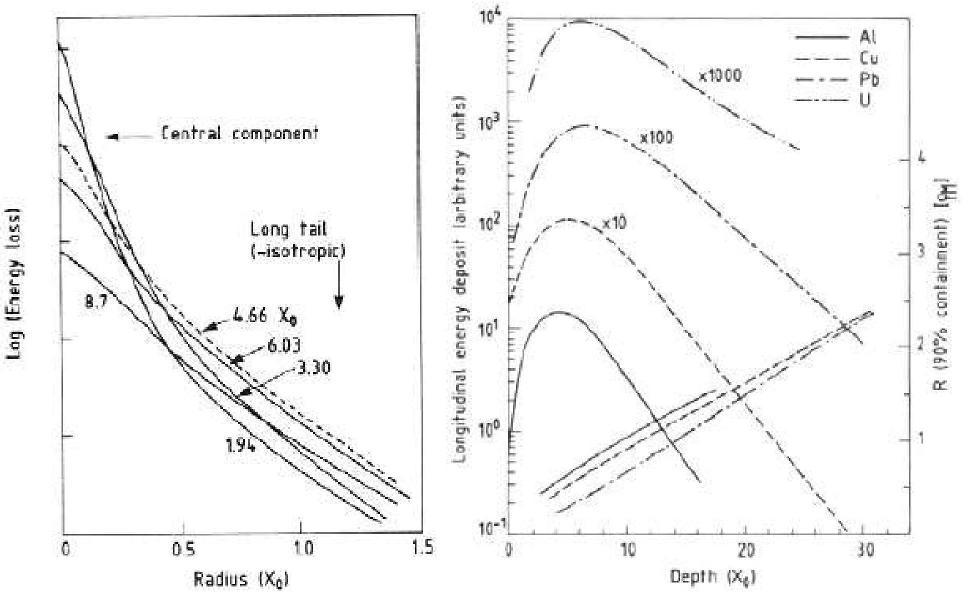

Figure 2.5: The left plot shows the particle energy loss as a function of radius in Electro-Magnetic Calorimeters. The right plot shows particle longitudinal and lateral energy deposition as a function of depth in Electro-Magnetic Calorimeters.

2.2.2.2 Barrel Electro-Magnetic Calorimeter at STAR

The STAR Barrel Electromagnetic Calorimeter (BEMC) is located inside the aluminum coil of the STAR solenoid and outside of the TPC. It covers $|\eta| < 1.0$ and 2π in ϕ [Mat98]. The inner surface of the BEMC has a radius of about 220cm. Figure 2.6 shows the BEMC side view from -Z direction.

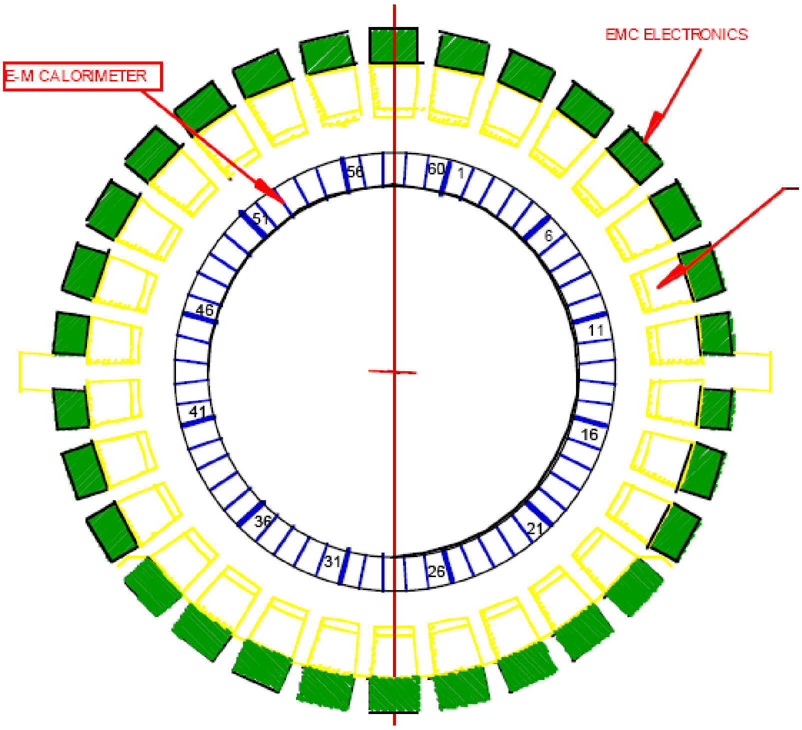

Figure 2.6: The BEMC side view from $-Z$ direction. The numbers are module numbers.

The design for the barrel electromagnetic calorimeter includes a total of 120 calorimeter modules, each covering 6° in $\Delta\phi$ and 1 unit in $\Delta\eta$ [Mat98]. There are 60 modules in +Z and 60 modules in -Z. In year 2004 when the Au+Au 200 GeV experiment was done, only 60 modules in +Z had been installed for operation. Each module is roughly 26cm in width, 293cm in length and 23.5cm in active depth. Each module is segmented into 40 towers, 2 in ϕ and 20 in η, with each tower covering 0.05 in $\Delta\phi$ and 0.05 in $\Delta\eta$. Thus the full BEMC is segmented into a total of 4800 towers and every tower is pointing to the center point of the interaction region. Each module has a shower max detector embedded about 5 radiation length below the inner surface of the BEMC. The BSMD will be discussed in section 2.2.3. Figure 2.7 shows the schematic view of a BEMC module.

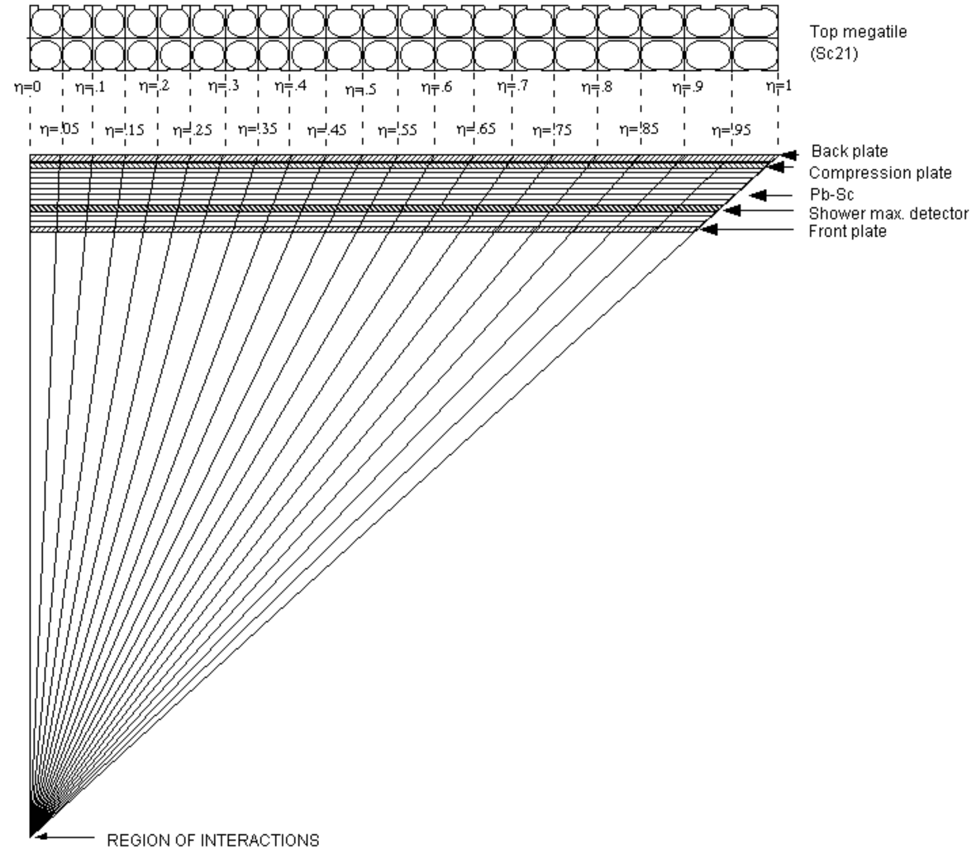

Figure 2.7: The BEMC module side view. The towers are all pointing to the center point of the interaction region.

The STAR BEMC is a sampling calorimeter made by layers of lead and plastic scintillator [Bed03]. This design is cost-effective. Figure 2.8 shows the schematic view of the front of one BEMC module. There are 21 active scintillating layers in

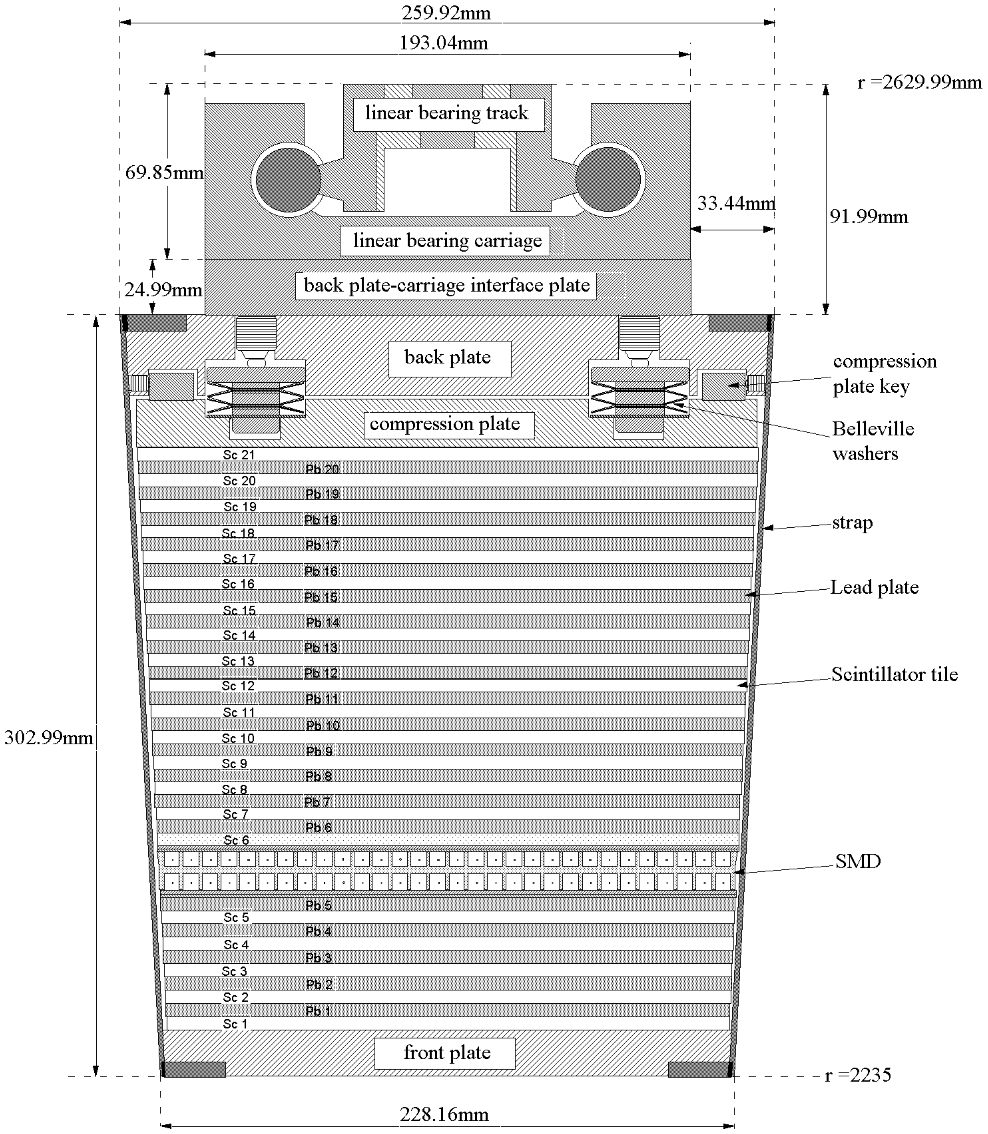

Figure 2.8: The BEMC module cross-sectional view.

the module. Of these 21 layers, 19 of them are $5mm$ in thickness and 2 of them, associated with the pre-shower detector, are $6mm$ in thickness. The scintillator layers alternate with 20 layers of $5mm$ thickness lead absorber plates. Photons from the scintillator layers are collected and transported through the clear optical fibers to the photo multiplier tubes (PMT). Figure. 2.9 shows how this is done.

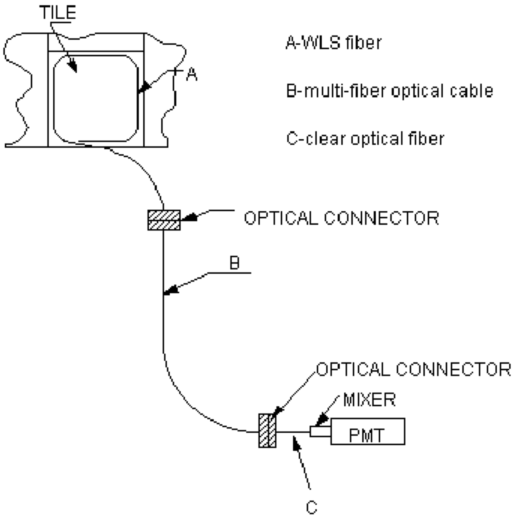

Figure 2.9: The BEMC wavelength-shifting fiber. Each scintillator layer has an optical fiber around it and all the 21 fibers are bundled to give out the total optical output of the tower.

2.2.3 Barrel Shower Maximum Detector: BSMD

The STAR BSMD provides finer spatial resolution and shower profile measurement compared with the BEMC, which has much larger segmentation [Bed03]. Each of the 4800 towers of the BEMC spans $\Delta\phi \times \Delta\eta = 0.05(radian) \times 0.05$ which corresponds to a tower size larger than $10cm \times 10cm$ at the radius of the inner surface of the detector at $\eta = 0$ and increasing toward $\eta = 1$. While the BEMC towers provide precise energy measurements for isolated electromagnetic showers, the high spatial resolution and shower profile information provided by the BSMD is essential for π^0 reconstruction, direct γ identification, and electron identification. Figure 2.10 shows the conceptual design of the STAR BSMD. It is located at about 5 radiation lengths depth from the inner surface of the BEMC modules. Figure 2.5 shows that the shower usually develops to its maximum at a depth around 5 radiation lengths.

The STAR BSMD has a double layer design. A two sided aluminum extrusion provides ground channels for two independent planes of gold plated tungsten wires. Each of these wires spans $\Delta\eta = 1$ on each side of the extrusion. There are two independent PC board cathode planes with strips etched in the η and ϕ directions respectively to sense the induced charge from the charge amplification near the wires. These perpendicular strips allow reconstruction of a two dimensional image of the shower. One set of strips are called the η strips. These η strips are perpendicular to the wires and provide an image of the shower spatial distribution in the η direction. Each of these η strips spans $\Delta\phi \approx 0.1(radian)$, which corresponds to the module width of about $23cm$. There are two groups of η strips. One group is narrower and each narrower strip spans about $1.537cm$ in Z. There are 75 of these narrower strips spanning from 0 to 0.5 in η. The other group is wider and each wider strip spans about $1.961cm$ in Z. There are

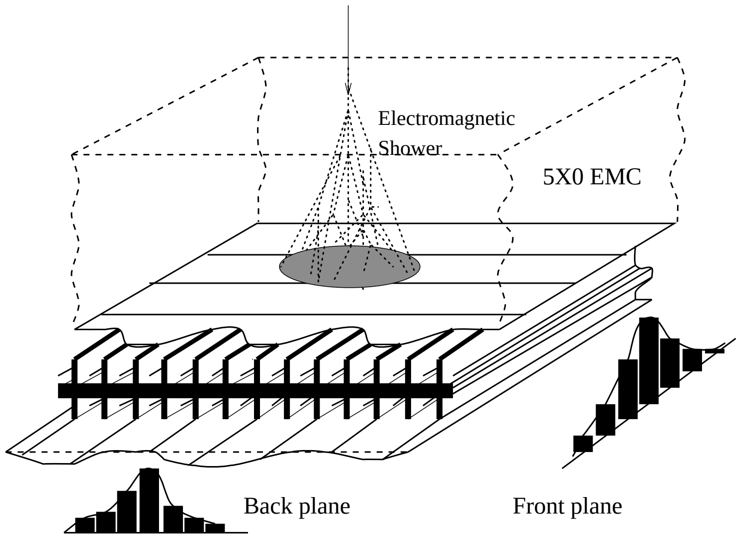

Figure 2.10: Schematic illustration of the double layer STAR BSMD. Two independent wire layers separated by an aluminum extrusion image electromagnetic showers in the η and ϕ directions on corresponding pad layers.

also 75 of these wider strips spanning from 0.5 to 1 in η. The other set of strips are called the ϕ strips. ϕ strips are parallel to the wires. These strips are about $1.33cm$ in width and 0.1 units in η. 15 of these strips form a patch/sub-division, which spans $\Delta\phi \approx 0.1$ and $\Delta\eta = 0.1$. There are 10 patches in each module. The BSMD is essentially a multi-wire proportional chamber, in which the strips read out signals using gas amplification. Some important features of the double sided BSMD design include improved reliability, improved functionality in high occupancy environment, improved hadron rejection and γ/π^0 separation and simplified mechanical construction. Figure 2.11 shows the schematics of the wires and strips in a STAR BSMD module.

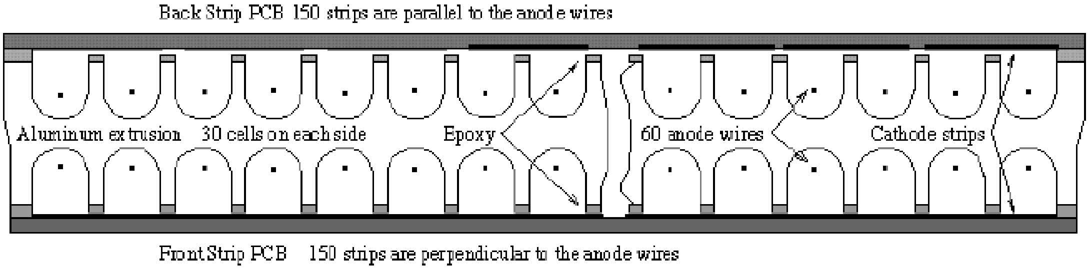

Figure 2.11: Cross sectional view of the STAR BSMD showing the extruded aluminum profile, the wires and cathode strips.

The STAR BSMD design parameters and specifications are summarized in table 2.3.

The BSMD has been extensively evaluated in test beams at the AGS. The position resolution in the front and back planes of the BSMD have been measured and the resolution in the front and back planes was found to be given approximately by

$$\sigma_{front}(mm) = 2.4mm + 5.6mm/\sqrt{E}(GeV) \tag{2.7}$$

Table 2.3: The STAR BSMD design parameters and specifications

Parameter	Value
Chamber Position inside EMC	$\sim 5X_0$ at $\eta = 0$
Rapidity Coverage (Single Module)	$\Delta\eta = 1.0$
Azimuthal Coverage (Single Module)	$\Delta\phi = 0.105$ (6°)
Occupancy (p+p)	$\sim 1\%$
Occupancy (Au+Au)	5% to $\sim$ 25% (depends on the threshold)
Chamber Depth (Cathode to Cathode)	$20.6mm$
Anode Wire Diameter	$50\mu m$
Gas Mixture	$90\%Ar$ and $10\%CO_2$
Gas Amplification	~ 3000
Signal Length	$110ns$
Strip Width (Pitch) in η for $\|\eta\| < 0.5$	1.46 (1.54) cm
Strip Width (Pitch) in η for $\|\eta\| > 0.5$	1.88 (1.96) cm
Strip Width (Pitch) in ϕ	1.33 (1.49) cm
Number of Strips per Module	300
Total Number of Modules	120
Total Number of Readout Channels	36000

$$\sigma_{back}(mm) = 3.2mm + 5.8mm/\sqrt{E}(GeV) \tag{2.8}$$

By using the STAR year 2003 d+Au 200 GeV data, the position resolution of the BSMD η is found to be less than $7.4mm$ on average and the position resolution of the BSMD ϕ is found to be around $6.6mm$ on average. The results are from the study of TPC reconstructed tracks' projection onto each BSMD plane. Track projection is discussed in detail in section 3.2.3.

CHAPTER 3

Data Analysis

This chapter is divided into two parts. The first part is about the event specific analysis, which includes trigger selection, centrality selection, event vertex cut, reaction/event plane azimuthal angle calculation, etc. The second part is about track specific analysis, which includes charged track reconstruction, inclusive electron identification, background electron removal, signal electron's correlation with reaction plane, etc.

3.1 Event Specific Analysis

In year 2004, about 80 million Au+Au collisions were recorded by STAR. By the time when this dissertation was written (February 23, 2006), about 29.5 events with valid BEMC information were processed by the STAR production team. After various event selection and cuts about 9 million minimum biased events were used to produce the results that are shown in this dissertation. Figure 3.1 shows a detailed tally of the events been analyzed for this dissertation research.

The event selection and cuts are listed in table 3.1 and here is a brief discussion of how each cut is determined.

In a relativistic heavy ion collision, the event centrality is determined by the impact parameter b, which is the distance between the centers of two colliding nuclei [Gla59]. The impact parameter b is not observable but it is correlated with

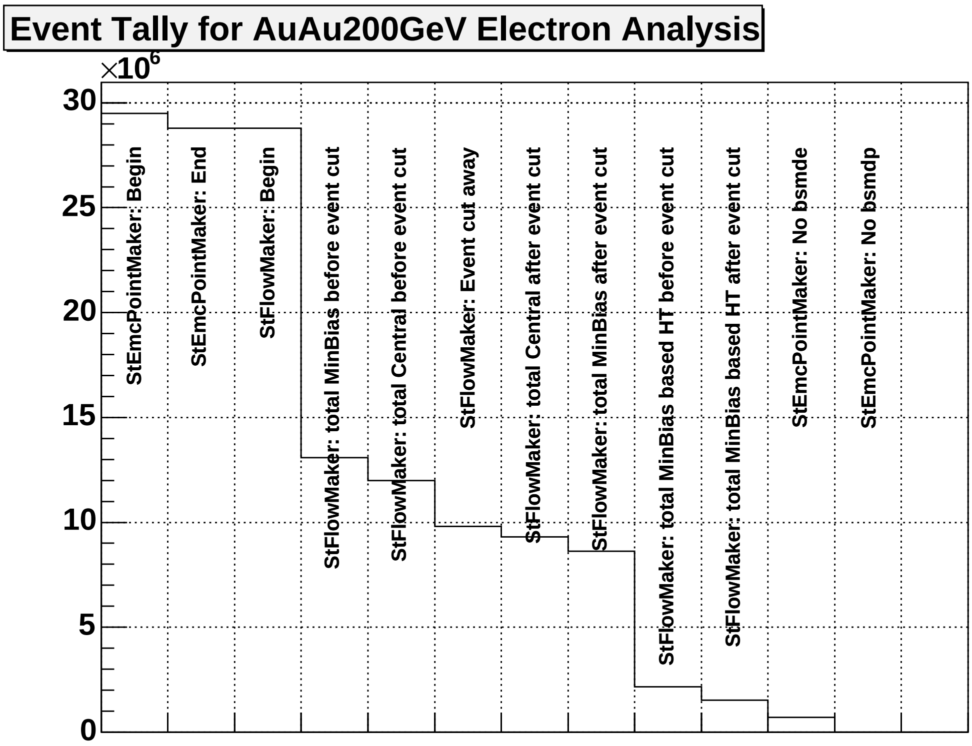

Figure 3.1: Detailed event statistics for Au+Au 200 GeV electron v_2 analysis. Only events with valid BEMC information, minimum bias trigger and qualifying vertex are kept.

Table 3.1: Event selection and cuts.

Parameter	Value	Comments
Trigger	minimum bias	To compare with other measurements and theoretical predictions
Centrality	0-80%	To compare with other measurements and theoretical predictions, and to avoid ambiguity between different models
Vertex Z	$(-20cm, 20cm)$	To avoid photon conversion electrons

the multiplicity of the event. The higher the multiplicity, the smaller the impact parameter and the more central the collision. In STAR, the reference multiplicity is used in the determination of the centrality. The reference multiplicity is defined as the number of tracks satisfying the following requirements:

- Flag>0 (a basic track reconstruction quality requirement)
- Distance of Closest Approach (DCA) to the primary vertex $< 3cm$
- Number of fit points ≥ 10
- $-0.5 < \eta < 0.5$

The reference multiplicity distribution is binned into percentiles of the total cross section. Each percentile corresponds to each centrality bin. 0 to 5% is for the most central collisions. The average number of binary collisions N_{bin} and the average number of participants N_{part} for each percentile can be calculated using Glauber model. However, two methods are used to calculate the N_{bin} and N_{part}. One is called *Optical* Glauber approach and the other is called *Monte Carlo* Glauber approach. The difference between these two is negligible for central Au+Au collisions, but is significant for peripheral Au+Au collisions [Ada03a]. Thus, in this analysis, only events within the centrality interval from 0 to 80% are selected. Table 3.2 lists the STAR centrality definition for year 2004 Au+Au 200 GeV experiment [Dun04]. Figure 3.2 and Figure 3.3 show the reference multiplicity and centrality distributions for Au+Au 200 GeV minimum biased events.

The cut on vertex Z was chosen to be $(-20cm, 20cm)$. Studies found that events with vertex Z outside this range have much larger fraction of photon conversion electrons [STA05].

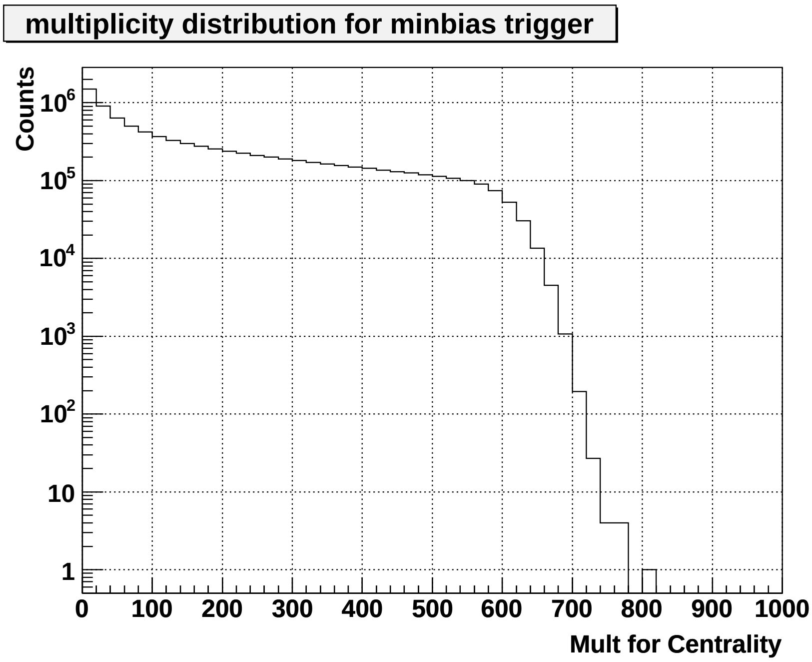

Figure 3.2: The STAR reference multiplicity distribution for Au+Au 200 *GeV* minimum biased events. The reference multiplicity is not the multiplicity of the event. It is solely used for the determination of the centrality.

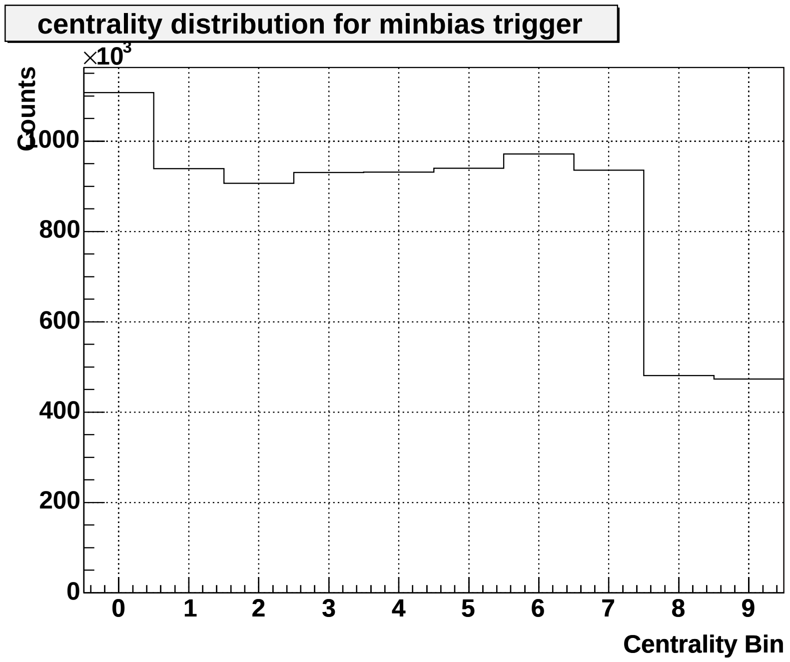

Figure 3.3: Centrality bin distribution for Au+Au 200 *GeV* minimum biased events. From bin 9 to bin 0 are 0-5%, 5-10%, 10-20%, 20-30%, 30-40%, 40-50%, 50-60%, 60-70%, 70-80%, and 80-100%. Equal width percentile has consistent number of entries and half width percentile (0-5% or 5-10%) has half the number of entries of the other percentiles. 80-100% is an abnormal percentile where Optical Glauber model and Monte Carlo Glauber model do not agree with each other.

Table 3.2: The STAR centrality definition for year 2004 Au+Au 200 GeV experiment.

Centrality	N_{par}	N_{bin}	Reference Multiplicity
0-5%	352.4 +3.4 -4.0	1051.3 + 71.5 -71.1	$[520, \infty)$
5-10%	299.3 +6.6 -6.7	827.9 +63.9 -66.7	[441, 520)
10-20%	234.6 +8.3 -9.3	591.3 +51.9 -59.9	[319, 441)
20-30%	166.7 +9.0 -10.6	368.6 +41.1 -50.6	[222, 319)
30-40%	115.5 +8.7 -11.2	220.2 +30.0 -38.3	[150, 222)
40-50%	76.6 +8.5 -10.4	123.4 +22.7 -27.3	[96, 150)
50-60%	47.8 +7.6 -9.5	63.9 +14.1 -18.9	[57, 96)
60-70%	27.4 +5.5 -7.5	29.5 +8.2 -11.3	[31, 57)
70-80%	14.1 +3.6 -5.0	12.3 +4.4 -5.2	[14, 31)

From equation 1.2, the reaction plane azimuthal angle is needed for the calculation of v_2. While the real reaction plane azimuthal angle is unknown, a parameter called the event plane azimuthal angle can be used in its place. The definition of the event plane azimuthal angle is [PV98]:

$$\Psi_{EP} = \arctan \frac{\sum_i w_i \sin(n\phi_i)}{\sum_i w_i \cos(n\phi_i)} \tag{3.1}$$

Each sum goes over all the particles used in the event plane azimuthal angle determination, while ϕ_i is the azimuthal angle of the ith particle and w_i is the weight for the ith particle. So, to get the event plane azimuthal angle, one can just collect all the tracks in the event and use equation 3.1 to calculate it. However, there are a few problems in doing this [PV98].

First of all, if the particle of which the v_2 is measured is also included in the event plane azimuthal angle calculation, auto-correlation is introduced. Auto-correlation tends to bias the v_2 towards bigger value. To avoid auto-correlation, one event is divided into two sub-events by randomly dividing all the tracks. To calculate the particle's v_2 without introducing the auto-correlation, the event plane azimuthal angle of the sub-event that does not include that particle is used.

Secondly, tracks with bad quality should not be used. A few basic quality cuts are needed to exclude bad tracks. Table 3.1 lists the cuts been used.

Value	Cut	Comments
Number of fit points	≥ 20	To ensure basic track quality
(Number of fit points)/(Number of maximum fit points)[1]1	> 0.52	To avoid track multiple counting

Table 3.3: Basic track quality cuts

Finally, the event plane azimuthal angle is only an approximation for the reaction plane azimuthal angle. It is an experimentally measured parameter, so it has limited resolution. The limited event plane azimuthal angle resolution will smear the particle-plane correlation. So the approximation of reaction plane azimuthal angle by event plane azimuthal angle will "dilute" the v_2 signal. This effect should be corrected.

The event plane azimuthal angle resolution can be improved by assigning non-uniform weights to the tracks in the event. Due to the structure, the STAR TPC has slightly different tracking efficiency for tracks of different azimuthal angle and different topology. Figure 3.4 shows the track's ϕ distribution for 4 different topologies: far east ($\eta < 0$ & $Z_{vertex} < 0$), far west ($\eta > 0$ & $Z_{vertex} > 0$), east ($\eta < 0$ & $Z_{vertex} > 0$) and west ($\eta > 0$ & $Z_{vertex} < 0$). The non-

---

[1] The number of fit points is the number of space points been used to fit a track trajectory (a helix). The number of maximum fit points is the number of possible space points available for a given helix topology.

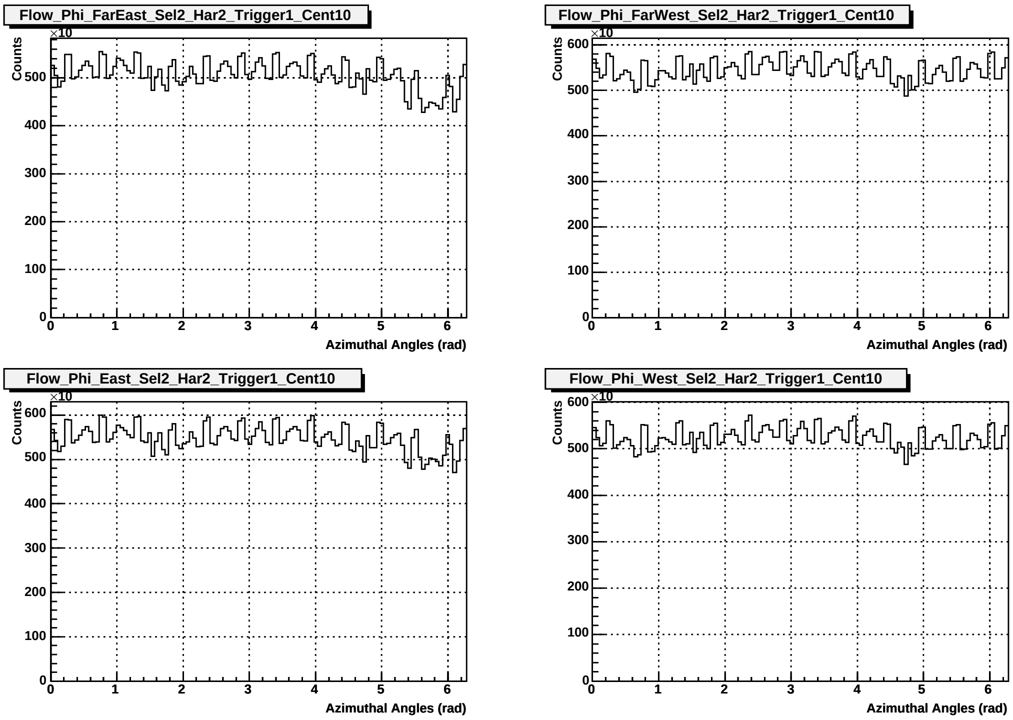

Figure 3.4: Track's ϕ distributions in Au+Au 200 GeV minimum biased events. The top left is for $\eta < 0$ & $Z_{vertex} < 0$, top right is for $\eta > 0$ & $Z_{vertex} > 0$, bottom left is for $\eta < 0$ & $Z_{vertex} > 0$ and bottom right is for $\eta > 0$ & $Z_{vertex} < 0$. From these plots, the structure of 24 sectors in the STAR TPC is visible. The dips are from the gaps between two consecutive sectors.

uniform efficiency lowers the event plane azimuthal angle resolution. This effect of reduced resolution can be reduced by assigning non-uniform weights to the each track according to its ϕ angle and topology. The weight for each ϕ bin is just proportional to the inverse of the bin content from the original ϕ histogram. So to generate ϕ weight, one need to collect tracks satisfying cuts listed in table 3.1 and fill their ϕ into ϕ histograms showing in Figure 3.4. Because the detector condition differs from run to run thus efficiency differs from run to run, so for each run there is a ϕ weight. Also because the tracking efficiency depends on event centrality, ϕ weight is further categorized by the centrality. Finally, only tracks from minimum biased events are collected to generate the ϕ weight. Events with any other trigger are biased events. For example, high p_T events triggered by BEMC can have non-uniform track distribution in ϕ because some of the BEMC modules are missing from time to time. After applying the ϕ weight, the weighted ϕ distributions are almost flat. Figure 3.5 shows the weighted ϕ distributions. Figure 3.6 shows the event plane azimuthal angle distribution with this weighting scheme. A very uniform Ψ distribution is achieved.

The weighting method can improve event plane azimuthal angle resolution but it cannot perfect it. The smearing effect caused by the limited event plane azimuthal angle resolution must be corrected. If the reaction plane azimuthal angle in equation 1.2 is substituted by the event plane azimuthal angle Ψ_{EP}, the observed v_2 is measured:

$$v_2^{obs} =< \cos[2(\phi - \Psi_{EP})] > \tag{3.2}$$

To correct for the smearing effect, one has to divide the v_2^{obs} by a “less than one” resolution correction factor [PV98]:

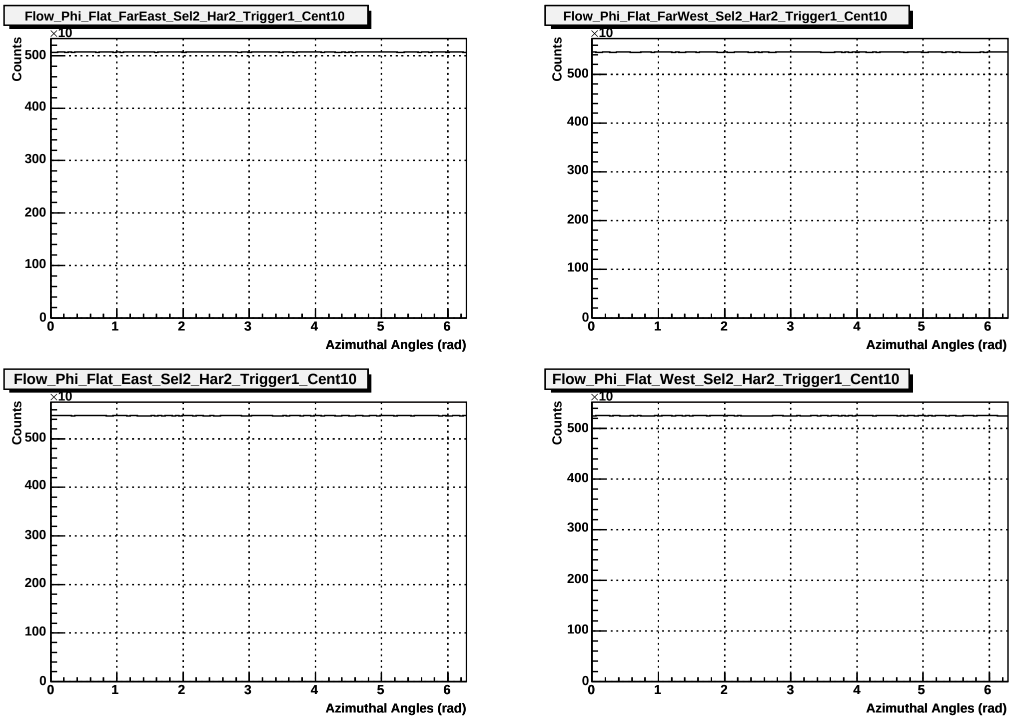

Figure 3.5: Track's weighted ϕ distributions in Au+Au 200 GeV minimum biased events. Theoretically, these distributions should be perfectly flat. But they might not due to computing uncertainties (dead jobs).

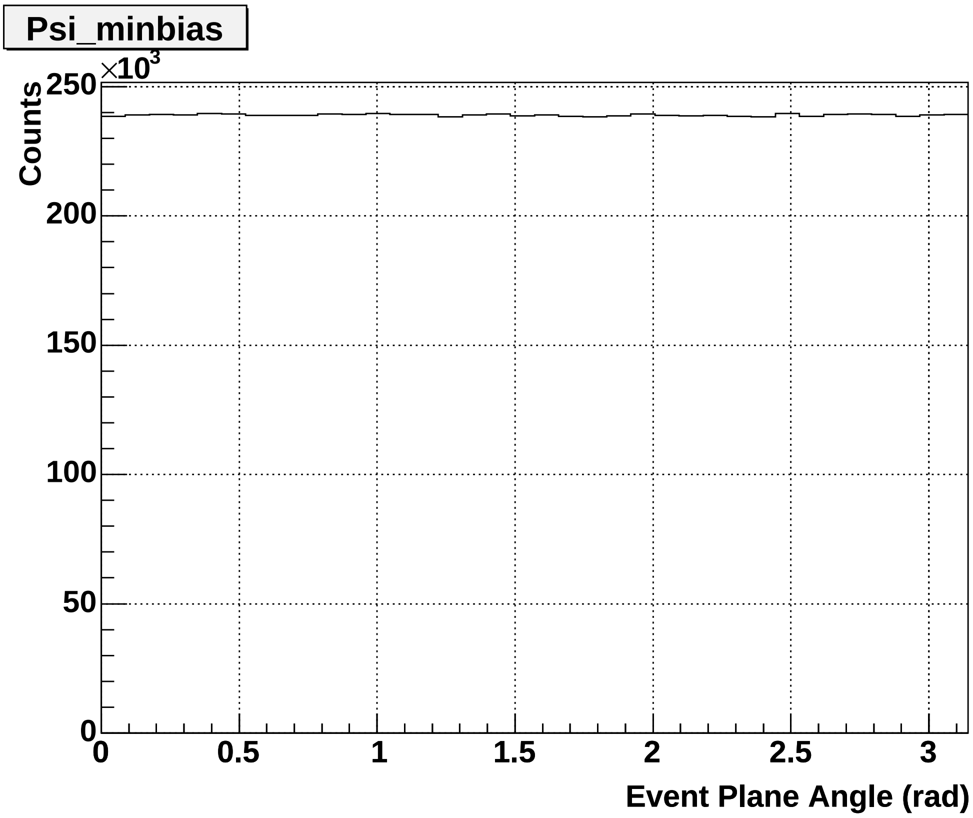

Figure 3.6: Event plane azimuthal angle distribution for Au+Au 200 GeV minimum biased events. Un-uniform weights are used in the event plane azimuthal angle calculations. With uniform weights, the distribution is not as flat as this.

$$v_2 = v_2^{obs} / < \cos[2(\Psi_{EP} - \Psi_{RP})] > \tag{3.3}$$

If sub-event plane azimuthal angle is used for v_2 calculation, then [PV98]:

$$< \cos[2(\Psi_{EP}^a - \Psi_{RP})] >= \sqrt{< \cos[2(\Psi_{EP}^a - \Psi_{EP}^b)] >} \tag{3.4}$$

where Ψ_{EP}^a is the event plane azimuthal angle of one sub-event and Ψ_{EP}^b is the event plane azimuthal angle of another sub-event. Figure 3.7 shows the correlation of Ψ_{EP}^a and Ψ_{EP}^b for minimum biased events. From it, the event plane resolution correction factor can be calculated by equation 3.4. In the analysis, the event plane resolution correction factor is calculated for each centrality bin and the final 0-80% minimum biased event plane resolution correction factor is a weighted average of these small bin event plane resolution correction factors, where the weight is the average reference multiplicity for each bin. Figure 3.8 shows the event plane resolution correction factor for each centrality bin. For low multiplicity events, event plane resolution is poor due to the small number of tracks. For high multiplicity events, the event plane resolution deteriorates because the central collision events intrinsically do not possess big azimuthal anisotropy so there is not much correlation between Ψ_{EP}^a and Ψ_{EP}^b. Figure 3.9 shows the weighted event plane resolution correction factors for merged centrality bins.

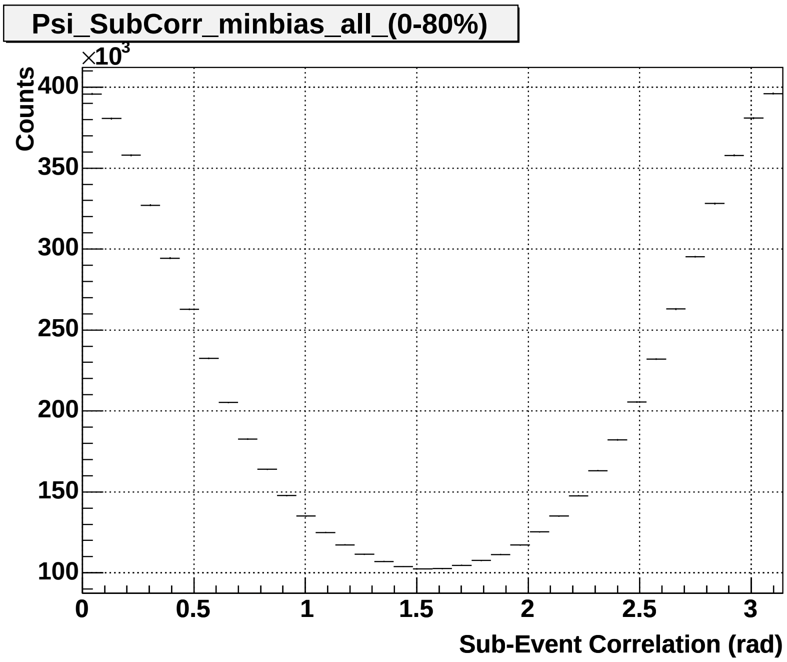

Figure 3.7: Sub-event plane azimuthal angle correlation for Au+Au 200 *GeV* minimum biased events. The X-axis is $|\Psi^{a}_{EP}$-$\Psi^{b}_{EP}|$. The 0-80% Au+Au 200 *GeV* minimum biased event plane resolution correction factor is **NOT** calculated from this histogram. It is calculated as the weighted average of the event plane resolution correction factor in each centrality bin within 0-80%.

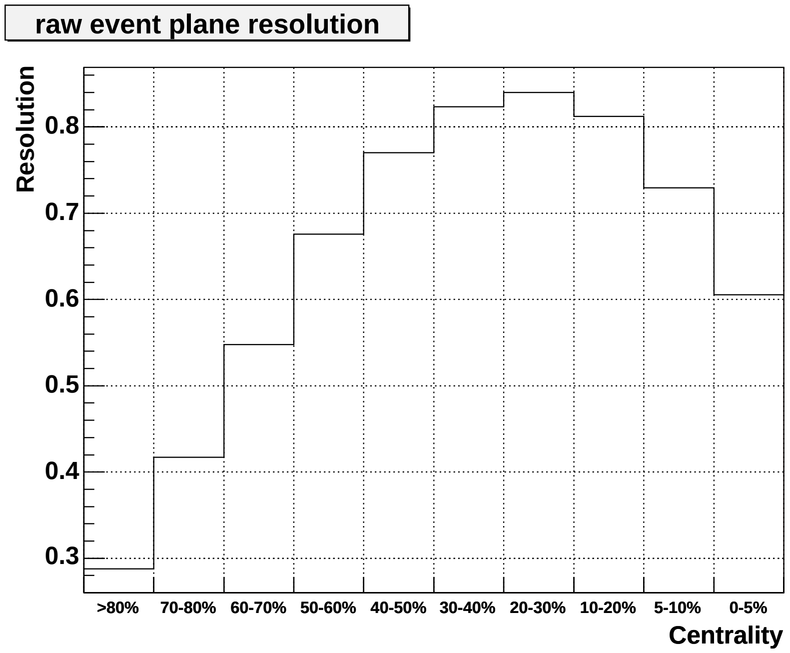

Figure 3.8: Raw event plane resolution correction factor for Au+Au 200 *GeV* minimum biased events. This raw event plane resolution correction factor is calculated from equation 3.4 and sub-event plane azimuthal angle correlation histogram like the one in Figure 3.7. The mid-centrality events have the best event plane resolution.

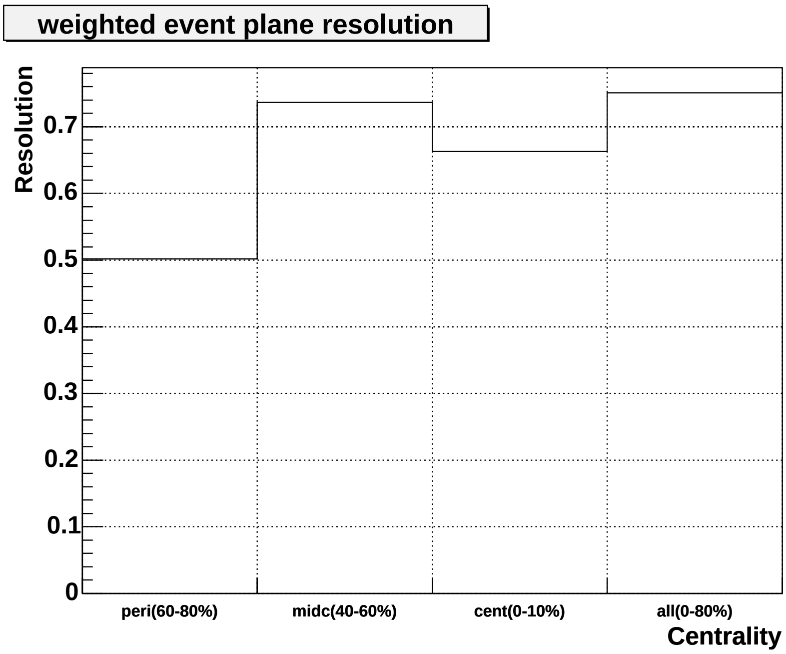

Figure 3.9: Weighted event plane resolution correction factor for Au+Au 200 GeV integrated centrality intervals.

3.2 Track Specific Analysis

3.2.1 Charged Tracks Reconstruction by TPC

When a charged particle travels through a TPC chamber, it ionizes the TPC gas molecules along its path [Leo87]. The ionization will produce positively charged ions and negatively charged electrons. The uniform electrical field along the Z direction causes the negative electrons to drift towards the end-cap anode pads. In each anode pad, there are multiple anode wires. When the drifting electrons are very close to a anode wire, the strong electrical field around the anode wire causes an avalanche and the movement of the avalanche ions induces current on the cathode pad planes. The magnitude of the induced current, which can be measured, is a function of the amount of drifting electrons. And the amount of electrons in turn is a function of the ionization energy loss (dE/dx) of the charged particle. Careful calibration can translate the measured current magnitude to the ionization energy loss dE/dx.

On the other hand, the trajectory of a charged particle in the TPC is a helix due to the magnetic field along the Z direction. The precise gas mixture and uniform electrical field make the drift velocity of ionization electrons constant thus the ionization position can be easily determined by the arrival time of the signal, thus the helix can be reconstructed via the ionization positions. Then the momentum of the charged particle can be calculated from the helix with the magnetic field known. For a certain TPC gas mixture, dE/dx is a function of particle's momentum and different particles follow different function. From Bethe-Bloch theory, dE/dx is a function of the β and the charge of a particle: $dE/dx = Z^2 f(\beta)$. When a plot of dE/dx versus particle's momentum is made, there is a different curve for each different particles. Figure 3.10 shows the ionization energy loss dE/dx as a function of momentum P of different particles measured by the STAR TPC [And03]. Different particles form different bands.

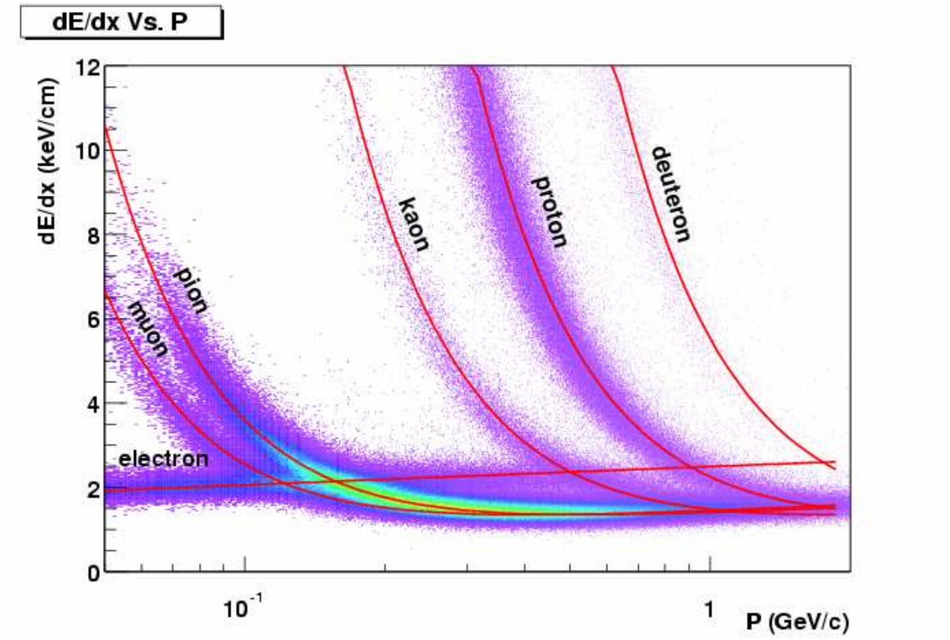

Figure 3.10: dE/dx v.s. P measured by the STAR TPC. Different particle species form different bands.

3.2.2 Electro-Magnetic Particles Reconstruction by BEMC and BSMD

After passing through the TPC, electrons and photons will go into the BEMC towers, create electro-magnetic showers and deposit all their energies in the BEMC. The BEMC is used to measure the energies of these particles. The BSMD, which is about 5 radiation length below the inner surface of BEMC, is used to measure the positions and the sizes of the showers. We have developed a software package to reconstruct electro-magnetic particles by reconstructing their showers in the BEMC. This section will discuss how these electro-magnetic particles are reconstructed and compare UCLA developed software with that from the STAR library.

Here are a few definitions that are used for this section:

Tower/Strip: the physical detecting channel in the BEMC/BSMD detector.

Hit: a tower or a strip that has an energy larger than a certain threshold.

Cluster: a bunch of hits that are geometrically close to each other but not necessarily next to each other.

Cluster Finder: the process or code to group closely distributed hits to clusters. It's called *StPreEclMaker* in the STAR library.

BEMC Point: the final output of the BEMC reconstruction.

"*1:n:m Situation*": when one tower cluster has n η cluster(s) underneath and m ϕ cluster(s) underneath.

Point Maker: the process or code to make the BEMC points out of the BEMC and BSMD clusters. It's called *StEpcMaker* in the STAR library. In the UCLA developed package, the cluster finder and point maker are combined into one program called *StEmcPointMaker*.

Sub-division: a $\Delta\eta = 0.1$ region on a module, i.e., $0 < \eta < 0.1$, $0.1 < \eta <$

0.2 etc. There are exactly 4 BEMC towers in each BEMC tower sub-division. There are exactly 15 BSMD ϕ strips in each BSMD ϕ sub-division. There are 14 to 16 BSMD η strips in each BSMD η sub-division.

All the plots in this section are based on the analysis of the STAR's year 2003 d+Au full field 200 GeV data.

Figure 3.11 is one example of what a typical module behaves in a d+Au 200 GeV event. From the top three 2-D histogram, it is obvious that two BEMC points should be reconstructed in this module for this event.

3.2.2.1 BEMC Point Reconstruction Software in STAR Library

Figure 3.12 shows the flow diagram for the BEMC point reconstruction chain in STAR library. At the beginning of the chain, raw ADC values of towers and strips are read out. Then in *StEmcAdcToEMaker*, calibration constants and status tables from the run to run database are applied to get the right energies from raw ADC values. Then *StPreEclMaker*, which is the cluster finder, clusters tower and strip hits. *StPreEclMaker* does clustering module by module. It does clustering independently and unconditionally on three detectors on three planes: BEMC towers, BSMD η strips, BSMD ϕ strips. It uses fixed threshold (only adjustable in the runtime macro) for clustering: minimum seed energy and minimum add-on energy. A tower or a strip has to have an energy above minimum seed energy to be considered as the first tower or strip of a new cluster. A tower or strip has to have an energy above minimum add-on energy to be considered as a part of an existing cluster. Finally *StEpcMaker* matches clusters on three planes and makes BEMC points out of the matched tower clusters BSMD η clusters and BSMD ϕ clusters. It divides $|\eta|$ range from 0 to 1 into 10 sub-divisions, and categorizes tower clusters, BSMD η clusters and BSMD ϕ clusters according to their η values

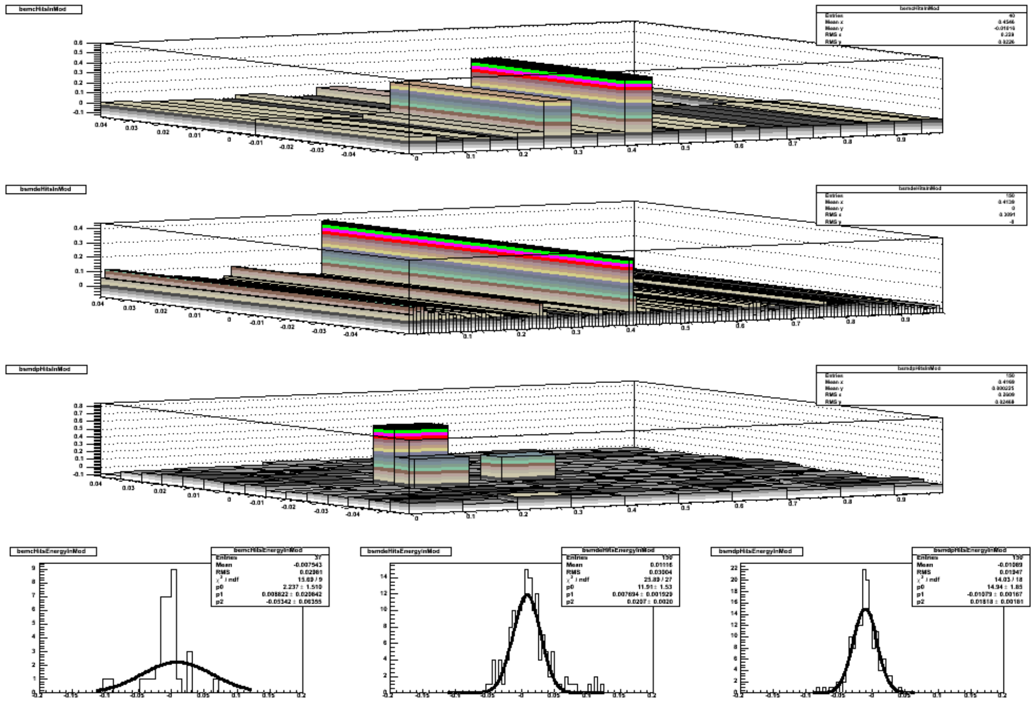

Figure 3.11: The behavior of a module in a typical d+Au 200 GeV event. X and Y in the top three 2-D histograms are not to scale. The top row is a 2-D histogram showing the energies of 40 BEMC towers in a module in one event. The second row is a 2-D histogram showing the energies of 150 BSMD η strips in a module in one event. The third row is a 2-D histogram showing the energies of 150 BSMD ϕ strips in a module in one event. In these three 2-D histograms, X axis indicates η, Y axis indicates ϕ, and Z axis indicates energy. The three 1-D histograms in the bottom row are the 1-D energy spectra of 40 BEMC towers, 150 BSMD η strips and 150 BSMD ϕ strips from left to right. The two 1-D histograms for BSMD strip energies give us an idea of where the clustering thresholds should be placed. The fitting quality of the 1-D histogram for tower energies is not very good, thus the fitting parameters are not used for the determination of tower clustering thresholds. Some of the real hits are far away from the pedestal peaks so they may not be visible in these 1-D histograms.

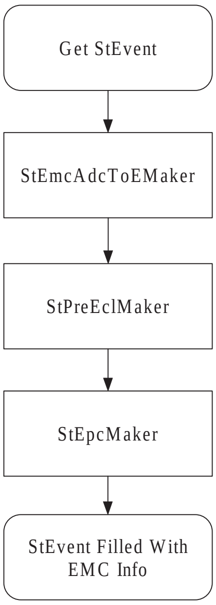

Figure 3.12: The STAR library BEMC point reconstruction chain.

(a tower cluster or a ϕ cluster can have η value too). Then it matches them by the η sub-division that they fall into. After matching is finished, the *StEpcMaker* will make BEMC points out of matched clusters. For "1:1:1" situation when there is no ambiguity, it simply gives out one BEMC point, with the energy from tower cluster, η from BSMD η cluster, and ϕ from BSMD ϕ cluster. For "1:n:m" situation, it will give out $min(n, m)$ BEMC points, and share the tower cluster's energy among these points. The ratio of the energy sharing depends solely on the ratio of the BSMD cluster energies.

It has a few drawbacks. Firstly it has fixed clustering thresholds, but the modules differ and the events differ. Each module uses its own electronic circuit board and the pedestal level depends on the electrical elements used on the circuit board. And also the pedestal level tends to shift with time. So we need variable thresholds. Secondly, it does clustering independently and unconditionally.

However, especially in low occupancy experiment, most of the tower modules will have no hit at all. In that case, it is not necessary to cluster the BSMD modules below. Unconditional and independent clustering is a waste of CPU time. This amount of CPU time is trivial in the whole STAR production process. But for a single user's analysis, which consists only a few simple makers in the analysis chain, this amount of CPU time is not negligible. Thirdly, for BSMD ϕ clustering, it does not go across sub-divisions. It is obvious that a ϕ cluster has non-negligible probability to fall across two sub-divisions. This is one origin of reconstruction inefficiency. Figure 3.13 shows when such a case happens. Finally, it uses fixed window for cluster-matching. It divides η range from 0 to 1 into 10 fixed sub-divisions and categorizes all clusters according to their η values. As we know, the BEMC tower has big granularity, thus it has bad space resolution. For the case when a shower happens at the boundaries of two sub-divisions, the tower cluster and η cluster may fall into two different η sub-divisions and they will not be matched. The mismatch will cause the efficiency to be compromised.

We have developed an independent BEMC reconstruction package to deal with these drawbacks.

3.2.2.2 The UCLA BEMC Reconstruction Software

We have developed the *StEmcPointMaker* package which serves the same function as *StPreEclMaker* combined with *StEpcMaker* in the STAR library. We have made several improvements. To name a few: it has a floating clustering threshold for the BSMD; it does clustering conditionally to save CPU time; it does clustering across sub-divisions on ϕ plane; it has a dynamic window for cluster-matching, so there is no loss of efficiency due to mismatch; and it has detailed quality assurance histograms for every step. Figure 3.14 is the flow chart of the

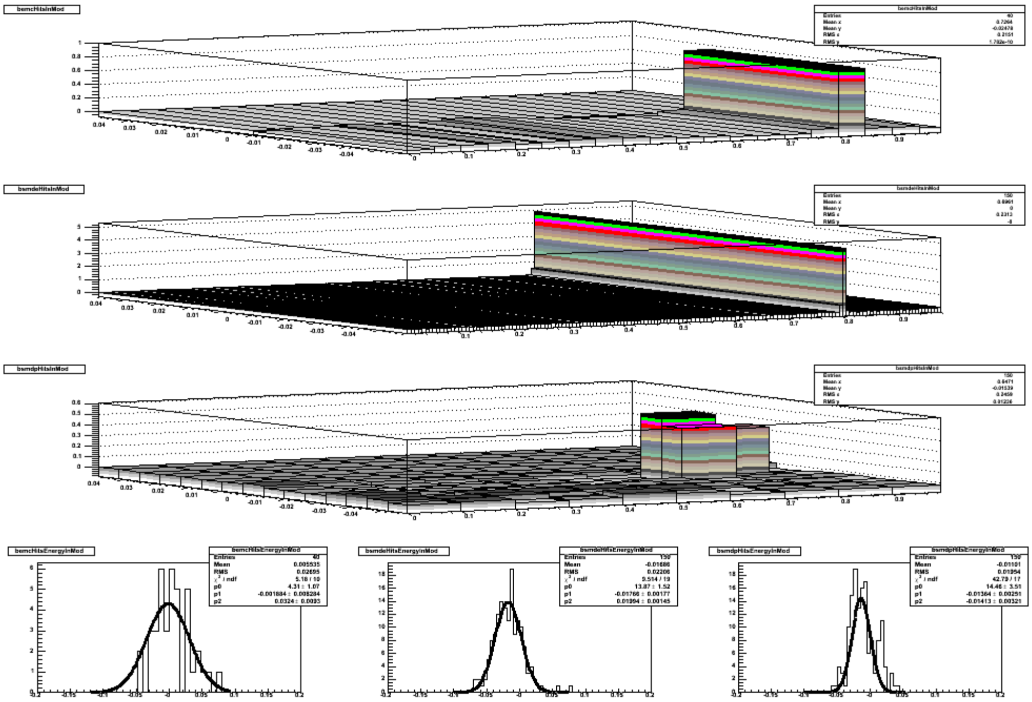

Figure 3.13: A situation when ϕ cluster crosses two sub-divisions. The 2-D histogram on the third row shows a ϕ cluster composed of two strips in one sub-division and one strip in a neighboring sub-divison.

UCLA BEMC reconstruction software.

Here are some explanation of the steps in the above figure:

Towers OK: basic check if the module has valid towers for current event. It's not yet implemented. It may not even be implemented in the future, given that the detector is working satisfactorily.

η/ϕ ***Strips OK***: basic check if the module has valid BSMD strips for current event. This is quite important because the clustering thresholds are determined by the energy spectrum of 150 BSMD strips in the module. The clustering thresholds can be also set to be some default fixed values for every module, every event. This can be set in the runtime macro.

Mask Towers: Please refer to the explanation of ***Mask*** η/ϕ ***Strips***.

Cluster Towers: put together the towers having energy above the threshold. Please note that there is no limit on the number of towers in a tower cluster.

Analyze & Check $\eta(\phi)$ ***Strips***: get all the strips in the module and fill their energies into a histogram to get the energy spectrum. In an event where the BSMD module occupancy is low, most of the strips are quiet and give out energies close to zero. A gaussian fit will produce a *mean* and *sigma*. The *mean* and *sigma* information will be used to determine the clustering thresholds later. Figure 3.15 shows the clustering threshold($Threshold_{seed} = mean + 3 * sigma$) distribution for BSMD η and BSMD ϕ modules. The second smaller peak of the BSMD ϕ module clustering threshold distribution(the right plot in Figure 3.15) is caused by one abnormal module(module 56), which has a very small *sigma* in general. This can be seen in Figure 3.16 and Figure 3.17. This scheme works but costs a lot of CPU time. In practice, a fixed default threshold can be also used for clustering and this step can be skipped.

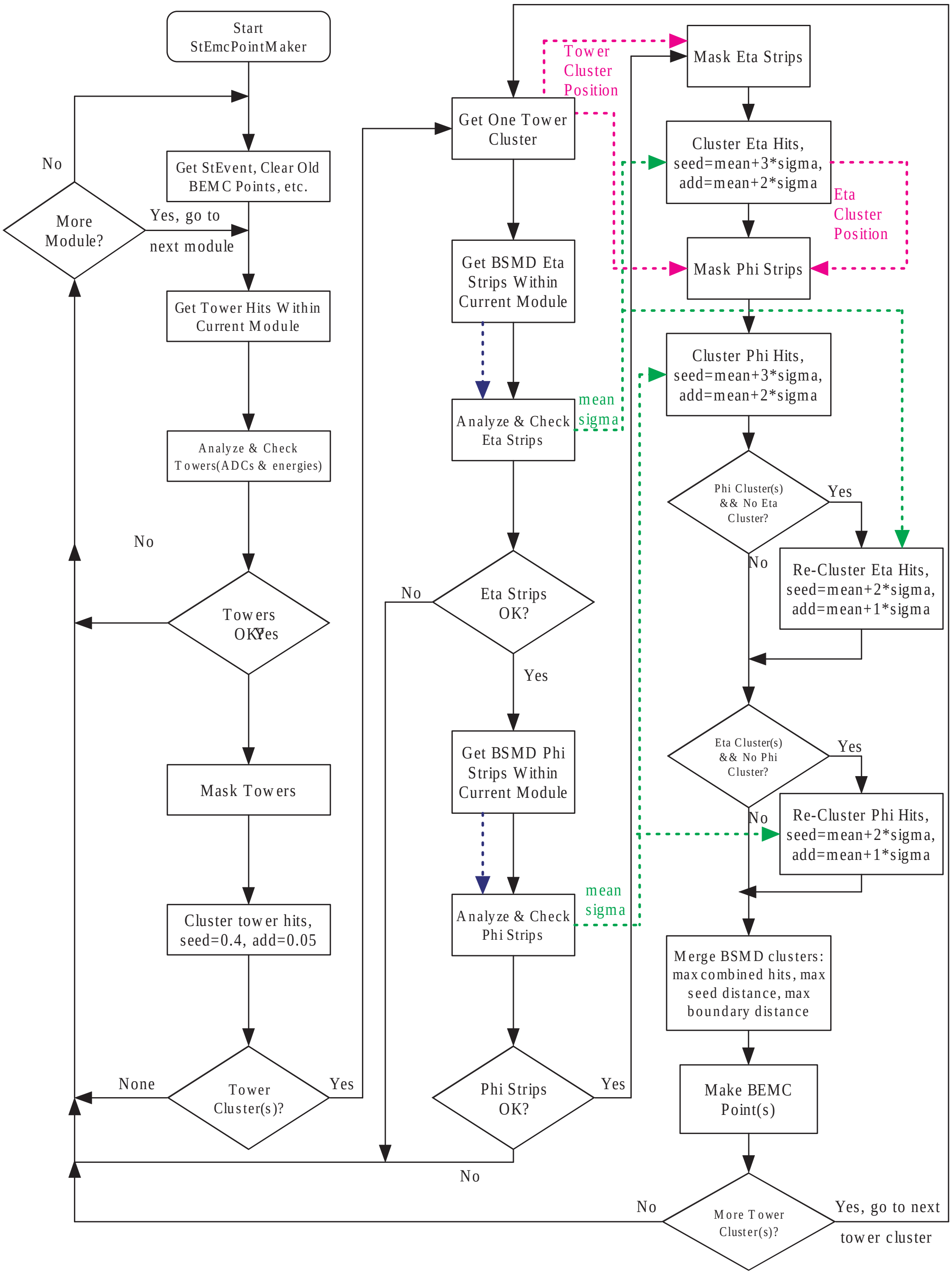

Figure 3.14: The flow chart of the UCLA BEMC reconstruction software: *StEmcPointMaker*.

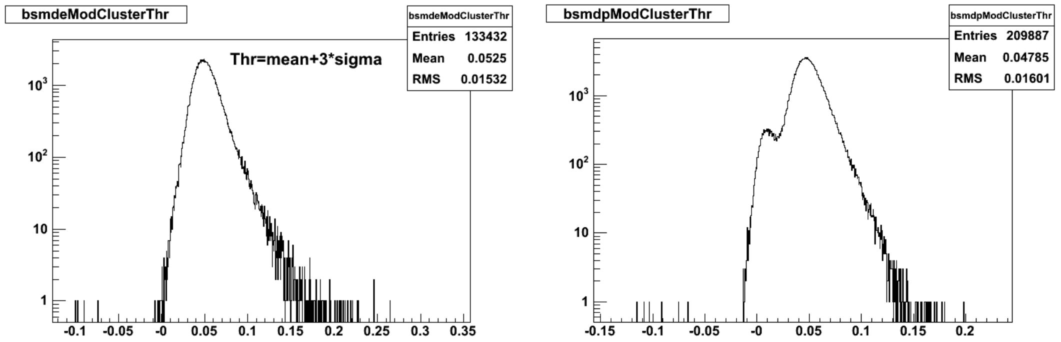

Figure 3.15: BSMD η(Left) and ϕ(Right) module clustering threshold distributions. The clustering thresholds are determined from the mean and sigma of the 150 detecting channels of each BSMD module. While every BSMD η module seems to be normal, there is at least one abnormal BSMD ϕ module. The 150 detecting channels of the abnormal BSMD ϕ module has a lower average pedestal than that of the channels in the other normal modules.

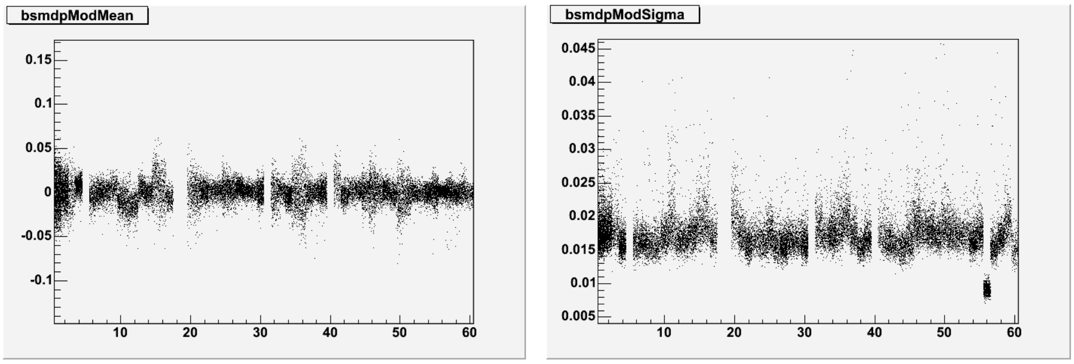

Figure 3.16: The mean and sigma of the 150 detecting channels in each BSMD ϕ module. The 150 detecting channels of module 56 have a lower average pedestal than that of the channels in the other modules. And also the sigma of the 150 detecting channels' pedestals differs largely from module to module.

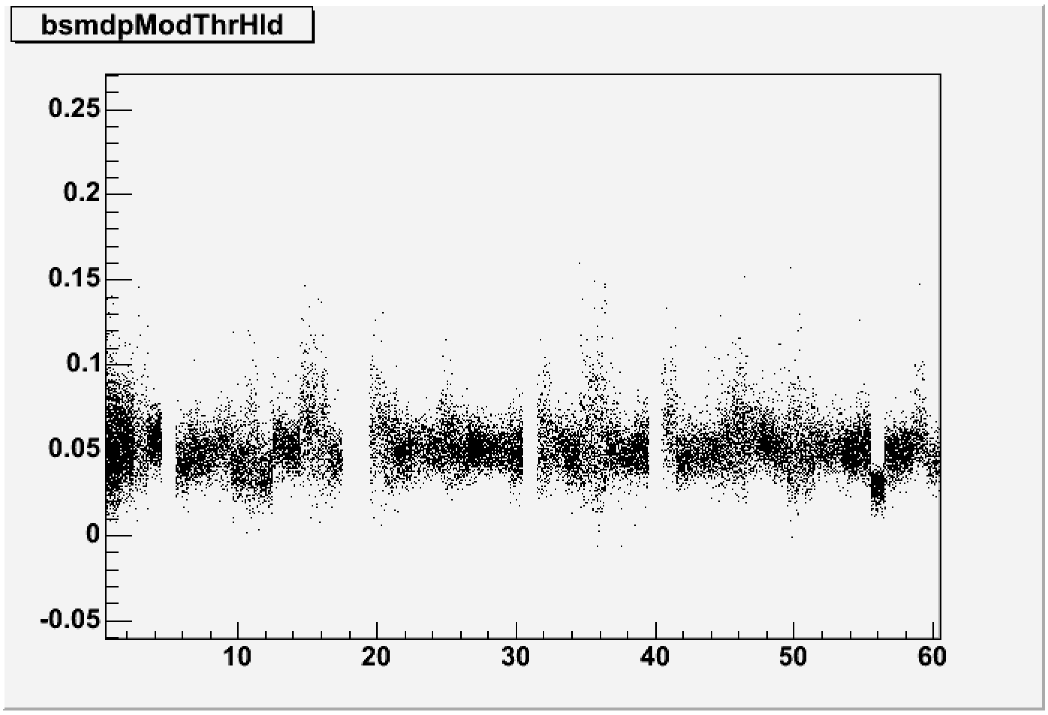

Figure 3.17: The BSMD ϕ clustering threshold of each module. The clustering thresholds are determined from the mean and sigma of the 150 detecting channels of each BSMD ϕ module. A fixed uniform threshold is not a good choice for clustering BSMD strips. The abnormal BSMD ϕ module No.56 is clearly identified.

Mask η Strips: according to the tower cluster's position and η expansion range, only the η strips that are within that η range will be considered for later BSMD η clustering. The other strips' energies will temporarily be zeroed.

Mask ϕ Strips: η cluster's ϕ range or tower cluster's ϕ range will be used to mask the ϕ strips. Only ϕ strips within that ϕ range will be considered for later BSMD ϕ clustering. The other strip energies will be temporarily zeroed.

Cluster $\eta(\phi)$ Hits: use seed energy threshold as $mean + 3 \times sigma$, add-on energy threshold as $mean + 2 \times sigma$. In this step, the definition of a cluster is very strict: a cluster should have NO valley in it. That means the seed strip should have the biggest energy. For other strips, the further away from the seed strip on each side, the smaller the strip's energy should be.

Merge BSMD Clusters: the strip energy fluctuation or dead strips can falsely split a single cluster into multiple clusters. Remember that in the initial clustering, the definition of the cluster is very strict. It turned out to be too strict. So it is necessary to merge BSMD clusters after the initial clustering is done. When merging two clusters, three parameters are used: maximum number of combined hits, maximum distance (in the unit of number of strips) between the two seed strips of the two clusters, and maximum distance (also in the unit of number of strips) between the two boundary strips of the two clusters. These three parameters correspond to three requirement for merging. Only if all these three requirements are satisfied, the two clusters can be recursively merged into one. By setting the maximum distance between the two boundary strips of the two clusters to 0 and the maximum distance between the two seed strips of two clusters to some large number, the strict requirement (no valley) of the cluster's shape is relieved. By setting the maximum distance between two boundary strips of two clusters to 1, the falsely split clusters caused by a dead strip could be recovered to one. During merging, a “1:2:2”(one tower cluster, two η clusters and two ϕ clusters) situation can be chosen to be favored. That means after each step of merging(suppose we have more than two clusters, then more than one step is needed to merge them because the merging is done step by step.), the program will see if the “1:2:2” situation is reached. If this “1:2:2” situation is chosen to be favored, the program will jump out of the merging loop and the merging is ended. The idea of favoring the “1:2:2” situation is to deal with high transverse momentum π^0s. The two daughter photons of a high transverse momentum π^0 will have a very small opening angle and will go into a single tower cluster. But the STAR BSMD, which has very good spacial resolution, should be able to tell them apart. While this appears like a good idea, it is not working. Detailed discussion on this follows.

Make BEMC Points: find the best match(es) between the η cluster(s) and ϕ cluster(s) based on their energies. A CERN mathlib routine is used to find the best match(es) that minimize the energy difference between the η and ϕ clusters. Eventually $min(m, n)$ BEMC points will be the output, where m and n are the numbers of the η and ϕ clusters for the given tower cluster. To determine the energies of the BEMC points for the situation when there are multiple η and ϕ clusters, the energies of the matched η and ϕ clusters can be used. The total energy of the tower cluster will be shared between the final BEMC points according to the matched η and ϕ cluster energy ratio. Because of the poor energy resolution of the BSMD, the other way to determine the tower energy sharing is to simply divide the tower cluster energy by 2 for “1:2:2” situation. Given the size of a single tower and the distance of it to the beam axis, the possibility of two uncorrelated photons(or electrons) flying into a single tower cluster is very small. So we can assume that the two BEMC points are caused by the decay daughters of a high transverse momentum π^0 and their energies should be very close. To compare the effects of using different merging parameters and energy sharing choices, all reasonable combinations of the merging parameters (in ***Merge BSMD Clusters***) and energy sharing choices (in ***Make BEMC Points***) were used and the histograms of the invariant mass of two BEMC points were plotted. From these invariant mass plots, we found that most of the time the "1:2:2" situation is not caused by two decay daughters of a π^0. Because of the 1 GeV cut for a single photon when the invariant mass was calculated, for the way of dividing tower cluster energy by 2, both photons will pass the cut if the tower cluster energy is above 2 GeV. This is fairly likely to happen, so there is a peak on the left side of the π^0 peak. While if dividing the tower cluster energy by the BSMD energy ratio, because of the big fluctuation of the BSMD energy ratios, it's very hard for both of the split points to survive the 1 GeV cut. Thus the false peak is not seen. Figure 3.18 shows the comparison of these two methods. The only difference between these two lies in that the left one uses *divide energy by 2* method, where the right one doesn't.

For some of the key steps there are quality assurance histograms to make sure the program behaves as it is supposed to. For example, Figure 3.19 are the histograms showing the number of η/ϕ strips below a tower cluster. Figure 3.20 shows the $\eta - \phi$ distribution of the reconstructed BEMC points.

By varying the clustering parameters, the best combination of parameters is found. The criteria is the π^0 peak signal to combinatorial background ratio. The best group of parameters are found to be 6 for the maximum number of combined hits, 4 for the maximum distance between two seed strips of two clusters, and 0 for the maximum distance between two boundary strips of two clusters. Figure 3.21 shows the invariant mass spectrum using the best combination of parameters. A π^0 peak is clearly seen in this plot.

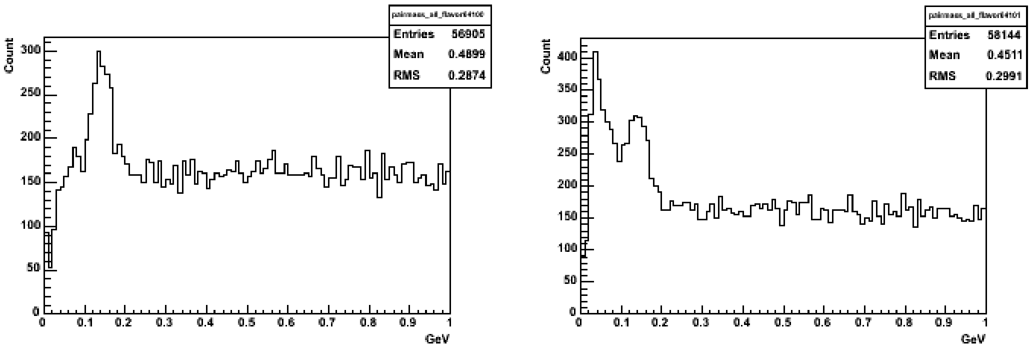

Figure 3.18: The comparison of using two different energy sharing choices. The left one does not use *divide energy by 2* method, the right one uses *divide energy by 2* method. During the *Merge BSMD Clusters* step, both of them use maximum number of combined hits as 6, maximum distance between two seed strips of two clusters as 4, maximum distance between two boundary strips of two clusters as 1.

We found that by using the similar clustering threshold parameters (that means the fixed uniform clustering threshold parameters are used instead of the calculated clustering threshold parameters), the UCLA BEMC reconstruction software can find 23% more electrons than the STAR library software! Had the calculated clustering threshold parameters been used, one would expect an even bigger improvement. However, it is found that the pedestal fitting of ***Analyze & Check*** $\eta(\phi)$ ***Strips*** step uses a lot of CPU time, so this step is skipped and the uniform clustering threshold parameters are used in this dissertation analysis. One possible future improvement is to have fixed but non-uniform clustering threshold parameters. This will solve the problem resulted from the non-uniform mean and sigma of the 150 detecting channels' pedestals of the modules, but without the huge cost of CPU time.

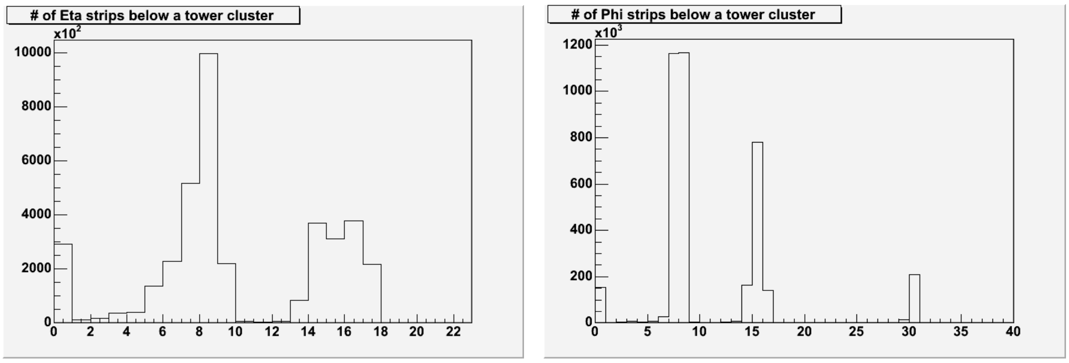

Figure 3.19: Number of working η/ϕ strips below a tower cluster. Geometrically, there should be $7\frac{1}{2}$ BSMD ϕ strips and 7 to 10 BSMD η strips below one tower. Then below a tower cluster, the number of BSMD ϕ strips is the multiple of $7\frac{1}{2}$ and the number of BSMD η strips is the multiple of any number between 7 and 10. The fact that some strips are not working complicates the situation. For example, in the left plot, some tower cluster can have number of BSMD η strips less than 6.

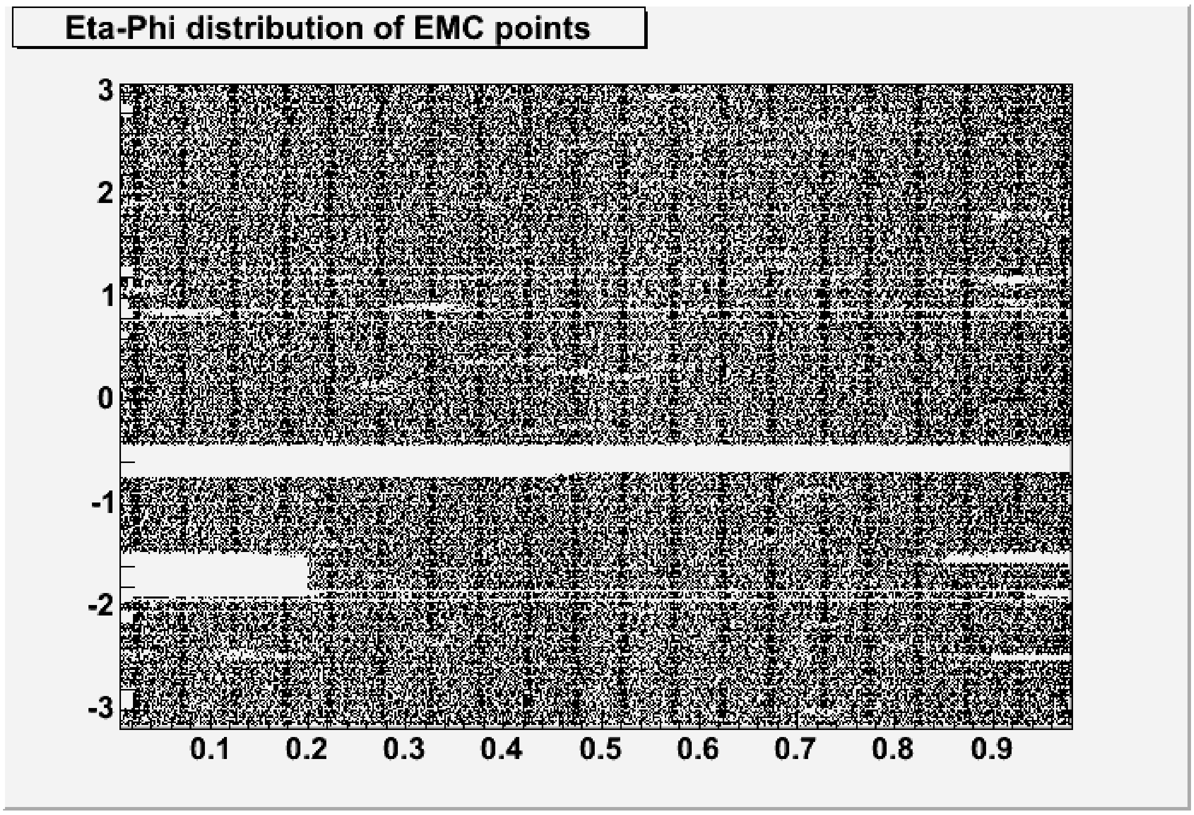

Figure 3.20: $\eta-\phi$ distribution of the reconstructed BEMC points. Except for one missing module and a few missing towers, the detector and the program behave normally. The darker vertical lines are tower centers. This happens if there is no BSMD η and BSMD ϕ cluster below the tower cluster, so the BEMC point's η and ϕ are from the tower cluster. The horizontal white lines are the gaps between BEMC modules.

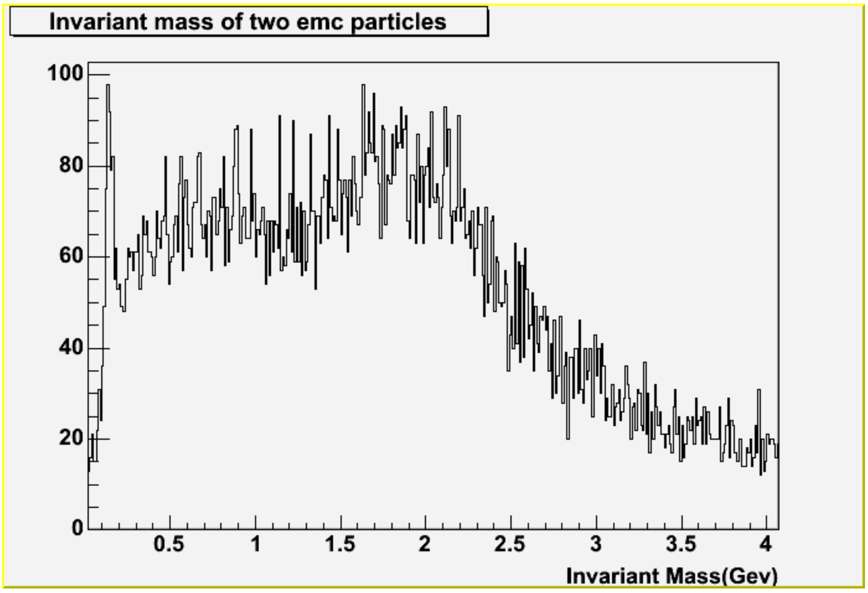

Figure 3.21: The invariant mass spectra of two BEMC reconstructed particles using different merging parameters. The π^0 peak is clearly visible around 135 MeV. If the BSMD clusters are not merged during the BEMC point reconstruction, the cluster splitting by malfunction strips will produce a small peak on the left side of the π^0 peak. The small peak will merge into the π^0 peak at higher π^0 p_T bin.

3.2.3 Hadron Rejection and Electron Selection

To reject hadrons and select electrons from heavy ion collisions at STAR, all the TPC reconstructed charged tracks within the interesting dynamic range are projected onto the BEMC tower inner plane, the BSMD η plane and the BSMD ϕ plane respectively. Tracks are projected onto the three planes of 60 modules and there is **NO** simplification of 60-side polygon cylinder to a circular cylinder. A virtual projection point will be the result of the combined information from all the three separate projections, with η or z from the projection onto BSMD η plane and ϕ from the projection onto BSMD ϕ plane. Any reconstructed BEMC point having a tower (a BEMC point has a tower cluster, and a tower cluster has towers) that geometrically contains the projection point to the tower inner plane will be associated with the track. Multiple BEMC points can be associated with one TPC track because two reconstructed BEMC points can share a tower hit. Multiple TPC tracks can also go into one tower. To study the v_2, the isolation cuts (a "one TPC track to one BEMC point" association requirement) can cause bias, so they are not used. Only the tracks with at least one BEMC point association will be further considered as electrons. The further consideration includes:

P/E: Track's momentum P is measured by TPC, and the associated BEMC points' total energy E is measured by BEMC. "Total" means if multiple BEMC points are associated with one track, then the sum of the energies from these BEMC points will be used as the E: the denominator. If projecting properly, an electron will deposit almost all of its energy in the BEMC towers because the towers have 21 radiation lengths. So the ratio of P to E should be around 1 for electrons. However, this is not true for hadrons. By setting the cut on P/E to be $0.3 < P/E < 1.5$, we can keep most of the electrons going into BEMC while rejecting a lot of hadrons. Figure 3.22

shows the P/E for electron candidates and the P/E for all the tracks with BEMC point association.

Number of BSMD Hits: Hadrons usually do not cause electro-magnetic shower in the BEMC towers. But they do produce BSMD hits occasionally. Then number of hits produced by hadrons is usually small. Figure 3.23 shows the number of BSMD hits distribution for electrons and hadrons. The difference between them is very clear. Electron candidates must satisfy 2 <=Number of BSMD η Hits< 15 and 2 <=Number of BSMD ϕ Hits< 15.

Projection Distance: In heavy ion collisions, the high occupancy in the TPC and the BEMC causes a lot of random associations between TPC tracks and BEMC points. Since the BSMD has high spatial resolution, we can cut away a lot of these random associations by cutting on the distance between the TPC track's projection position and the reconstructed BEMC point's position. Figure 3.24 shows the two dimensional histogram of this distance. Figure 3.25 shows the one dimensional projection distance histograms in z and ϕ directions. Please note that the ϕ distance histogram has two peaks and the z distance histogram is not centered at 0. The reason is that the radius used in the software is slightly off from the reality. The cuts that we use are about 3σ on each side of the peaks.

Ionization energy loss dE/dx: After all the BEMC cuts, a final dE/dx cut is applied to the tracks. The value of the final dE/dx cut is approximately from 0 to 3σ on electron's dE/dx band when electron's transverse momentum is larger than $1.5GeV$. Above $1.5GeV$, the electron's dE/dx no longer rises. Figure 3.26 shows the dE/dx distributions of the tracks with p_T between $1.5GeV$ and $6GeV$ after BEMC and BSMD cuts.

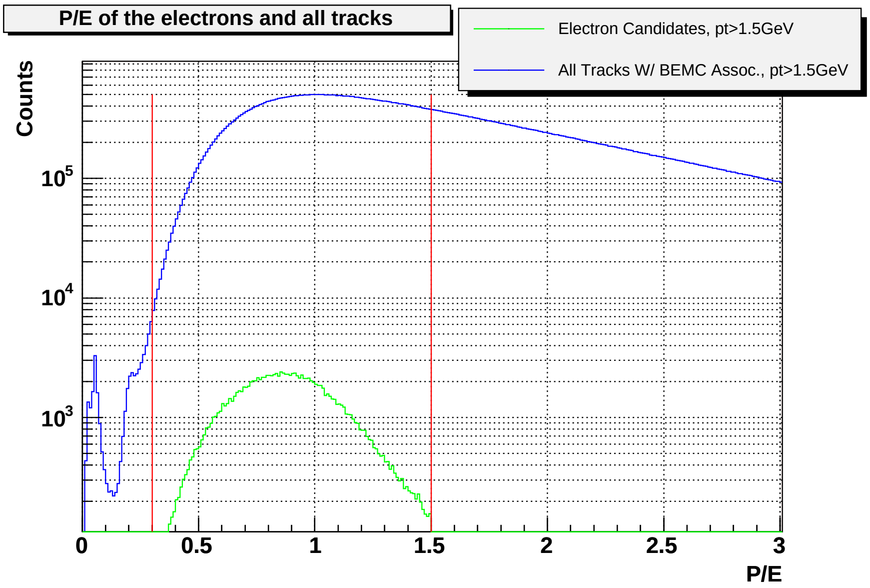

Figure 3.22: P/E for electron candidates and P/E for all tracks with BEMC association. The electron candidates are the tracks that survive all the other electron identification cuts: number of BSMD hits cut, projection distance cut, and dE/dx cut. The two small peaks between 0 and 0.3 of the P/E for all tracks are due to the energies added by photons or/and electrons going into the same tower cluster. The electron candidates P/E peak is not at 1 due to the energy contamination from the tracks going into the same tower cluster. Further analysis found that the P/E peak of electron candidates gradually moves toward 1 if the type of the event goes from central to peripheral. Electron candidates must satisfy $0.3 < P/E < 1.5$.

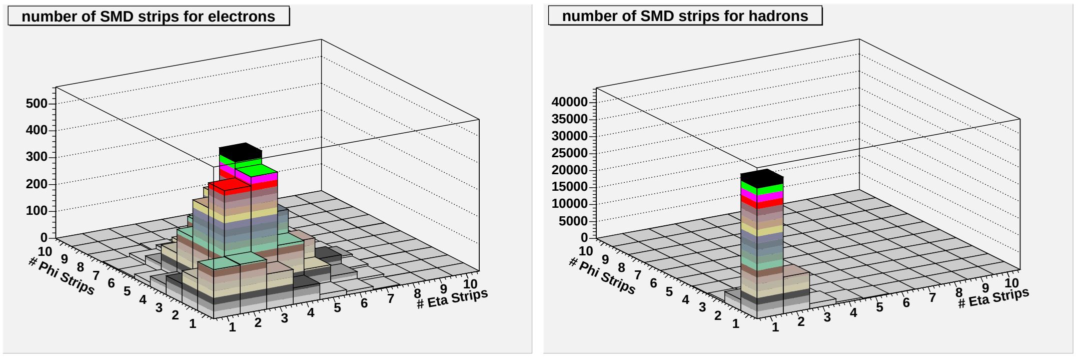

Figure 3.23: Number of BSMD hits for electrons and hadrons. The left plot is for electron candidates that already pass all other electron identification cuts except the number of BSMD hits cut. The right plot is for TPC preselected hadrons, which have dE/dx 3σ away from the electron dE/dx band. Isolation cuts are used to produce these histogram, though they are not used for v_2 analysis. Electron candidates must satisfy $2 <=$Number of BSMD η Hits< 15 and $2 <=$Number of BSMD ϕ Hits< 15.

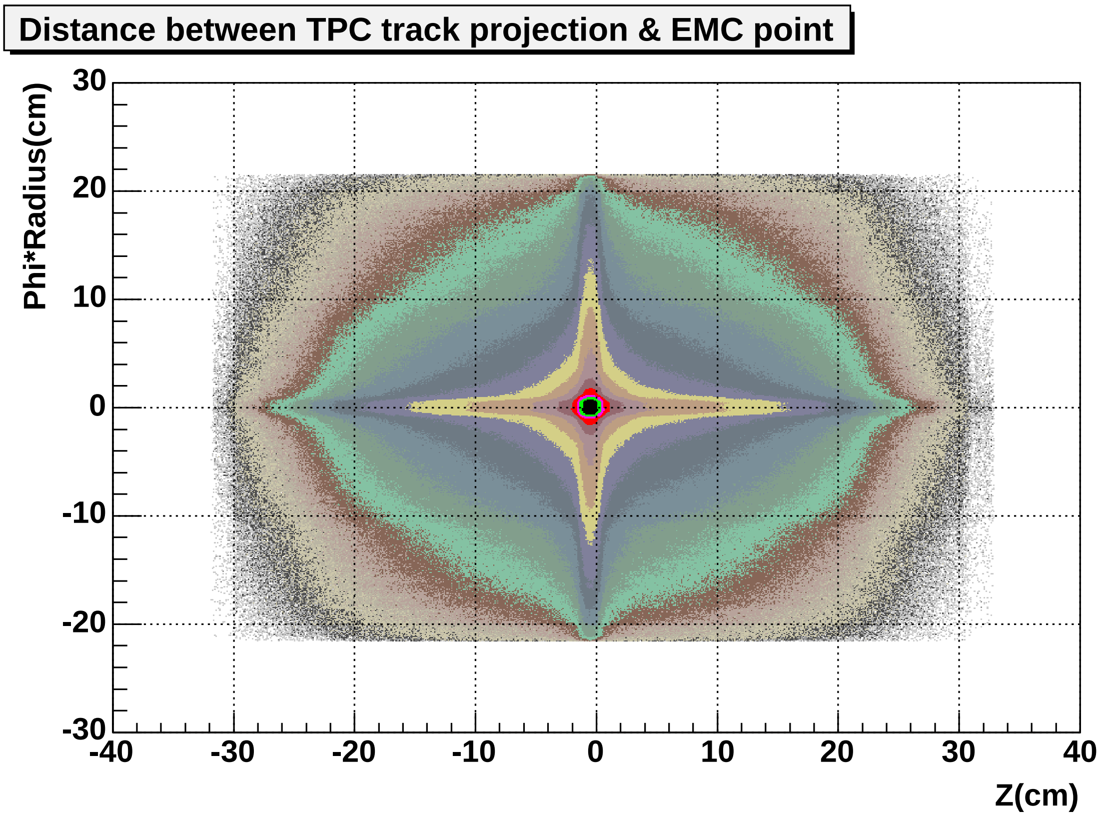

Figure 3.24: Two dimensional projection distance distribution for all tracks with BEMC point association. The “cross” is due to the situation that only one BSMD cluster is correctly assigned to the reconstructed BEMC point. During the reconstruction of BEMC points, if there is one BSMD cluster from one plane and multiple BSMD clusters from another plane, a decision has to be made on the match. If the match is wrong, then only one BSMD cluster is correctly assigned to the reconstructed BEMC point. In that case, the position of one dimension is accurate but not for the other dimension.

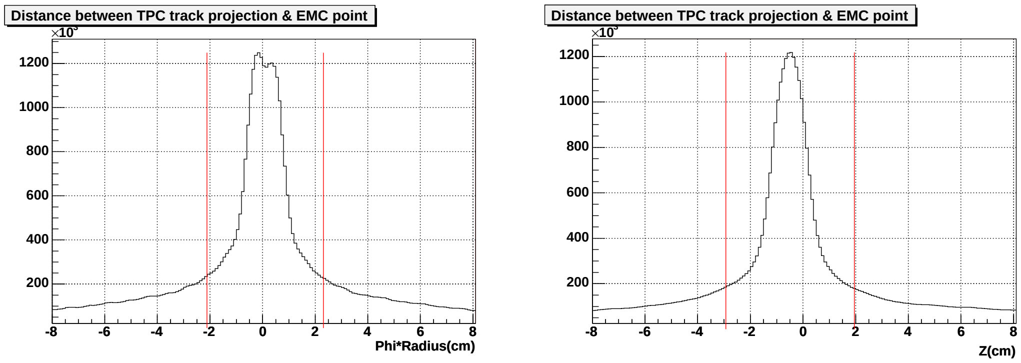

Figure 3.25: One dimensional projection distance distributions in z/η and ϕ directions for all tracks with BEMC point association. The lines denote where the cuts are set. The ϕ distance histogram has two peaks and the z distance histogram is not centered at 0. The reason is that the radius been used in the software is slightly off from the reality.

Multiple Gaussian functions are used to fit the dE/dx histogram in Figure 3.26. Two of them are used to fit the hadron dE/dx peaks and one of them is used to fit the electron dE/dx peak. From the fitting parameters and the cut parameters, the purity of the inclusive electron in this p_T bin can be calculated. The purity is defined as the number of electrons survive the electron identification cuts divided by the number of all the particles survive the same cuts.

Table 3.4 lists a summary of all the electron identification cuts.

After all these BEMC and TPC electron identification cuts, we can achieve an inclusive electron sample with a purity of nearly 100%. Figure 3.27 shows the purity of the final inclusive electron sample as a function of transverse momentum. The purity is calculated from the fitting parameters and cut parameters.

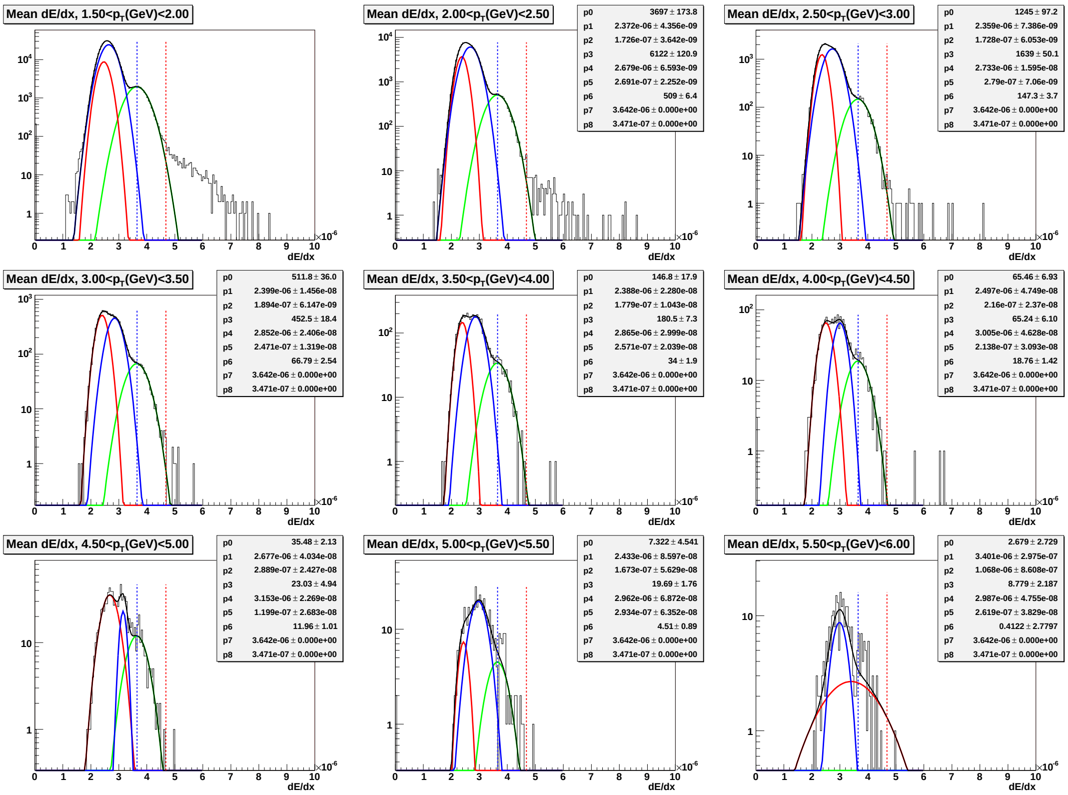

Figure 3.26: dE/dx distributions of all the tracks after BEMC cuts. In each of these plots, especially the three at the top, the ramp on the right side of the electron dE/dx peak is due to merged tracks. When two tracks are very close to each other, the TPC track reconstruction software tends to reconstruct them as one track, with dE/dx equaling the sum dE/dx of them. Three Gaussian functions are used to fit the dE/dx histograms. Two of them are used to fit the hadron dE/dx peaks and one of them is used to fit the electron dE/dx peak. The fitting failed badly for the last histogram due the limited statistics.

Table 3.4: Electron identification cuts

Parameter	Value	Comments
P/E	$(0.3, 1.5)$	An electron's P/E is about 1
Proj. Distance in ϕ ($\times$ BSMD ϕ radius)(cm)	$(2.113, 2.317)$	About $(-3\sigma, 3\sigma)$
Proj. Distance in z(cm)	$(2.929, 1.947)$	About $(-3\sigma, 3\sigma)$
No. of BSMD Hits	$(2, 15)$	An electron has big shower size
$dE/dx(\times KeV/cm)$	$(3.651, 4.681)$	About $(0, 3\sigma)$
Pseudo-rapidity η	$(-0.7, 0.7)$	To avoid large photon conversion electron background from the SVT support
Transverse Momentum p_T	$(1.5, \infty)$	To reduce hadron contamination, hadron dE/dx bands impinge electron band at low p_T
No. of Fit Points	$(20, 50)$	To ensure good track quality
No. of dE/dx Points	$(15, 100)$	To ensure good track quality
"No. Fit Points" divided by "No. Max Points"	$(0.52, 1.2)$	To avoid duplicate tracks
Chi Square	$(0, 3)$	To ensure good track quality
Global DCA	$(0, 1.5)$	To reduce photonic electron contamination

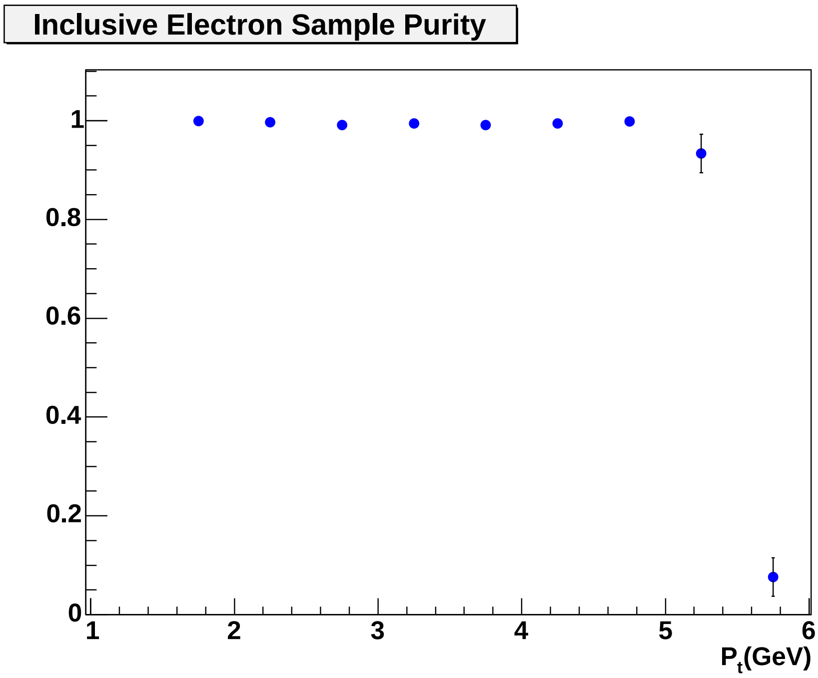

Figure 3.27: The purity of the inclusive electron sample after the BEMC cuts as a function of p_T.

3.2.4 Photonic Electron Background Removal

There are primarily two types of photonic electron background: one is from photon conversion and the other is from scalar meson Dalitz decay [Eid04]:

$$\gamma \longrightarrow e^{+} + e^{-} \tag{3.5}$$

$$\pi^{0} \longrightarrow e^{+} + e^{-} + \gamma \quad (1.198 \pm 0.032)\% \tag{3.6}$$

$$\eta \longrightarrow e^{+} + e^{-} + \gamma \quad (0.60 \pm 0.08)\% \tag{3.7}$$

There are a few sources of conversion photons: direct photons, photons from π^0 and η decays, etc. The electrons from scalar meson Dalitz decay include electrons from π^0 Dalitz decays, electrons from η Dalitz decays, etc. Among them, electrons from π^0 Dalitz decays dominate and others can be ignored [SLM03] [GW94]. The argument above leads to two types of background: electrons from photon conversion and electrons from π^0 Dalitz decays.

As all the non-photonic electrons come directly from the primary vertex of the event while the photon conversion electrons come only from the conversion points where material exists, a reasonable cut on the track's *Distance of the Closest Approach* (DCA) to the event's primary vertex should remove a lot of photon conversion electrons without hurting the statistics on non-photonic electrons. The DCA cut that is applied is $DCA < 1.5cm$. Figure 3.28 shows how the DCA cut helps to remove the photon conversion electron background.

From Figure 3.28, the DCA cut seems to remove a small fraction of photon conversion electrons. This seems to contradict the common sense. But what

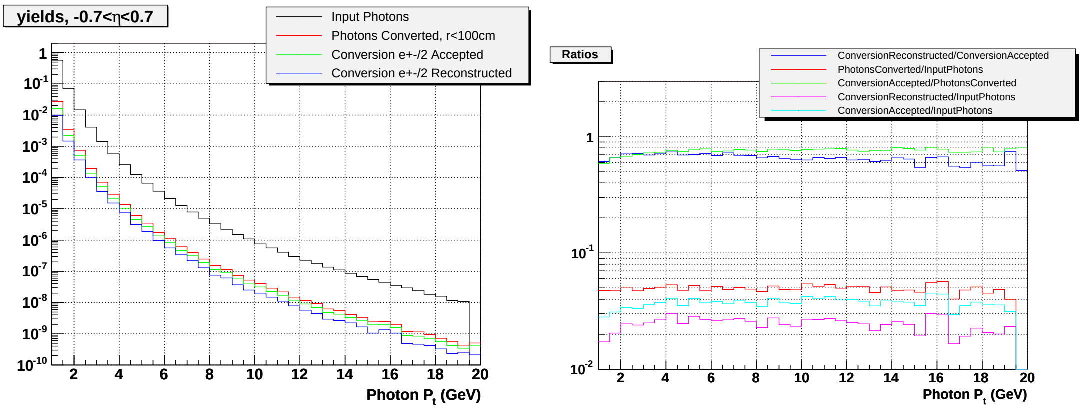

Figure 3.28: The primary vertex DCA cut's effect on photon conversion electron background removal. The left plot shows the spectra of input photons, the photons that convert inside $r < 100cm$ cylinder, the electron identification routine accepted photon conversion electrons and the invariant mass method reconstructed photon conversion electrons. The right plot shows the ratio of these spectra. The ratio of invariant mass method reconstructed photon conversion electron spectrum to the electron identification routine accepted photon conversion electron spectrum gives the photon conversion electron background removal efficiency. The ratio of converted photon spectrum to the input photon spectrum gives the probability of a photon conversion. The effect of the primary vertex DCA cut can be seen from the ratio of electron identification routine accepted photon conversion electron spectrum to the spectrum of the photons that convert inside $r < 100cm$ cylinder. This ratio is surprisingly close to 1. This seems to mean that the primary vertex DCA cut does not help much to remove photon conversion electrons.

really happens is that the tracks that not coming out of the event vertex can only be reconstructed by TPC with a much lower efficiency. So many of these photon conversion electrons are not reconstructed by the TPC in the first place. What have been reconstructed by the TPC may very likely to already satisfy the small DCA requirement. So DCA cut only removes a small fraction of photon conversion electrons been reconstructed by the TPC.

There is still a significant amount of background electrons left in the inclusive electron sample. A portion of these residual background electrons can be further identified by invariant mass calculations. If an electron comes from a photon conversion or π^0 Dalitz decay, then the invariant mass of it and its partner will be very small. However there is no such correlation for non-photonic electrons. This can be seen from Figure 3.29. When calculate the correctly identified photonic electrons via the subtraction of combinatorial histogram from the histogram showing correlation, a cut around 100 MeV can be chosen. Then the real number of photonic electrons in the inclusive electron sample can be estimated as the result of dividing the correctly identified photonic electron by the efficiency of this invariant mass method. Then the number of non-photonic electron is the number of inclusive electrons minus the number of estimated real photonic electrons.

However, as can be seen from Figure 3.29, there is a huge combinatorial “background” (this background is from our signal electrons!) underneath the invariant mass peak. In a typical Au+Au event, there are hundreds to thousands of charged tracks and many of them are used in the invariant mass calculation. So the probability that a non-photonic signal electron randomly falling into the low invariant mass region is rather high. Since the real photonic electrons are statistically calculated by the subtraction of the combinatorial histogram from the histogram showing correlation, the error propagation will make the uncertainties

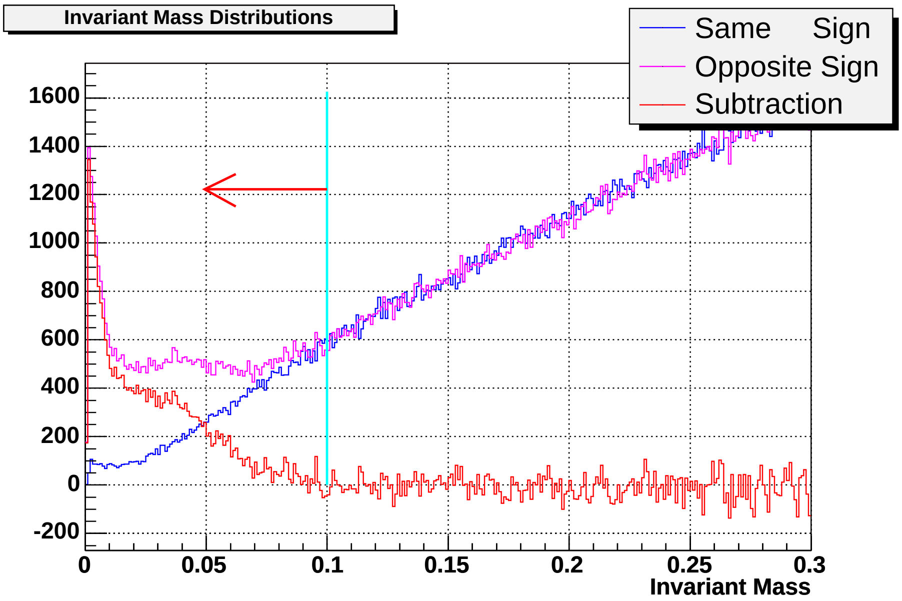

Figure 3.29: The same sign pair and opposite sign pair invariant mass distributions. The same sign pair invariant mass distribution reproduce the combinatorial background under the opposite sign pair invariant mass peak very well. In Au+Au collision, the combinatorial background is very large. If a 100 MeV cut is used to tag the photonic background electrons, the "signal" to "background" ratio is around 1. The "signal" in this context is the photonic **background** electrons, while the "background" in this context is the non-photonic **signal** electrons.

of the final result very large. Lowering the invariant mass cut will decrease the combinatorial but greatly hurt the efficiency.

Further research shows that the secondary (on the right side) invariant mass peak is caused by the limited tracking resolution. To see how this could happen, look at Figure 3.30.

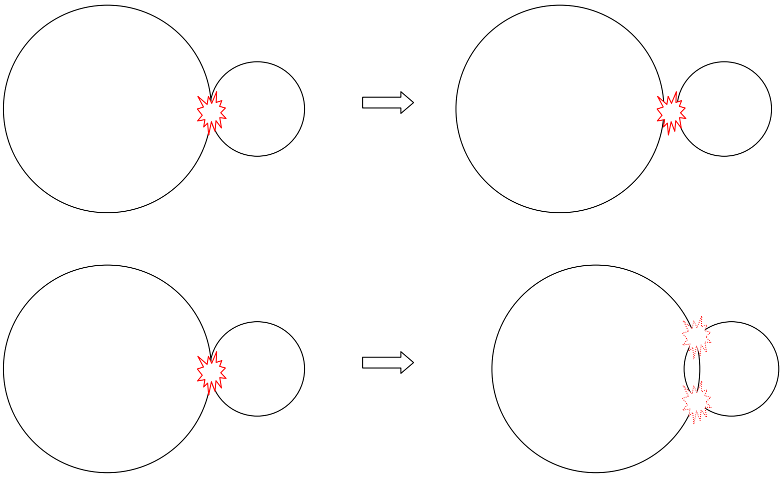

Figure 3.30: Tracking resolution effect on the invariant mass calculation. The TPC track reconstruction software reconstruct two helices either away (top) or towards each other (bottom). The view is from Z axis.

Figure 3.30 shows what two helices look like in ϕ $(X - Y)$ plane. For a pair of photon conversion electrons, two helices look like two circles almost tangent to each other in ϕ plane. The tangent point is where the conversion happens.

However, the TPC's limited tracking resolution may cause the reconstructed two circles to be shifted either away or toward each other. The procedure of calculating the invariant mass showing in Figure 3.29 is the following:

1. Identify first electron candidate from primary track[2] pool through TPC, BEMC and BSMD.
2. Find a partner candidate from the global track[3] pool, with either same or opposite charge to the first electron candidate, in the same event. The partner candidate only need to satisfy basic dE/dx cuts to maximize the partner finding efficiency.
3. Find the corresponding global track of the first primary electron, and calculate the DCA of these two global tracks.
4. Trace the momentum back to the point where the DCA of two tracks exists for each global track and calculate the pair invariant mass using the momenta found.
5. Go back to 2 until there is no more partner candidates in the event.

If the two circles are shifted away from each other, which is the situation shown in the top plot of Figure 3.30, the step 4 of the procedure above will find

---

[2] If a track has DCA to primary vertex less than $3cm$, the primary vertex (with big weight) is added to the track's original group of hits. A primary track is the fitting result of the original group of hits together with the added primary vertex. A global track is just the original track. Every primary track has a corresponding global track but not the other way. The addition of primary vertex to the track's original group of hits can greatly improve the reconstructed track's quality if and only if the track really comes from the primary vertex. A track not coming from primary vertex can be reconstructed as a primary track by chance. Then the addition of primary vertex to that track's original group of hits will cause bias towards the track's reconstruction.

[3] The partner candidate can happen to be reconstructed as a primary track but it should really be a global track.

the points where the DCA of two tracks exists to be still the tangent points. When trace two tracks' momenta back to these two points, their opening angle in ϕ plane is zero and this will result in a small invariant mass, which is the first peak on the left in Figure 3.29. If the two circles are shifted towards each other, which is the situation shown in the bottom plot of Figure 3.30, the step 4 of the procedure above will find the points where the DCA of two tracks exists to be one of the intersections shown in Figure 3.30. When trace two tracks' momenta back to these two points, their opening angle in ϕ plane is not zero and this will result in a bigger invariant mass, which is the second broader peak on the right in Figure 3.29.

This resolution effect can be eliminated by ignoring the opening angle in ϕ plane and only conserve the opening angle in θ $(X - Z)$plane [Joh02]. To do this, both momentum vectors are rotated to the same θ plane so their opening angle in ϕ plane is forced to be zero. The invariant mass resulted through this method is called 2-D invariant mass. Figure 3.31 shows the 2-D invariant mass distributions for photon conversions and π^0 Dalitz decays. Figure 3.32 shows the 2-D invariant mass distributions for same sign and opposite sign pairs for every event-plane-azimuthal-angle-adjusted ϕ bin in the real data analysis.

Table 3.5 shows a summary of the cuts been applied to remove the photonic background.

In the analysis, the photonic background electrons are removed statistically. The 2-D invariant mass between the selected electron with all the other opposite-sign charged candidates is calculated. It is tagged as *OppSign* if the 2-D invariant mass is below 100 MeV. In heavy ion collisions, even with the method dealing with combinatorial described previously, the probability that a non-photonic electron been "wrongly" tagged as *OppSign* cannot be ignored. So the num-

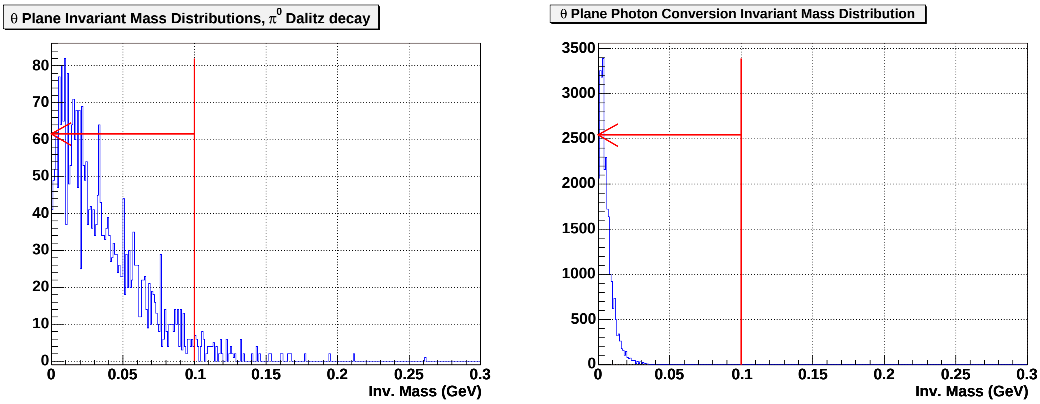

Figure 3.31: 2-D invariant mass distributions of photon conversions and π^0 Dalitz decays. The opening angle in ϕ plane is ignored in these calculations. The left plot is for π^0 Dalitz decay electrons. The right plot is for photon conversion electrons. These plots are based on the analysis of simulation data. A cut on invariant mass is chosen to be 100 MeV to contain the π^0 Dalitz decay peak.

Table 3.5: Cuts for invariant mass method for photonic background removal.

Variable	Cut
Primary Vertex DCA (cm)	$(0, 3)$
Opening Angle in θ $(radian)$	$(0, 0.02)$
Opening Angle in ϕ $(radian)$	$(0, 0.1)$
3-D Opening Angle $(radian)$	$(0, 0.1)$
2-D Invariant Mass (MeV)	$(0, 100)$
Track to Track DCA (cm)	$(0, 1)$
Partner Track's dE/dx (σ)	$(-3, 3)$

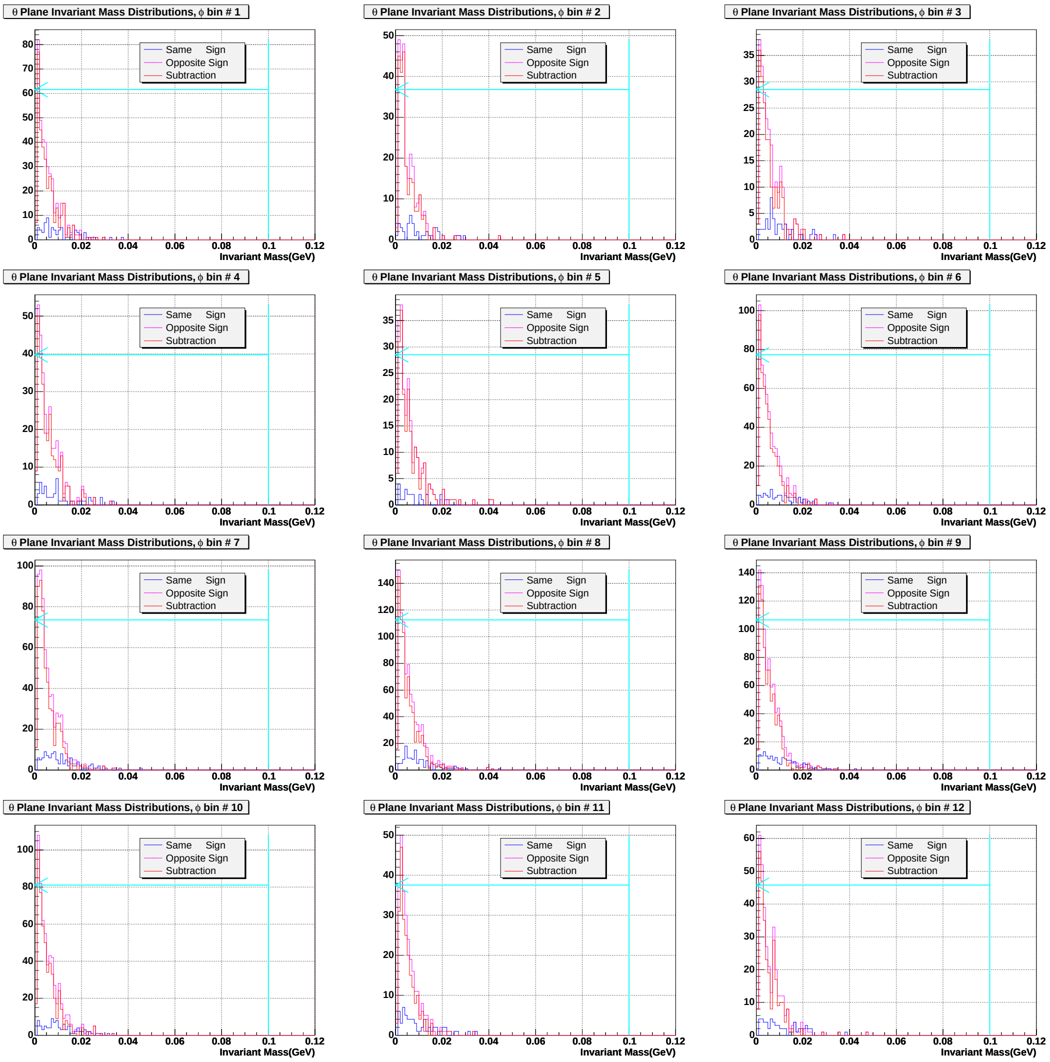

θ Plane Invariant Mass Distributions, ϕ bin # 1

θ Plane Invariant Mass Distributions, ϕ bin # 2

θ Plane Invariant Mass Distributions, ϕ bin # 3

θ Plane Invariant Mass Distributions, ϕ bin # 4

θ Plane Invariant Mass Distributions, ϕ bin # 5

θ Plane Invariant Mass Distributions, ϕ bin # 6

θ Plane Invariant Mass Distributions, ϕ bin # 7

θ Plane Invariant Mass Distributions, ϕ bin # 8

θ Plane Invariant Mass Distributions, ϕ bin # 9

θ Plane Invariant Mass Distributions, ϕ bin # 10

θ Plane Invariant Mass Distributions, ϕ bin # 11

θ Plane Invariant Mass Distributions, ϕ bin # 12

Figure 3.32: 2-D invariant mass distributions of same sign and opposite sign pairs. The opening angle in ϕ plane is ignored in these calculations. These plots are based on the analysis of real data. Although the invariant mass peak is well within 20 MeV, a cut on invariant mass is still chosen to be 100 MeV so that the π^0 Dalitz decay peak is contained, while the introduced combinatorial between 20 MeV and 100 MeV is negligible.

ber of *OppSign* electrons is always larger than the number of correctly identified photonic electrons because of the combinatorial "background" below the photon conversion peak in the invariant mass histogram shown in Figure 3.32. Now if we again calculate the invariant mass between the selected electron but with all the other *same-sign* charged partner candidates and tag them as *SameSign* if the invariant mass is also below 100 MeV, the number of *SameSign* electrons will be a good estimation of the number of "wrongly" identified photonic electrons. Then the number of correctly identified photonic electrons will be number of *OppSign* electrons minus number of *SameSign* electrons. The subtraction of *SameSign* electrons from *OppSign* electrons will not only take care of the combinatorial background, but also cancel the bias introduced by this low invariant mass cut. A low invariant mass cut is strongly correlated with a small opening angle cut, but the v_2 is about the opening angle. Thus the sample of electrons having low invariant mass with non-correlated particles tend to have biased higher v_2. The subtraction of *OppSign* electrons from *SameSign* electrons will cancel this bias.

One way to get the non-photonic electron's v_2 is to get an event-plane-angle-adjusted-ϕ distribution of the non-photonic electrons. The number of non-photonic electrons is calculated by the method described above for every bin in p_T and every bin in event-plane-angle-adjusted-ϕ. Figure 3.33 shows how this is achieved for $p_T \sim 1.75$ GeV. This process is repeated for each p_T bin. The final non-photonic electron v_2 data points can be derived from the fitting parameters. The fitting function is $Y = N(1 + 2 \times v_2^{obs} \times \cos(2 \times X))$.

For each bin in these histograms, the errors are calculated by the following way. Suppose the number of inclusive electrons is directly measured as N_{inc} and the corresponding error is $\sqrt{N_{inc}}$. The number of *OppSign* electrons is directly measured as N_{opp} and the corresponding error is $\sqrt{N_{opp}}$. The number of *SameSign*

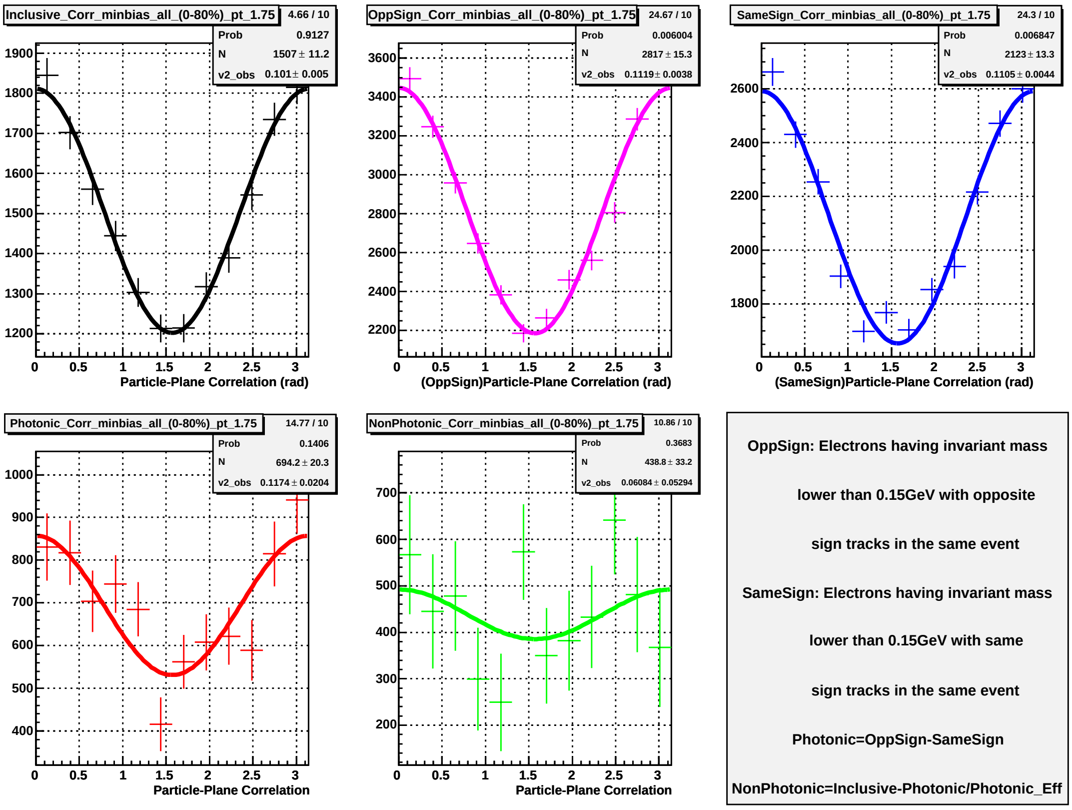

Figure 3.33: The photonic background subtraction process in non-photonic electron v_2 analysis for $1.5 < p_T(GeV) < 2$. The cuts used for the secondary track when calculating the invariant mass is around 3σ on each side of the electron's dE/dx peak. What's more, the DCA of two tracks must be less than $1cm$. When calculating the invariant mass, the track's global track version is used for the identified electron. The secondary track is also initially pulled from the global track pool. The cut on invariant mass to determine $OppSign$ and $SameSign$ is set as 100 MeV. If an electron candidate falls into the low invariant mass region multiple times, the corresponding $OppSign$ or $SameSign$ histogram will be filled multiple times. The efficiency of photonic electron identification is determined by simulation.

electrons is directly measured as N_{same} and the corresponding error is $\sqrt{N_{same}}$. Then number of photonic electrons is indirectly measured as N_{pho}, and the corresponding error is δN_{pho}(assuming no correlation between *OppSign* electrons and *SameSign* electrons), then:

$$N_{pho} = N_{opp} - N_{same} \tag{3.8}$$

$$\delta N_{pho} = \sqrt{N_{opp} + N_{same}} \tag{3.9}$$

The number of non-photonic electrons is indirectly measured and it is denoted as N_{non}. The corresponding error is denoted as δN_{non}. Assuming no correlation between inclusive electrons and indirectly measured photonic electrons, then:

$$\begin{aligned} N_{non} &= N_{inc} - \frac{N_{pho}}{\epsilon} && (3.10) \\ &= N_{inc} - \frac{N_{opp} - N_{same}}{\epsilon} && (3.11) \\ \delta N_{non} &= \sqrt{(\delta N_{inc})^2 + \frac{(\delta N_{opp})^2}{\epsilon^2} + \frac{(\delta N_{same})^2}{\epsilon^2}} && (3.12) \\ &= \sqrt{N_{inc} + \frac{N_{opp}}{\epsilon^2} + \frac{N_{same}}{\epsilon^2}} && (3.13) \end{aligned}$$

The above calculation is applied to every bin in p_T and every bin in event-plane-azimuthal-angle-adjusted-ϕ of all the non-photonic electron event-plane-azimuthal-angle-adjusted-ϕ histograms. The errors of the final non-photonic electron v_2 are from the fitting results. Figure 3.34 shows the photonic background removal process in higher p_T bins.

The other way to get the non-photonic electron's v_2 is to calculate it from the inclusive electron v_2, photonic background electron v_2 and their spectra ratios. The v_2 of non-photonic electron is a weighted average of the inclusive electron

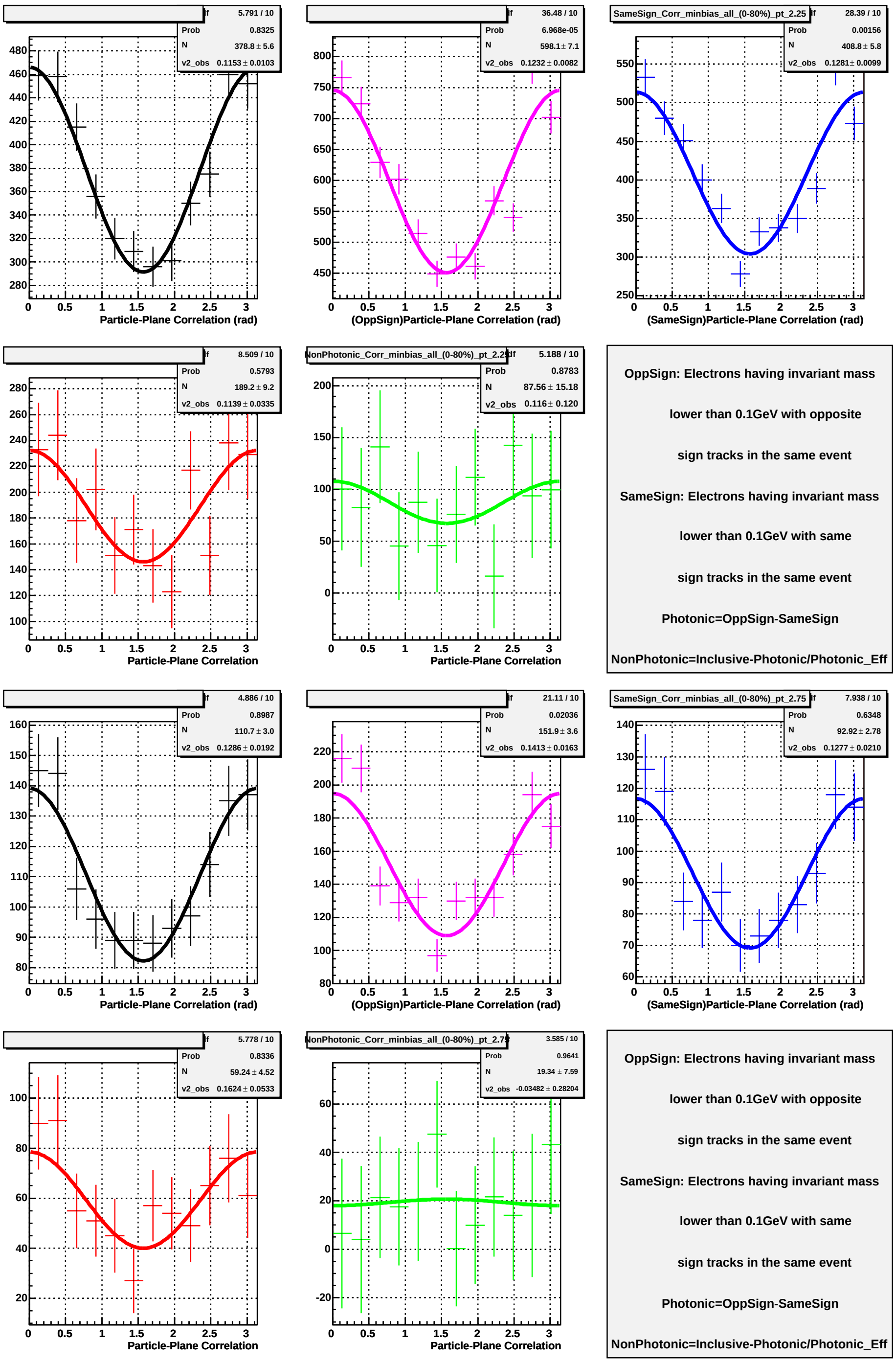

OppSign: Electrons having invariant mass lower than 0.1GeV with opposite sign tracks in the same event

SameSign: Electrons having invariant mass lower than 0.1GeV with same sign tracks in the same event

Photonic=OppSign-SameSign

NonPhotonic=Inclusive-Photonic/Photonic_Eff

OppSign: Electrons having invariant mass lower than 0.1GeV with opposite sign tracks in the same event

SameSign: Electrons having invariant mass lower than 0.1GeV with same sign tracks in the same event

Photonic=OppSign-SameSign

NonPhotonic=Inclusive-Photonic/Photonic_Eff

Figure 3.34: The photonic background subtraction process in non-photonic electron v_2 analysis for $2 < p_T(GeV) < 2.5$ and $2.5 < p_T(GeV) < 3$.

v_2 and photonic electron v_2, while the weight for photonic electron v_2 is negative and the sum of the weight is one. Both the photonic electron's $v_2({v_2}^{pho})$ and the inclusive electron's $v_2({v_2}^{inc})$ are known. And the fraction of the photonic electrons in the inclusive electron sample is also known, so the non-photonic electron's $v_2({v_2}^{non})$ can be calculated as following:

$$\begin{aligned} {v_2}^{inc} &= \frac{\frac{N_{pho}}{\epsilon}}{N_{inc}}{v_2}^{pho} + \frac{N_{non}}{N_{inc}}{v_2}^{non} && (3.14) \\ {v_2}^{non} &= \frac{N_{inc}}{N_{non}}{v_2}^{inc} - \frac{\frac{N_{pho}}{\epsilon}}{N_{non}}{v_2}^{pho} && (3.15) \end{aligned}$$

Plug in $N_{non} = N_{inc} - \frac{N_{opp}-N_{same}}{\epsilon}$ and $N_{pho} = N_{opp} - N_{same}$:

$${v_2}^{non} = \frac{N_{inc}}{N_{inc} - \frac{N_{opp}-N_{same}}{\epsilon}}{v_2}^{inc} - \frac{\frac{N_{opp}-N_{same}}{\epsilon}}{N_{inc} - \frac{N_{opp}-N_{same}}{\epsilon}}{v_2}^{pho} \quad (3.16)$$

The errors can be also calculated accordingly.

3.2.5 Photonic Electron Background Removal Efficiency

Photonic electron background removal efficiency is estimated by simulation. From section 3.2.4, there are primarily two types of photonic electron background: electrons from photon conversions and electrons from π^0 Dalitz decays. The efficiency of the removal of each is estimated separately from simulations. Then the overall photonic background removal efficiency is the weighted average of these two efficiencies.

3.2.5.1 Photon Conversion Electron Background Removal Efficiency

The photon conversion electron background removal efficiency is estimated through simulation. Photons with an initially specified p_T distribution are generated and their interaction with the detector material is simulated so that conversion electrons are produced. These simulated particles are embedded into the real event, which means the simulated response from each detector unit is added onto the real response from that detector unit in the same event. Then the embedded event is analyzed using the same method and the same cuts been used in the real data analysis [4]. The electron identification routine described in section 3.2.3 accepts a fraction of the total photon conversion electrons. Then the low 2-D invariant mass method described in section 3.2.4 reconstructs a fraction of the accepted photon conversion electrons. The ratio of the low invariant mass method reconstructed photon conversion electron spectrum to the accepted photon conversion electron spectrum gives the efficiency of removing this type of electrons as a function of p_T. For the sake of statistics at high transverse momentum,

---

[4] To use as much statistics as possible, the cuts on P/E, projection distance and number of the BSMD hits are not applied. These cuts do not affect the background removal efficiency. Since the STAR simulation code does not simulate dE/dx, dE/dx related cuts are not applied either. A TPC reconstructed track is deemed as originated from a simulated track if they have 10 common TPC hits

the initially specified p_T distribution does not resemble the real measured inclusive photon p_T spectrum. However, proper weight function $w1(p_T)$ is found so that the weighted photon p_T spectrum resembles the real inclusive photon p_T spectrum. In the weighting function $w1(p_T)$, p_T is the transverse momentum of the conversion photon. For a produced photon conversion electron, its parent photon's p_T is found and the corresponding weight is also applied towards that electron. So both the final simulated accepted and reconstructed photon conversion electron p_T spectra should resembles their real counterparts. In Figure 3.35, the left shows the raw and weighted electron spectra for both the denominator and numerator. The right of Figure 3.35 shows the efficiencies as a function of p_T.

3.2.5.2 π^0 Dalitz Decay Electron Background Removal Efficiency

The π^0 Dalitz decay electron background removal efficiency is also estimated through simulation. π^0s with an initially specified p_T distribution are generated and their Dalitz decay daughters are produced through simulation. These simulated particles are embedded into the real event, which means the simulated response from each detector unit is added onto the real response from that detector unit in the same event. Then the embedded event is analyzed using the same method and the same cuts been used in the real data analysis [5]. The electron identification routine described in section 3.2.3 accepts a fraction of the total π^0 Dalitz decay electrons. Then the low 2-D invariant mass method described in section 3.2.4 reconstructs a fraction of the accepted π^0 Dalitz decay electrons.

---

[5] To use as much statistics as possible, the cuts on P/E, projection distance and the number of BSMD hits are not applied. These cuts do not affect the background removal efficiency. Since the STAR simulation code does not simulate dE/dx, dE/dx related cuts are not applied either. A TPC reconstructed track is deemed as originated from a simulated track if they have 10 common TPC hits.

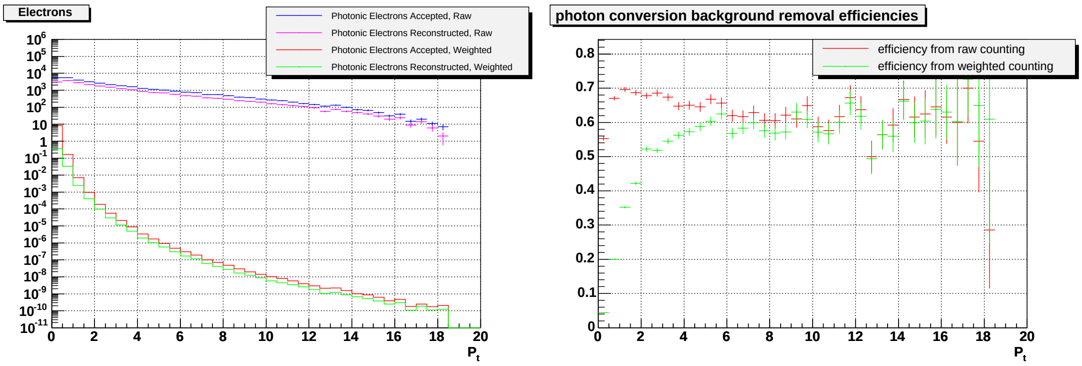

Figure 3.35: Photon conversion electron background removal efficiency calculation. The left shows the un-weighted and weighted electron spectra of both the denominator and numerator. The weight function is properly chosen so the weighted electron spectra resemble the real electron spectra from Au+Au 200 GeV minimum biased events. The right shows the efficiency as a function of p_T in each case. At low p_T, the efficiency from un-weighted calculation and the efficiency from weighted calculation deviates from each other significantly. The major reason for a photon conversion electron not having been reconstructed by the invariant mass method lies on the TPC's incapability of tracking its partner. This happens especially when its partner's p_T is too small to be tracked. So the efficiency of reconstructing a photon conversion electron strongly depends on its partner electron's p_T distribution, especially at low p_T. The un-weighted spectra does not resemble its partner electron's p_T distribution so the efficiency calculated from un-weighted spectra is not right.

The ratio of the reconstructed π^0 Dalitz decay electron spectrum to the accepted π^0 Dalitz decay electron spectrum gives the efficiency of removing this type of electrons as a function of p_T. For the sake of statistics at high transverse momentum, the initially specified p_T distribution does not resemble the real measured π^0 p_T spectrum. However, proper weight function $w2(p_T)$ is found so that the weighted π^0 p_T spectrum resembles the real π^0 p_T spectrum. In the weighting function $w2(p_T)$, p_T is the transverse momentum of the π^0. For a produced π^0 Dalitz decay electron, its parent π^0's p_T is found and the corresponding weight is also applied towards that electron. So both the final simulated accepted and reconstructed π^0 Dalitz decay electron p_T spectra should resembles their real counterparts. In Figure 3.36, the left shows the raw and weighted electron spectra for both the denominator and numerator. The right of Figure 3.36 shows the efficiencies as a function of p_T.

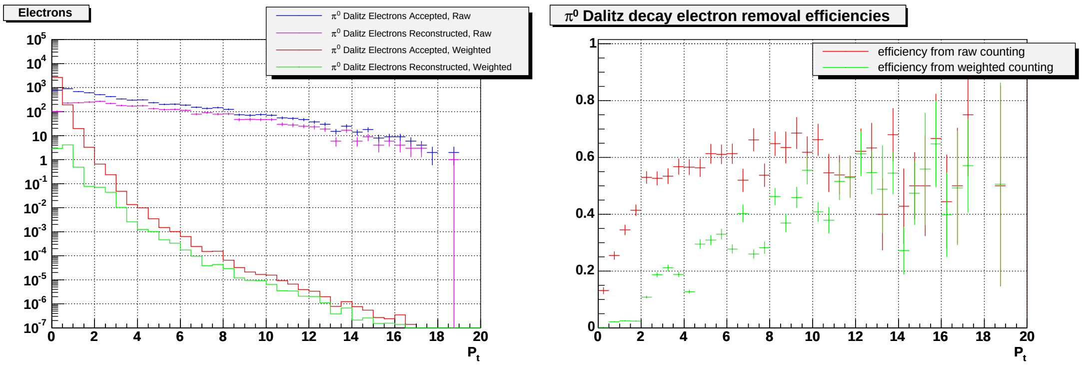

Figure 3.36: π^0 Dalitz decay electron background removal efficiency calculation. The left shows the raw and weighted electron spectra of both the denominator and numerator. The right shows the efficiency as a function of p_T. Please refer to Figure 3.35 for more explanation.

3.2.5.3 The Fraction of Two Types of Photonic Electron Background

The photon conversion electron p_T spectrum can be derived through simulation with the knowledge of inclusive photon p_T spectrum and the material in the STAR detector. The π^0 Dalitz decay electron p_T spectrum can be derived through simulation with the knowledge of π^0 p_T spectrum. The π^0 p_T spectrum and inclusive photon p_T spectrum in AuAu $200GeV$ collisions are already measured [Adl05] [Adl03].

To get the photon conversion electron p_T spectrum, photons with an initially specified p_T distribution are generated and their interaction with the detector material is simulated so that conversion electrons are produced. For the sake of statistics at high transverse momentum, the initially specified p_T distribution does not resemble the real inclusive photon p_T spectrum. However, proper weight function $w1(p_T)$ is found so that the weighted photon p_T spectrum resembles the measured inclusive photon p_T spectrum [Adl05]. In the weighting function $w1(p_T)$, p_T is the transverse momentum of the photon. For a produced photon conversion electron, its parent photon's p_T is found and the corresponding weight is applied towards that electron. So the final simulated photon conversion electron p_T spectrum should also resembles its real counterpart.

To get the π^0 Dalitz decay electron p_T spectrum, π^0s with an initially specified p_T distribution are generated and their Dalitz decay daughter electrons are produced through simulation. Again, for the sake of statistics at high transverse momentum, the initially specified p_T distribution does not resemble the real π^0 p_T spectrum. However, proper weight function $w2(p_T)$ is found so that the weighted π^0 p_T spectrum resembles the measured π^0 p_T spectrum [Adl03]. In the weighting function $w2(p_T)$, p_T is the transverse momentum of the π^0. For a produced π^0 Dalitz decay electron, its parent π^0's p_T is found and the corresponding weight is applied towards that electron. So the final π^0 Dalitz decay electron p_T spectrum should also resemble its real counterpart.

3.2.5.4 The Average of Two Types of Background Removal Efficiency

Suppose there are $N_1(p_T)$ photon conversion electrons and $N_2(p_T)$ π^0 Dalitz decay electrons. Also suppose that the efficiency to identify the photon conversion electrons is $\epsilon_1(p_T)$ and the efficiency to identify the π^0 Dalitz decay electron is $\epsilon_2(p_T)$. Then the number of background electron been identified is $N_1(p_T)\epsilon_1(p_T)+N_2(p_T)\epsilon_2(p_T)$. If the overall photonic background removal efficiency is $\epsilon(p_T)$, then the following equation should be satisfied:

$$\frac{N_1(p_T)\epsilon_1(p_T)+N_2(p_T)\epsilon_2(p_T)}{\epsilon(p_T)} = N_1(p_T)+N_2(p_T) \tag{3.17}$$

Then:

$$\begin{aligned}
\epsilon(p_T) &= \frac{N_1(p_T)\epsilon_1(p_T)+N_2(p_T)\epsilon_2(p_T)}{N_1(p_T)+N_2(p_T)} && (3.18)\\
&= \frac{N_1(p_T)}{N_1(p_T)+N_2(p_T)}\epsilon_1(p_T)+\frac{N_2(p_T)}{N_1(p_T)+N_2(p_T)}\epsilon_2(p_T) && (3.19)
\end{aligned}$$

3.2.5.5 The Simulation Quality

How accurate one can determine the efficiencies from simulation depends on how accurate the simulation agrees with the real situation. The inefficiency to remove the photonic background electrons is mainly due to the STAR TPC's tracking inefficiency, especially its inefficiency in tracking low transverse momentum particles. Because the intrinsical asymmetry distribution of a photon conversion

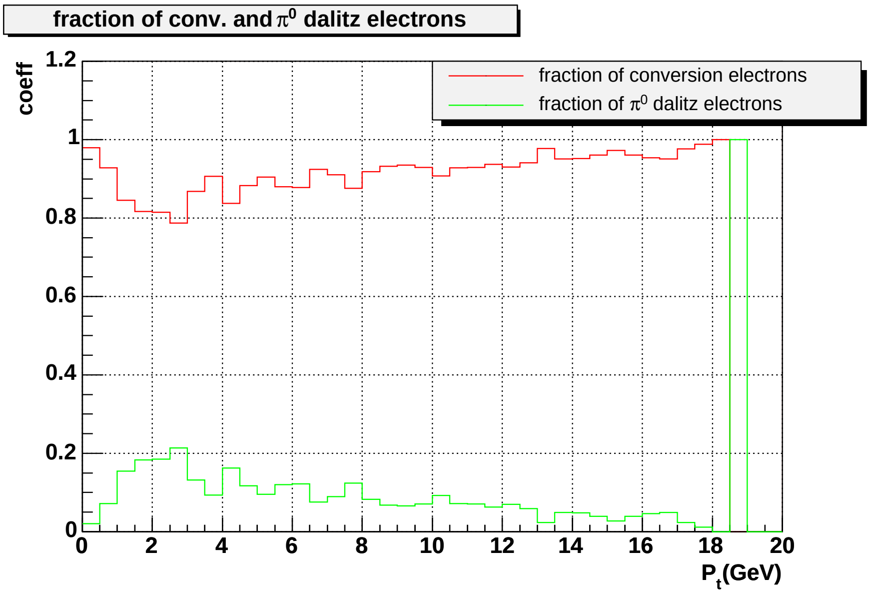

Figure 3.37: The relative fraction of two types of photonic electron background. The fraction calculation is based on published Au+Au 200 GeV minimum biased data.

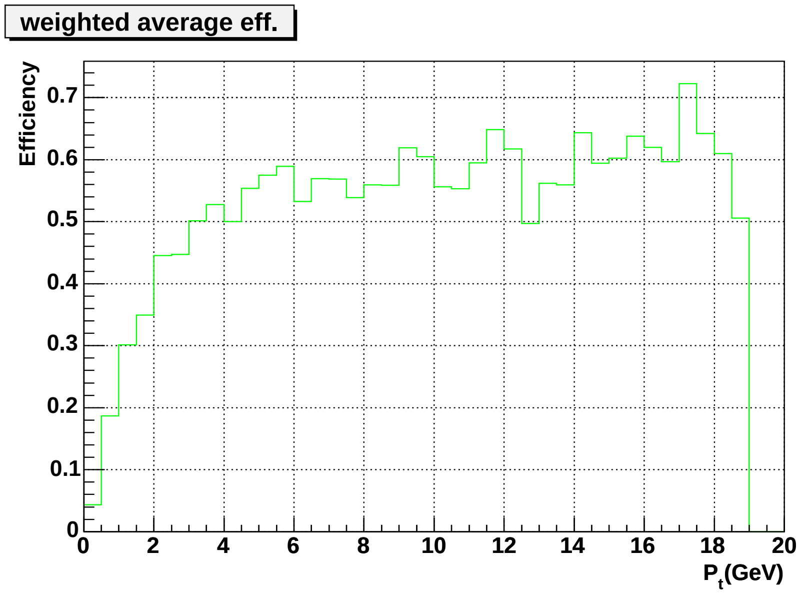

Figure 3.38: The weighted average of the π^0 Dalitz decay electron background removal efficiency and the photon conversion electron background removal efficiency. The weight function is from the calculation of the relative fraction of these two types of photonic electron background. Please refer to Figure 3.37 for the fractions.

or scaler meson Dalitz decay is rather flat, for a given identified photonic electron of p_T starting at 1.5 GeV, due to the power-law-like p_T distribution of its parent photon, the conditional probability density function of its partner track should also be close to a power law function starting from $p_T = 0$. So for a given identified photonic electron of p_T starting at 1.5 GeV, its partner electron tends to have small p_T. However, the STAR TPC has difficulty in tracking very low p_T particles. Thus the average efficiency of background electron removal is only around 50%, although the STAR TPC's tracking efficiency in middle p_T range is much higher.

To determine the background removal efficiency, it is critical to ensure that the simulation agrees with real situation very well on photonic partner electron's p_T spectrum. Figure 3.39 shows the comparison of the simulation data and real data results on photonic partner electron's p_T spectra in each firstly identified electron's p_T bin. The agreement is very good.

Another critical property in this efficiency calculation is the pair asymmetry distribution. The pair asymmetry is defined as $|(E_1 - E_2)/(E_1 + E_2)|$, where E_1 and E_2 are the energies of each particle. Figure 3.40 shows the comparison of simulation data and real data analysis results on photonic pair asymmetry distributions for each pair's p_T bin. For photons/pi^0s at a given energy, when they convert/decay into pairs of electrons, the intrinsical pair asymmetry distribution is rather flat and large pair asymmetry is not favored. The large pair asymmetry shown in these plots is due to the special sequence in the data analysis. If the first identified electron already has a high p_T, then its partner electron's p_T distribution follows a steep power law function because their parent's p_T distribution follows a steep power law function and the intrinsical pair asymmetry distribution is rather flat. For the analysis of the simulation data, the asymmetry calculation

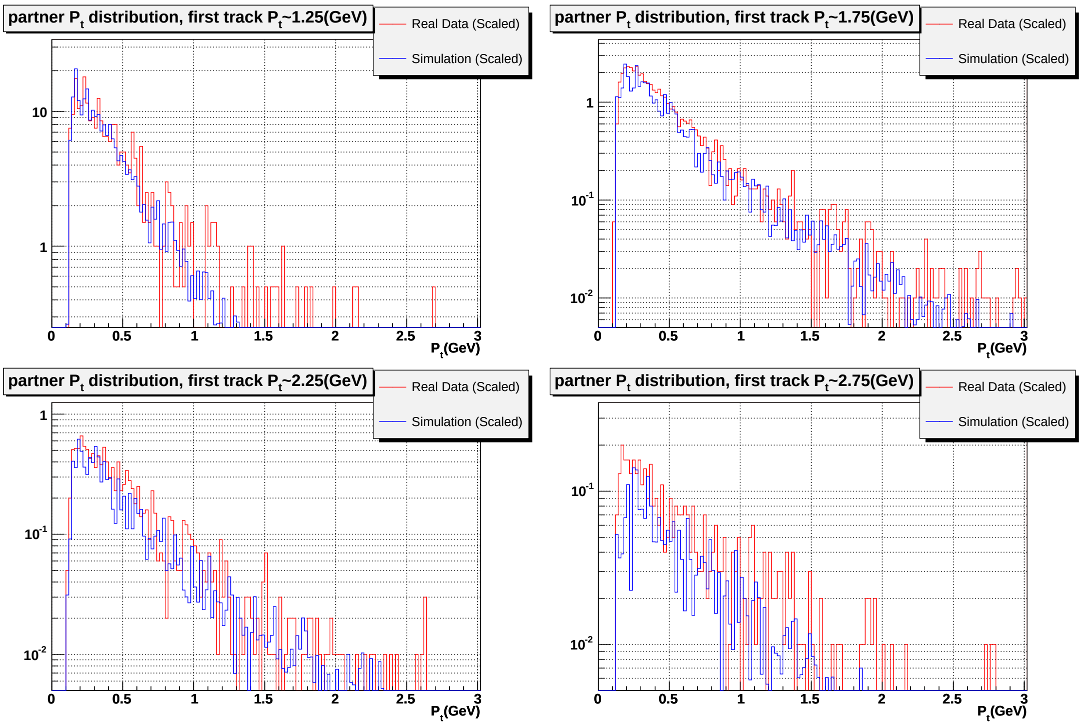

Figure 3.39: The comparison of an identified photonic electron's partner electron's p_T distributions from real data analysis and simulation data analysis. Four plots are for four p_T bins of the first identified photonic electron. Because the photonic background removal efficiency strongly depends on the partner electron's p_T distribution, it is critical to make sure that the simulation agrees with the real data very well. The *SameSign* and *OppSign* technique that is described in section 3.2.4 is used to produce the real data histograms (*OppSign*-*SameSign*) shown in these plots. Figure 3.41 shows how this technique is also applied to pair asymmetry distributions.

is easy because every track in the simulation data is known exactly. But in the analysis of the real data, the pair asymmetry calculation needs more work because no track is identified for sure. One can get the photonic pair asymmetry distribution by subtracting the same sign pair asymmetry distribution from the opposite sign pair asymmetry distribution. Figure 3.41 shows how this is done.

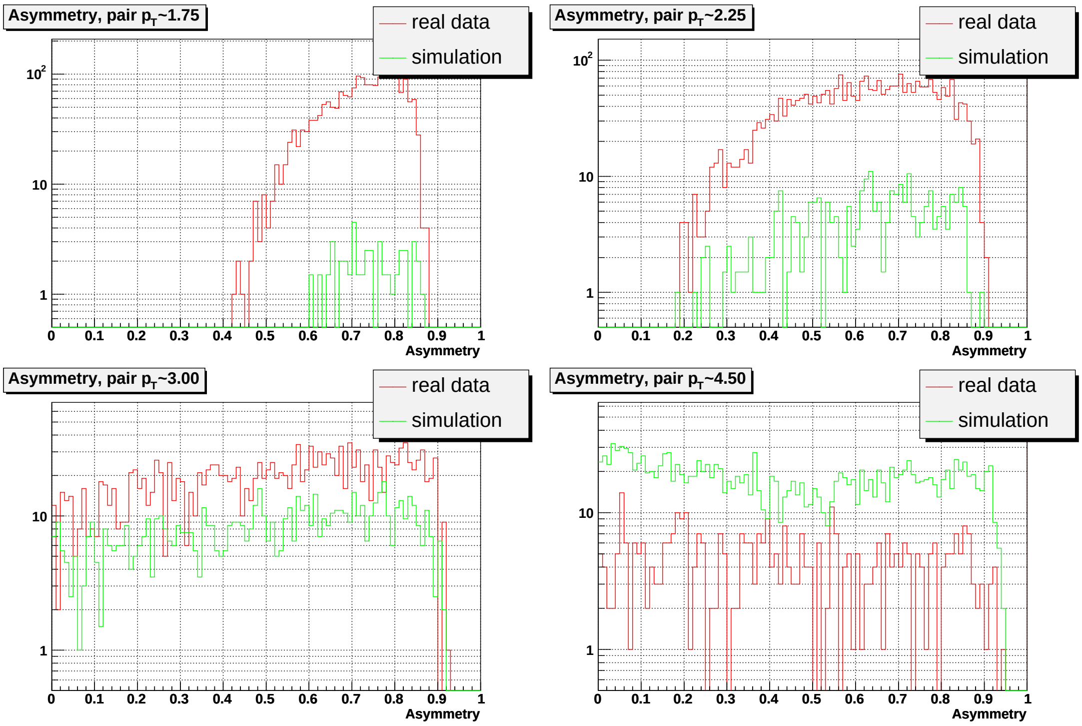

Figure 3.40: The comparison of photon conversion asymmetries from real data analysis and simulation data analysis. Four plots are for four pair p_T bins. The *SameSign* and *OppSign* technique that is described in section 3.2.4 is used to produce the real data histograms (*OppSign*-*SameSign*) shown in these plots. The large pair asymmetry is not intrinsical to photonic pairs, but due to the special sequence in the data analysis.

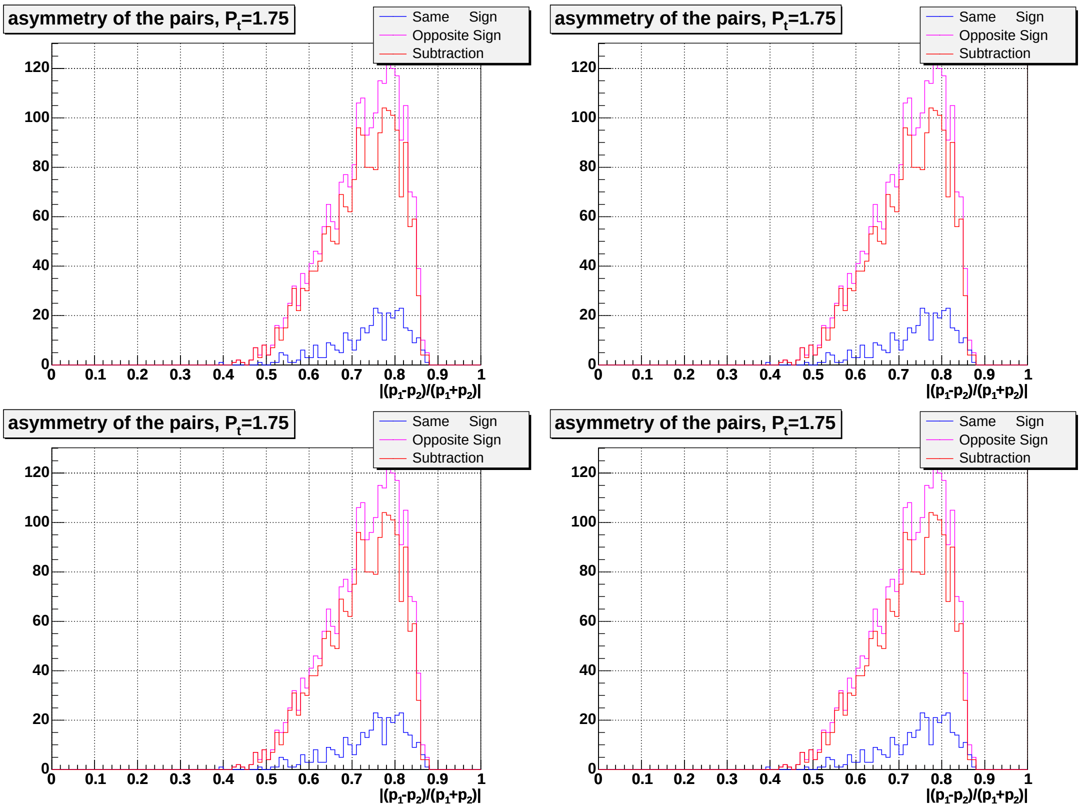

Figure 3.41: The calculation of photonic pair asymmetry distributions in the real data analysis. The photonic pair asymmetry distributions are produced by subtracting the same sign pair asymmetry distributions from the opposite sign pair asymmetry distributions.

CHAPTER 4

Results and Discussion

4.1 Results

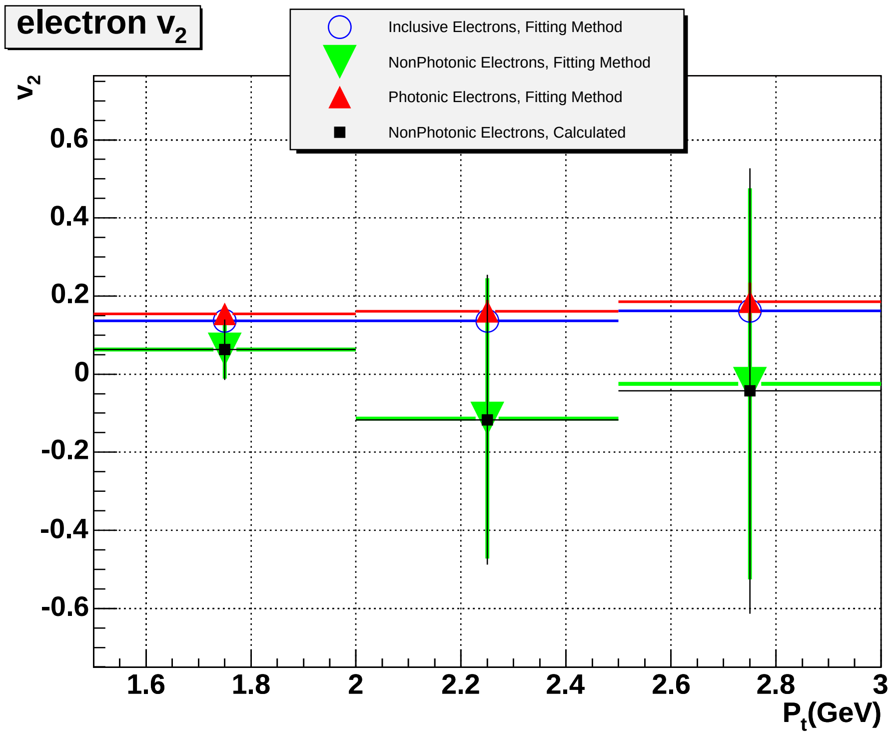

Figure 4.1: Non-photonic electron v_2 preliminary result.

Figure 4.1 shows the non-photonic electron v_2 as a function of transverse momentum for 0-80% Au+Au 200 *GeV* minimum biased events with only statistical error bars plotted. The uncertainties are so big that one cannot draw any physics conclusion on non-photonic electron elliptic flow. The two methods described in section 3.2.4 agree with each very well.

4.2 Discussion

From equation 3.16, the error in non-photonic electron v_2 comes from the error in the value of the photonic electron v_2 and from the error in the value of the inclusive electron v_2. In the STAR detector system, there is a lot of material surrounding the collision zone, for example, the material in the Silicon Vertex Tracker (SVT). The relativistic heavy ion collisions create large number of π^0's, thus large number of decay photons. The material increased the probability that these photons convert into background electron pairs. The photonic electrons coming from these photon conversions in many cases contaminated the non-photonic electron sample. Figure 4.2 shows the ratios between non-photonic, photonic and inclusive electrons. The number of photonic electrons is at least 4 times[1] as many as non-photonic electrons! Therefore the errors on the value of the inclusive electron v_2 and the photonic electron v_2 are magnified by large inclusive to non-photonic ratios and photonic to non-photonic ratios! Although the 2-D invariant mass method discussed in section 3.2.4 significantly narrowed the uncertainties on the photonic electron v_2 measurement, the final errors of non-photonic electron v_2 are still too large to make the measurement conclusive. Except for taking much more data, the only way to deal with this is to remove unnecessary material in the detector system. Removal of Silicon Vertex Tracker (SVT), which has never yielded physics results, will be very helpful and is highly recommended.

The photon can convert into an electron-positron pair wherever material ex-

---

[1] The estimation of the ratio of number of photonic electrons to the number of non-photonic electrons is very difficult.

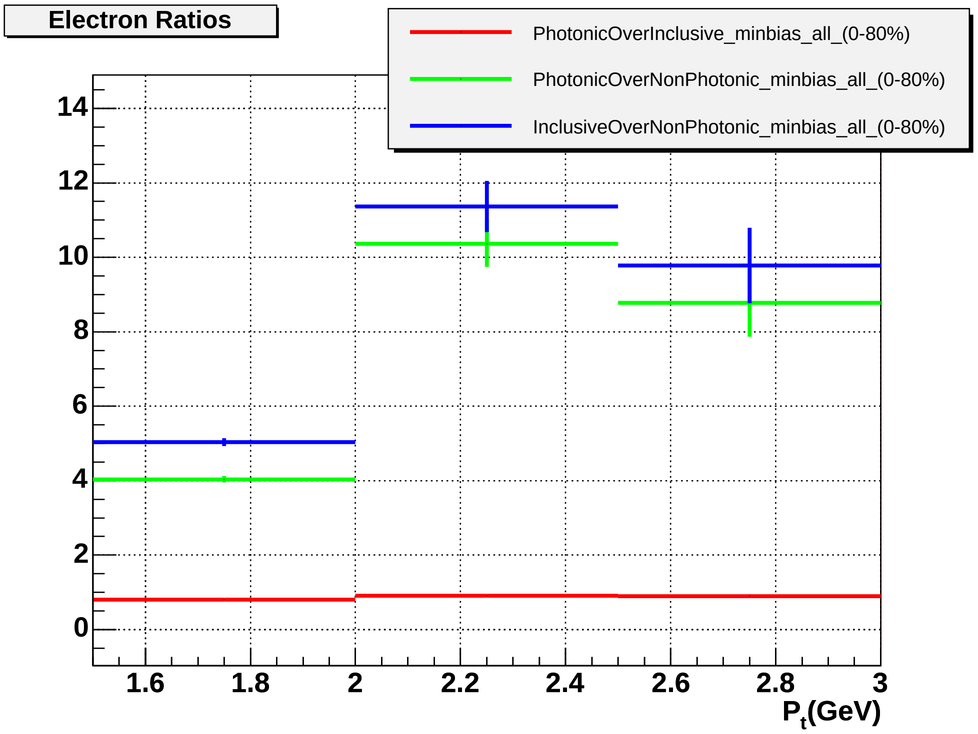

Figure 4.2: Photonic, non-photonic and inclusive electron ratios. The uncertainties from efficiency calculations are not included.

ists. In the STAR detector system, there are beam pipe, Silicon Strip Detector (SSD), SVT, Inner Field Cage (IFC), and the air molecules. Table 4.1 lists the radiation length in each of them.

Table 4.1: The radiation length of material in STAR detector

Detector/Material	Radiation Length
Beam Pipe	0.3%
SVT	4.5%
SSD	0.5%
IFC	0.6%
Air	0.15%

If the SVT is removed, the probability of photon conversion will drop by a factor of 4[2]. This will significantly improve the signal to background ratio. For example, if the signal to background ratio is 1:4 and if there are 85% background electrons come from photon conversions, then the number of photon conversion background electrons will be reduced by a factor of 4 if the SVT is removed, while the number of signal electrons and the number of π^0 Dalitz decay electrons will not change. This will lead to signal to background ratio as 1:1.45[3].

To see how the errors will be reduced if the SVT is removed, one can use 50%[4] of the original number of events to produce the inclusive electron event-plane-azimuthal-angle-adjusted-ϕ distribution, and use 36%[5] of the original number of events to produce the "opposite sign" and "same sign" electron event-plane-azimuthal-angle-adjusted-ϕ distributions and use the method from chapter 3 to get the estimation of the errors. By doing so, the signal to background ratio would

---

[2] $(0.3 + 4.5 + 0.5 + 0.6 + 0.15)/(0.3 + 0.5 + 0.6 + 0.15) \approx 4$

[3] $1 : (4 \times 0.85/4 + 4 \times 0.15)$=1:1.45

[4] $(1 + 1.45)/(1 + 4) \approx 50\%$

[5] $1.45/4 \approx 36\%$

be modified to approximately 1:1.45 for the same number of events. Figure 4.3 shows the non-photonic electron v_2 error bars for 9 million minimum biased events if the STAR SVT is removed.

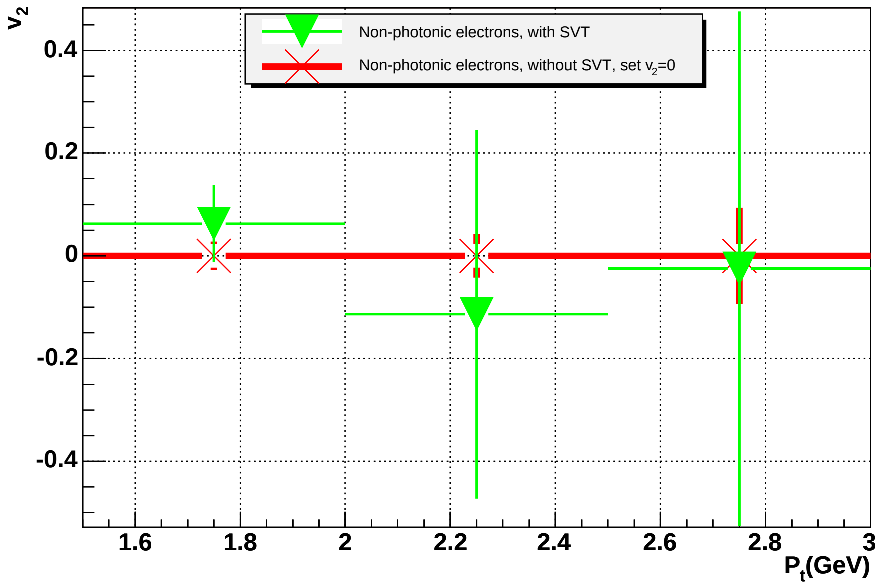

Figure 4.3: The expected non-photonic electron v_2 error bars for 9 million minimum biased events if the STAR SVT is removed. Only the error bars of each data points are relevant. Shown in the same plot is the non-photonic electron v_2 results from section 4.1

4.3 Non-photonic electron spectra measurement

The measurement of the non-photonic electron spectra is important to understand the heavy quark energy loss at high p_T[6]. As discussed in section 1.3, the large observed suppression of light hadron yield at high p_T in Au+Au central collisions compared to peripheral collisions can be explained by large parton energy loss through gluon radiation in the dense medium created by central collisions. If the gluon radiation is the dominant energy loss mechanism of partons, then the magnitude of the energy loss is sensitive to the color charge density of the medium. While the results discussed in section 1.3 are all based on the measurement of light hadrons, the measurement of heavy hadron originated non-photonic electron spectra at high p_T will provide new insight on the energy loss mechanism.

The non-photonic electron spectra can be measured by using methods similar to those discussed in chapter 3. First, an inclusive sample can be obtained by applying all the TPC, BEMC and BSMD cuts. Unlike in v_2 analysis, this inclusive sample does not need to be pure in this step. Moderate hadron contamination can be corrected for and the correction factor can be calculated from the dE/dx cuts and multiple gaussian fitting parameters of the one dimensional dE/dx distributions. Thus the number of real inclusive electrons can be calculated by correcting the hadron contamination. Secondly, the number of reconstructed photonic electrons can be calculated by subtracting the same sign pair invariant mass distribution from the opposite sign pair invariant mass distribution. Then the number of real photonic electrons in the inclusive electron sample is the number of reconstructed photonic electrons corrected by the efficiency of this invariant mass method. Finally, the number of non-photonic electrons can be calculated by subtracting the number of real photonic electrons from the number

---

[6] Research in collaboration with Alexander Suaide et al.

of inclusive electrons. Figure 4.4 shows the non-photonic electron spectra for d+Au, p+p, and Au+Au 200 *GeV* experiments. The good agreement between the pQCD calculations [CNV05] [Ada05c] and the results indicate that the electrons from B mesons start to surpass the electrons from D mesions at p_T between 4 and 5 *GeV*.

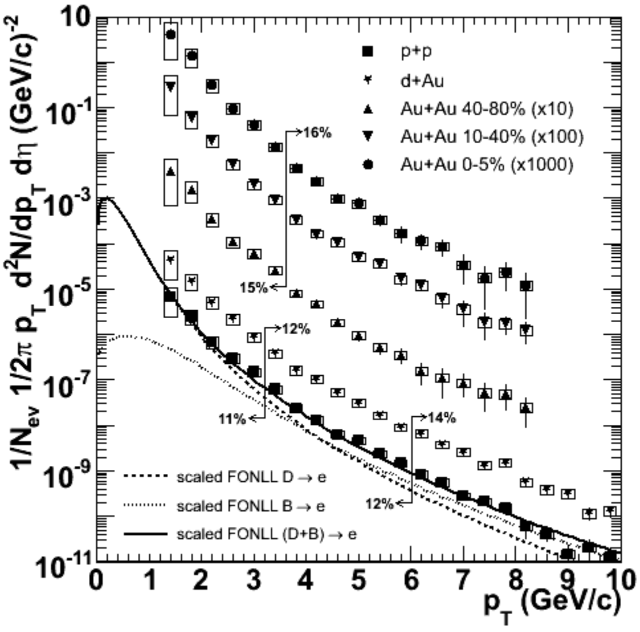

Figure 4.4: The non-photonic electron spectra for d+Au, p+p, and Au+Au 200 *GeV* experiments. The dotted line is for B meson originated electron spectra from pQCD calculation. The dashed line is for D meson originated electron spectra from pQCD calculation [CNV05] [Ada05c]. The solid lines is the sum of them. It seems that the electrons from B meson starts to dominate around p_T between 4 and 5 *GeV*.

From these spectra, we can calculate the non-photonic electron nuclear modification factor R_{AA} for d+Au and Au+Au, which are shown in Figure 4.5.

The non-photonic electron R_{AA} for d+Au is around 1 for the measured p_T range. This indicates that the non-photonic electron production, and thus the heavy quark production scales with number of binary collisions. This is consistent with the belief that the heavy quarks mainly originate from hard processes which occur at an early stage in the evolution of the system.

The large suppression of non-photonic electron yield from Au+Au central collisions is surprising. It is widely believed that due to their larger mass, heavy quarks lose less energies than light quarks through the radiation of gluons in the medium (dead cone effect) [DK01]. However, the suppression magnitude of heavy quark originated non-photonic electrons is close to the suppression magnitude for light hadrons [Ada03b]! The disagreement between the measured suppression and suppression predicted by several models indicates that there are additional energy loss mechanisms not taken into consideration by these models.

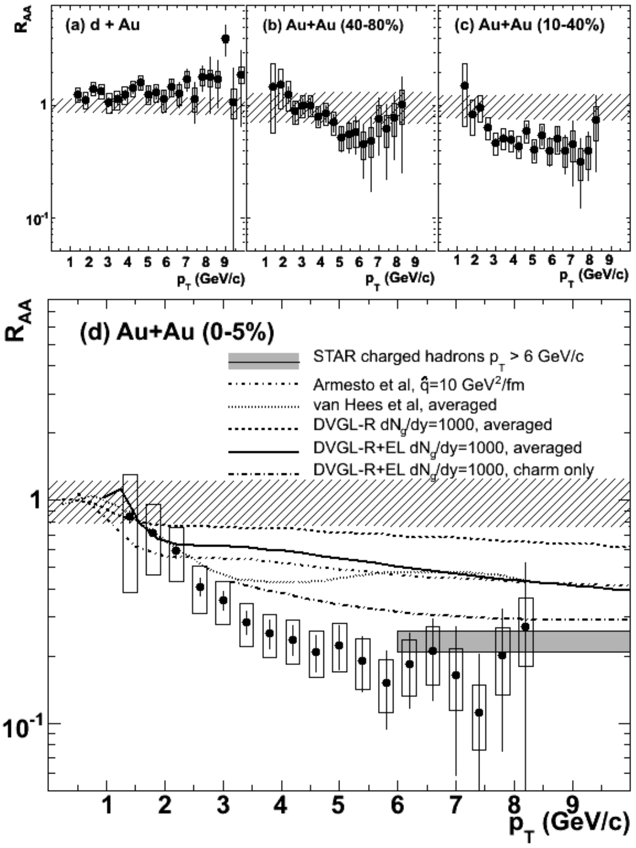

Figure 4.5: The non-photonic electron nuclear modification factor R_{AA} for d+Au and Au+Au 200 GeV experiments. The grey box around 0.2 is the average R_{AA} of measured light hadrons [Ada03b]. The dashed and dash-dotted are model predictions that took gluon radiation as the only energy loss mechanism [DGV06] [ACD05]. The dotted line is a model prediction that took elastic scattering as the only energy loss mechanism [HGR05]. The solid line is a calculation that takes both gluon radiation and elastic scattering as the energy loss mechanisms [WHD05]. All these predictions included electrons from both D and B meson decays. The authors of [WHD05] also made similar prediction with electrons from D meson decays only. It is shown as the dash-dotted line below the solid line in the legend.

APPENDIX A

Kinematics

A.1 Transverse momentum

A particle's transverse momentum is defined as:

$$p_T = \sqrt{p_x^2 + p_y^2} \tag{A.1}$$

Transverse momentum is useful because it is Lorentz invariant.

A.2 Rapidity and Pseudo-rapidity

A particle's rapidity is defined as

$$y = \frac{1}{2} \ln \left(\frac{E + p_z}{E - p_z} \right) \tag{A.2}$$

where $E{=}\sqrt{p^2 + m^2}$ is particle's energy. Like transverse momentum, rapidity is also Lorentz invariant. In experiment, the particle's identification is unknown so its mass is unknown either. Another variable called pseudo-rapidity can be quite useful. A particle's pseudo-rapidity is defined as:

$$\eta = \frac{1}{2} \ln \left(\frac{p + p_z}{p - p_z} \right) \tag{A.3}$$

In high energy experiment, it is common to have $p \gg m$, so pseudo-rapidity η is a good approximation for the rapidity y. The pseudo-rapidity can be also written as

$$\eta = -\ln\left[\tan\left(\theta/2\right)\right]. \tag{A.4}$$

where θ is the angle between the particle momentum $\boldsymbol{p}$ and the beam axis. θ can be easily measured with today's detector technology.

APPENDIX B

The STAR Collaboration

J. Adams[3], M.M. Aggarwal[29], Z. Ahammed[43], J. Amonett[20], B.D. Anderson[20], D. Arkhipkin[13], G.S. Averichev[12], S.K. Badyal[19], Y. Bai[27], J. Balewski[17], O. Barannikova[32], L.S. Barnby[3], J. Baudot[18], S. Bekele[28], V.V. Belaga[12], A. Bellingeri-Laurikainen[38], R. Bellwied[46], J. Berger[14], B.I. Bezverkhny[48], S. Bharadwaj[33], A. Bhasin[19], A.K. Bhati[29], V.S. Bhatia[29], H. Bichsel[45], J. Bielcik[48], J. Bielcikova[48], A. Billmeier[46], L.C. Bland[4], C.O. Blyth[3], S. Blyth[21], B.E. Bonner[34], M. Botje[27], A. Boucham[38], J. Bouchet[38], A.V. Brandin[25], A. Bravar[4], M. Bystersky[11], R.V. Cadman[1], X.Z. Cai[37], H. Caines[48], M. Calderón de la Barca Sánchez[17], J. Castillo[21], O. Catu[48], D. Cebra[7], Z. Chajecki[28], P. Chaloupka[11], S. Chattopadhyay[43], H.F. Chen[3]6, Y. Chen[8], J. Cheng[41], M. Cherney[1]0, A. Chikanian[48], W. Christie[4], J.P. Coffin[18], T.M. Cormier[46], M.R. Cosentino[35], J.G. Cramer[45], H.J. Crawford[6], D. Das[43], S. Das[43], M. Daugherity[40], M.M. de Moura[35], T.G. Dedovich[12], A.A. Derevschikov[31], L. Didenko[4], T. Dietel[14], S.M. Dogra[19], W.J. Dong[8], X. Dong[36], J.E. Draper[7], F. Du[48], A.K. Dubey[15], V.B. Dunin[12], J.C. Dunlop[4], M.R. Dutta Mazumdar[43], V. Eckardt[23], W.R. Edwards[21], L.G. Efimov[12], V. Emelianov[25], J. Engelage[6], G. Eppley[34], B. Erazmus[38], M. Estienne[38], P. Fachini[4], J. Faivre[18], R. Fatemi[17], J. Fedorisin[12], K. Filimonov[21], P. Filip[11], E. Finch[48], V. Fine[4], Y. Fisyak[4], K.S.F. Fornazier[35], J. Fu[41], C.A. Gagliardi[39], L. Gaillard[3], J. Gans[48], M.S. Ganti[43], F. Geurts[25], V. Ghazikhanian[8], P. Ghosh[43], J.E. Gonzalez[8], H. Gos[44], O. Grachov[46],

O. Grebenyuk[27], D. Grosnick[42], S.M. Guertin[8], Y. Guo[46], A. Gupta[19], T.D. Gutierrez[7], T.J. Hallman[4], A. Hamed[46], D. Hardtke[21], J.W. Harris[48], M. Heinz[2], T.W. Henry[39], S. Heppelmann[30], B. Hippolyte[18], A. Hirsch[32], E. Hjort[21], G.W. Hoffmann[40], M. Horner[21], H.Z. Huang[8], S.L. Huang[36], E.W. Hughes[5], T.J. Humanic[28], G. Igo[8], A. Ishihara[40], P. Jacobs[21], W.W. Jacobs[17], M Jedynak[44], H. Jiang[8], P.G. Jones[3], E.G. Judd[6], S. Kabana[2], K. Kang[41], M. Kaplan[9], D. Keane[20], A. Kechechyan[12], V.Yu. Khodyrev[12], J. Kiryluk[2]2, A. Kisiel[44], E.M. Kislov[12], J. Klay[21], S.R. Klein[21], D.D. Koetke[42], T. Kollegger[14], M. Kopytine[20], L. Kotchenda[25], K.L. Kowalik[21], M. Kramer[26], P. Kravtsov[25], V.I. Kravtsov[31], K. Krueger[1], C. Kuhn[18], A.I. Kulikov[12], A. Kumar[29], R.Kh. Kutuev[13], A.A. Kuznetsov[12], M.A.C. Lamont[48], J.M. Landgraf[4], S. Lange[14], F. Laue[4], J. Lauret[4], A. Lebedev[4], R. Lednicky[12], S. Lehocka[12], M.J. LeVine[4], C. Li[36], Q. Li[46], Y. Li[41], G. Lin[48], S.J. Lindenbaum[26], M.A. Lisa[28], F. Liu[47], H. Liu[36], J. Liu[34], L. Liu[47], Q.J. Liu[45], Z. Liu[47], T. Ljubicic[4], W.J. Llope[34], H. Long[8], R.S. Longacre[4], M. Lopez-Noriega[28], W.A. Love[4], Y. Lu[47], T. Ludlam[4], D. Lynn[4], G.L. Ma[37], J.G. Ma[8], Y.G. Ma[37], D. Magestro[28], S. Mahajan[19], D.P. Mahapatra[15], R. Majka[48], L.K. Mangotra[19], R. Manweiler[42], S. Margetis[20], C. Markert[20], L. Martin[38], J.N. Marx[21], H.S. Matis[21], Yu.A. Matulenko[31], C.J. McClain[1], T.S. McShane[10], F. Meissner[21], Yu. Melnick[31], A. Meschanin[31], M.L. Miller[22], N.G. Minaev[31], C. Mironov[20], A. Mischke[27], D.K. Mishra[15], J. Mitchell[34], B. Mohanty[43], L. Molnar[32], C.F. Moore[40], D.A. Morozov[31], M.G. Munhoz[35], B.K. Nandi[43], S.K. Nayak[19], T.K. Nayak[43], J.M. Nelson[3], P.K. Netrakanti[43], V.A. Nikitin[13], L.V. Nogach[31], S.B. Nurushev[31], G. Odyniec[21], A. Ogawa[4], V. Okorokov[25], M. Oldenburg[21], D. Olson[21], S.K. Pal[43], Y. Panebratsev[12], S.Y. Panitkin[4], A.I. Pavlinov[46], T. Pawlak[44], T. Peitzmann[27], V. Perevoztchikov[4], C. Perkins[6], W. Peryt[44], V.A Petrov[46], S.C. Phatak[15], R. Picha[7], M. Planinic[49], J. Pluta[46], N. Porile[32], J. Porter[45], A.M. Poskanzer[21], M. Potekhin[4], E. Potrebenikova[12], B.V.K.S. Potukuchi[19], D. Prindle[45], C. Pruneau[46], J. Putschke[21], G. Rakness[30],

R. Raniwala[33], S. Raniwala[33], O. Ravel[38], R.L. Ray[40], S.V. Razin[12], D. Reichhold[32], J.G. Reid[45], J. Reinnarth[38], G. Renault[38], F. Retiere[21], A. Ridiger[25], H.G. Ritter[21], J.B. Roberts[34], O.V. Rogachevski[12], J.L. Romero[7], A. Rose[21], C. Roy[38], L. Ruan[36], M.J. Russcher[27], R. Sahoo[15], I. Sakrejda[21], S. Salur[48], J. Sandweiss[48], M. Sarsour[17], I. Savin[13], P.S. Sazhin[12], J. Schambach[40], R.P. Scharenberg[32], N. Schmitz[23], K. Schweda[21], J. Seger[10], P. Seyboth[23], E. Shahaliev[12], M. Shao[36], W. Shao[5], M. Sharma[29], W.Q. Shen[37], K.E. Shestermanov[31], S.S. Shimanskii[12], E Sichtermann[21], F. Simon[23], R.N. Singaraju[43], N. Smirnov[48], R. Snellings[27], G. Sood[42], P. Sorensen[21], J. Sowinski[17], J. Speltz[18], H.M. Spinka[1], B. Srivastava[32], A. Stadnik[12], T.D.S. Stanislaus[42], R. Stock[14], A. Stolpovsky[46], M. Strikhanov[25], B. Stringfellow[32], A.A.P. Suaide[35], E. Sugarbaker[28], C. Suire[4], M. Sumbera[11], B. Surrow[22], M. Swanger[10], T.J.M. Symons[21], A. Szanto de Toledo[35], A. Tai[8], J. Takahashi[35], A.H. Tang[27], T. Tarnowsky[32], D. Thein[8], J.H. Thomas[21], S. Timoshenko[25], M. Tokarev[12], T.A. Trainor[45], S. Trentalange[8], R.E. Tribble[39], O. Tsai[8], J. Ulery[32], T. Ullrich[4], D.G. Underwood[1], G. Van Buren[4], M. van Leeuwen[21], A.M. Vander Molen[24], R. Varma[16], I.M. Vasilevski[13], A.N. Vasiliev[31], R. Vernet[18], S.E. Vigdor[17], Y.P. Viyogi[43], S. Vokal[12], S.A. Voloshin[46], W.T. Waggoner[10], F. Wang[32], G. Wang[20], G. Wang[5], X.L. Wang[36], Y. Wang[41], Z.M. Wang[36], H. Ward[40], J.W. Watson[20], J.C. Webb[17], G.D. Westfall[24], A. Wetzler[21], C. Whitten Jr. [8], H. Wieman[21], S.W. Wissink[17], R. Witt[2], J. Wood[8], J. Wu[36], N. Xu[21], Z. Xu[4], Z.Z. Xu[36], E. Yamamoto[21], P. Yepes[34], V.I. Yurevich[12], I. Zborovský[11], H. Zhang[4], W.M. Zhang[20], Y. Zhang[36], Z.P. Zhang[36], R. Zoulkarneev[13], Y. Zoulkarneeva[13], A.N. Zubarev[12]

(STAR Collaboration)

[1]Argonne National Laboratory, Argonne, Illinois 60439
[2]University of Bern, 3012 Bern, Switzerland
[3]University of Birmingham, Birmingham, United Kingdom

[4]Brookhaven National Laboratory, Upton, New York 11973
[5]California Institute of Technology, Pasadena, California 91125
[6]University of California, Berkeley, California 94720
[7]University of California, Davis, California 95616
[8]University of California, Los Angeles, California 90095
[9]Carnegie Mellon University, Pittsburgh, Pennsylvania 15213
[10]Creighton University, Omaha, Nebraska 68178
[11]Nuclear Physics Institute AS CR, 250 68 Řež/Prague, Czech Republic
[12]Laboratory for High Energy (JINR), Dubna, Russia
[13]Particle Physics Laboratory (JINR), Dubna, Russia
[14]University of Frankfurt, Frankfurt, Germany
[15]Institute of Physics, Bhubaneswar 751005, India
[16]Indian Institute of Technology, Mumbai, India
[17]Indiana University, Bloomington, Indiana 47408
[18]Institut de Recherches Subatomiques, Strasbourg, France
[19]University of Jammu, Jammu 180001, India
[20]Kent State University, Kent, Ohio 44242
[21]Lawrence Berkeley National Laboratory, Berkeley, California 94720
[22]Massachusetts Institute of Technology, Cambridge, MA 02139-4307
[23]Max-Planck-Institut fuer Physik, Munich, Germany
[24]Michigan State University, East Lansing, Michigan 48825
[25]Moscow Engineering Physics Institute, Moscow Russia
[26]City College of New York, New York City, New York 10031
[27]NIKHEF, Amsterdam, The Netherlands
[28]Ohio State University, Columbus, Ohio 43210
[29]Panjab University, Chandigarh 160014, India
[30]Pennsylvania State University, University Park, Pennsylvania 16802
[31]Institute of High Energy Physics, Protvino, Russia

[32]Purdue University, West Lafayette, Indiana 47907
[33]University of Rajasthan, Jaipur 302004, India
[34]Rice University, Houston, Texas 77251
[35]Universidade de Sao Paulo, Sao Paulo, Brazil
[36]University of Science & Technology of China, Anhui 230027, China
[37]Shanghai Institute of Nuclear Research, Shanghai 201800, P.R. China
[38]SUBATECH, Nantes, France
[39]Texas A&M University, College Station, Texas 77843
[40]University of Texas, Austin, Texas 78712
[41]Tsinghua University, Beijing 100084, China
[42]Valparaiso University, Valparaiso, Indiana 46383
[43]Variable Energy Cyclotron Centre, Kolkata 700064, India
[44]Warsaw University of Technology, Warsaw, Poland
[45]University of Washington, Seattle, Washington 98195
[46]Wayne State University, Detroit, Michigan 48201
[47]Institute of Particle Physics, CCNU (HZNU), Wuhan, 430079 China
[48]Yale University, New Haven, Connecticut 06520
[49]University of Zagreb, Zagreb, HR-10002, Croatia

References

[ACD05] Nestor Armesto, Matteo Cacciari, Andrea Dainese, Carlos A. Salgado, and Urs Achim Wiedemann. "How sensitive are high-p(T) electron spectra at RHIC to heavy quark energy loss?" 2005.

[Ack03] K. H. Ackermann et al. "STAR detector overview." *Nucl. Instrum. Meth.*, **A499**:624–632, 2003.

[Ada03a] J. Adams et al. "Production of charged pions and hadrons in Au + Au collisions at s(NN)**(1/2) = 130-GeV." 2003.

[Ada03b] J. Adams et al. "Transverse momentum and collision energy dependence of high p(T) hadron suppression in Au + Au collisions at ultrarelativistic energies." *Phys. Rev. Lett.*, **91**:172302, 2003.

[Ada04a] J. Adams et al. "Azimuthal anisotropy in Au + Au collisions at s(NN)**(1/2) = 200-GeV." 2004.

[Ada04b] J. Adams et al. "Particle dependence of azimuthal anisotropy and nuclear modification of particle production at moderate p(T) in Au + Au collisions at s(NN)**(1/2) = 200-GeV." *Phys. Rev. Lett.*, **92**:052302, 2004.

[Ada05a] J. Adams et al. "Experimental and theoretical challenges in the search for the quark gluon plasma: The STAR collaboration's critical assessment of the evidence from RHIC collisions." *Nucl. Phys.*, **A757**:102–183, 2005.

[Ada05b] J. Adams et al. "Multi-strange baryon elliptic flow in Au + Au collisions at s(NN)**(1/2) = 200-GeV." *Phys. Rev. Lett.*, **95**:122301, 2005.

[Ada05c] J. Adams et al. "Multiplicity and pseudorapidity distributions of photons in Au + Au collisions at s(NN)**(1/2) = 62.4-GeV." *Phys. Rev. Lett.*, **95**:062301, 2005.

[Adl02] C. Adler et al. "Centrality Dependence of High p_T Hadron Suppression in Au + Au Collisions at $\sqrt{s_{NN}} = 130$ GeV." *Phys. Rev. Lett.*, **89**:202301, 2002.

[Adl03] S. S. Adler et al. "Mid-rapidity neutral pion production in proton proton collisions at s**(1/2) = 200-GeV." *Phys. Rev. Lett.*, **91**:241803, 2003.

[Adl05] S. S. Adler et al. "Centrality dependence of direct photon production in s(NN)**(1/2) = 200-GeV Au + Au collisions." *Phys. Rev. Lett.*, **94**:232301, 2005.

[And03] M. Anderson et al. "The STAR time projection chamber: A unique tool for studying high multiplicity events at RHIC." *Nucl. Instrum. Meth.*, **A499**:659–678, 2003.

[Bau75] H. G. Baumgardt et al. "SHOCK WAVES AND MACH CONES IN FAST NUCLEUS-NUCLEUS COLLISIONS." *Z. Phys.*, **A273**:359–371, 1975.

[Bed03] M. Beddo et al. "The STAR barrel electromagnetic calorimeter." *Nucl. Instrum. Meth.*, **A499**:725–739, 2003.

[Che03] Y. Chen. *High Transverse Momentum Charged Hadron Production in Au+Au Collisions at the Relativistic Heavy-Ion Collider.* PhD thesis, University of California–Los Angeles, 2003.

[CNV05] Matteo Cacciari, Paolo Nason, and Ramona Vogt. "QCD predictions for charm and bottom production at RHIC." *Phys. Rev. Lett.*, **95**:122001, 2005.

[DES04] X. Dong, S. Esumi, P. Sorensen, N. Xu, and Z. Xu. "Resonance decay effects on anisotropy parameters." *Phys. Lett.*, **B597**:328–332, 2004.

[DGV06] Magdalena Djordjevic, Miklos Gyulassy, Ramona Vogt, and Simon Wicks. "Influence of bottom quark jet quenching on single electron tomography of Au + Au." *Phys. Lett.*, **B632**:81–86, 2006.

[DK01] Yuri L. Dokshitzer and D. E. Kharzeev. "Heavy quark colorimetry of QCD matter." *Phys. Lett.*, **B519**:199–206, 2001.

[Dun04] J. Dunlop. "http://www.star.bnl.gov/protected/common/common2004/trigger2004/200gev/200gevFaq.html.", 2004.

[Eid04] S. Eidelman et al. "Review of Particle Physics." *Physics Letters B*, **592**:1+, 2004.

[Fer87] T. Ferbel. *Experimental techniques in high-energy nuclear and particle physics.* Addison-Wesley, 1987.

[Giu03] P. Giubellino. "Experiments at the LHC." *Nucl. Phys.*, **A715**:441–450, 2003.

[Gla59] R.J. Glauber. *Lectures in Theoretical Physics*, volume 1. Interscience, New York, 1959.

[Gle01] N. K. Glendenning. "Phase transitions and crystalline structures in neutron star cores." *Phys. Rept.*, **342**:393–447, 2001.

[GW73] D. J. Gross and F. Wilczek. "Ultraviolet Behavior of Non-Abelian Gauge Theories." *Phys. Rev. Lett.*, **30**:1343–1346, 1973.

[GW94] Miklos Gyulassy and Xin-Nian Wang. "HIJING 1.0: A Monte Carlo program for parton and particle production in high-energy hadronic and nuclear collisions." *Comput. Phys. Commun.*, **83**:307, 1994.

[HGR05] Hendrik van Hees, Vincenzo Greco, and Ralf Rapp. "Heavy-quark probes of the quark-gluon plasma at RHIC." 2005.

[HKH01] P. Huovinen, P. F. Kolb, Ulrich W. Heinz, P. V. Ruuskanen, and S. A. Voloshin. "Radial and elliptic flow at RHIC: Further predictions." *Phys. Lett.*, **B503**:58–64, 2001.

[HM96] John W. Harris and Berndt Muller. "The search for the quark-gluon plasma." *Ann. Rev. Nucl. Part. Sci.*, **46**:71–107, 1996.

[Huo05] Pasi Huovinen. "Anisotropy of flow and the order of phase transition in relativistic heavy ion collisions." *Nucl. Phys.*, **A761**:296–312, 2005.

[Joh02] Ian Johnson. *Photon and Neutral Pion Production in Au+Au Collisions at* $\sqrt{s_{NN}} = 130GeV$. PhD thesis, University of California–Davis, 2002.

[JW05] Peter Jacobs and Xin-Nian Wang. "Matter in extremis: Ultrarelativistic nuclear collisions at RHIC." *Prog. Part. Nucl. Phys.*, **54**:443–534, 2005.

[Kar02] F. Karsch. "Lattice Results on QCD Thermodynamics." *Nucl. Phys.*, **A98**:199 – 208, 2002.

[KSH00] P. F. Kolb, J. Sollfrank, and U. W. Heinz. "Anisotropic Transverse Flow and the Quark-Hadron Phase Transition." *Phys. Rev.*, **C62**:054909, 2000.

[Lee75] T. D. Lee. "Abnormal Nuclear States and Vacuum Excitations." *Rev. Mod. Phys.*, **47**:267, 1975.

[Leo87] William R. Leo. *Techniques for Nuclear and Particle Physics Experiments, A How-to Approach.* Springer-Verlag, 1987.

[Mat98] H. Matis et al. "CSN0229A - STAR Geometry." 1998.

[NG84] S. Nagamiya and M. Gyulassy. "HIGH-ENERGY NUCLEAR COLLISIONS." *Adv. Nucl. Phys.*, **13**:201–315, 1984.

[Pol73] H. D. Politzer. "Reliable Perturbative Results for Strong Interactions?" *Phys. Rev. Lett.*, **30**:1346–1349, 1973.

[PV98] A. M. Poskanzer and S. A. Voloshin. "Methods for Analyzing Anisotropic Flow in Relativistic Nuclear Collisions." *Phys. Rev.*, **C58**:1671–1678, 1998.

[Sch04] Kai Schweda. "Highlights from STAR." *J. Phys.*, **G30**:S693–S700, 2004.

[Sch06] G. Schroeder. "http://www.bnl.gov/RHIC/.", 2006.

[SLM03] Torbjorn Sjostrand, Leif Lonnblad, Stephen Mrenna, and Peter Skands. "PYTHIA 6.3: Physics and manual." 2003.

[Sor97] H. Sorge. "Elliptical flow: A signature for early pressure in ultrarelativistic nucleus nucleus collisions." *Phys. Rev. Lett.*, **78**:2309–2312, 1997.

[Sor03] Paul Richard Sorensen. *Kaon and Lambda Production at Intermediate p_T: Insights into the Hadronization of the Bulk Partonic Matter Created in Au+Au Collisions at RHIC.* PhD thesis, University of California, Los Angeles, 2003.

[STA05] STAR. "http://www.star.bnl.gov/STAR/comp/simu/newsite/geometry.html.", 2005.

[TLS01] D. Teaney, J. Lauret, and Edward V. Shuryak. "Flow at the SPS and RHIC as a quark gluon plasma signature." *Phys. Rev. Lett.*, **86**:4783–4786, 2001.

[WHD05] Simon Wicks, William Horowitz, Magdalena Djordjevic, and Miklos Gyulassy. "Heavy quark tomography of A + A including elastic and inelastic energy loss." 2005.

[Wil74] K. G. Wilson. *Phys. Rev.*, **D10**:2445, 1974.

[Won94] C. Wong. *Introduction to High-Energy Heavy-Ion Collisions.* World Scientific, Singapore, first edition, 1994.